ABSTRACT

Title of Document: MECHANICS OF NON PLANAR INTERFACES IN FLIP-CHIP INTERCONNECTS

Koustav Sinha, Doctor of Philosophy, 2012

Directed By: Professor Abhijit Dasgupta, Department of Mechanical Engineering

With the continued proliferation of low cost, portable consumer electronic products with greater functionality, there is increasing demand for electronic packaging that is smaller, lighter and less expensive. Flip chip is an essential enabling technology for these products. The electrical connection between the chip I/O and substrate is achieved using conductive materials, such as solder, conductive epoxy, metallurgy bump (e.g., gold) and anisotropic conductive adhesives. The interconnect regions of flip-chip packages consists of highly dissimilar materials to meet their functional requirements. The mismatches in properties, contact morphology and crystal orientation at those material interfaces make them vulnerable to failure through delamination and crack growth under various loading patterns. This study encompasses contact between deformable bodies, bonding at the asperities and fracture properties at interfaces formed by the interconnects of flip-chip packages. This is achieved through experimentation and modeling at different length scales, to be able to capture the detailed microstructural features and contact mechanics at interfaces typically found in electronic systems.

Two different forms of interconnects in flip-chip packages have been studied here; the first of them is the gold-gold interface in adhesively bonded flip-chip-on-flex packages that are based on a Non Conductive Adhesive (NCA) bonding process. The process is a form of adhesive joining and requires the simultaneous application of adhesive, pressure, temperature, and time to bring a flip chip into contact to a board or flex foil. Experimental investigations performed in [4] [84] show evidence of metallurgical bonding between mating gold bumps on silicon dies. In this study, further pull test experiments are performed to detect the effect of bonding force and bonding time on the strength of the interface. Also, the roughness features evolve during the bonding process at the interface. The surface roughness of unmated and mated Au bumps is characterized on flip-chip dies, since the amount of surface flattening provides insights into both mechanical interlocking as well as propensity for cold-welding. A diffusion creep model fits well to the experimental results which can be used as a prediction tool for such bonding process. Further, using techniques developed in related studies [3] [85], elastic-plastic, large-deformation finite element modeling with nonlinear contact surfaces is used to further understand and quantify this time-dependent surface-flattening phenomenon. The consequences that these bonding mechanisms have on the robustness of the adhesive interconnect are being investigated.

The second study is on Solder-IMC interface which is prevalent in almost any electronic package. For example, shock and drop loading can cause interfacial fractures between layers of dissimilar intermetallic compounds (IMCs) in solder joints that connect components to printed wiring assemblies (PWAs) in electronic

systems. Studies have revealed that these interfaces are usually wavy and non-planar and that the waviness decreases with continued thermal aging, accompanied by a reduction of the apparent fracture resistance of the interface [65]. This loss of fracture resistance can be a result of changes in the stress-strength interference due to: (i) increase in the stress intensity factor because of decrease in the waviness; and (ii) intrinsic changes in the interfacial fracture energy caused by aging-induced chemical changes. The focus of this study is to explore the first of the two factors listed above by constructing detailed finite element fracture models and comparing the predictions with the test data published in the literature [6]. Global-local, elastic-plastic-creep finite element analysis is conducted to assess the changes in fracture energy release rates brought about by the changing roughness profiles and comparing them with test data. The global model analyses the average stresses in Yao's solder cantilever specimen [65] and the local finite element model extracts the energy release rate around interfacial crack-tips. The energy release rates are averaged over a periodic length of the wavy interface to obtain effective average values over the range of phase angles, so that the results can be compared with test results reported by Yao & Shang [65]. Parametric studies are conducted for the effect of crack length and load rate on the relative changes of strain energy release rate for different degrees of nonplanarity. This is a fundamental study to understand the influence of loss of IMC interfacial waviness on the loss of apparent fracture resistance.

These studies provide deeper understanding of the basic physical phenomena that are responsible for interfacial bonding and failures at nonplanar interfaces.

MECHANICS OF NON PLANAR INTERFACES IN FLIP-CHIP INTERCONNECTS

By

Koustav Sinha

Dissertation submitted to the Faculty of the Graduate School of the University of Maryland, College Park, in partial fulfillment of the requirements for the degree of Doctor of Philosophy
2012

Advisory Committee:
Professor Abhijit Dasgupta, Chair and Advisor
Assistant Professor Santiago Solares
Professor Sung Lee
Professor Aris Christou
Associate Professor Patrick McCluskey

© Copyright by
Koustav Sinha
2012

Dedication

To my parents for showing me how to dream and then heartily supporting those dreams…

also to the love of my life for being my strength & motivation.….☺

Acknowledgements

My first few days in College Park were like entering a completely new planet. The very first meeting I had with Prof. Dasgupta lasted for just 10 mins and it was one of the most memorable ones of all. He immediately welcomed me to the group, took a scrap paper and made some flow-charts which apparently contained the blue-print of my next 5 years. That scrap paper acted as a guiding light in the up and down journey of my graduate life. The immense contribution he had to my growth as a researcher and person can't be acknowledged enough in this small space. He playing the role of a perfect mentor and being like a mirror to my every mistake helped me shape to a better professional to say the least.

Grad school can never be complete without labmates. I was most fortunate to have some tremendous seniors who voluntarily helped me out in small things that you have no idea about when you land in unfamiliar settings. When the burden of research weighed heavy on the shoulders, there was always a few in the lab I could hang out with. Even staying up whole night to finish project reports didn't feel too hard thanks to their presence. Some of them ended up being very good friends that will stay for the rest of my life. Many thanks to Lynn, Yasir, Gayatri, Yuxun, Joe, Dan, Shaughn, Leila, Cholmin, Stuart, Subhasis, both the Ehsans, Josh, Jingshi, David, Jaemi, Matt, Stephane and all the German and French folks. You guys made it worth coming here.

Special thanks also goes to Dr. Das, Rama Boudi, and Jahnavi, who always made me feel at home here in Maryland.

While the thesis would have been incomplete without the people mentioned above, the inspiration behind me pursuing higher studies was my family. Their unconditional love and unwavering support made all these possible and I owe everything to them. Not to forget the innumerable other people who have been part of my life in numerous ways and helped me shape as a person.

Table of Contents

Dedication....ii
Acknowledgements....iii
Table of Contents....v
List of Tables....vii
List of Figures....ix
Chapter 1: Introduction to the Thesis....1
Chapter 2: Gold Bump Interconnects in Adhesively Bonded Flip-Chip Joints: Background Study....2
2.1 Problem Statement....2
2.2 Background and Motivation....3
2.3 Literature Review....6
2.3.1 Adhesively Bonded Interconnects in FCOF....6
2.3.2 Cold Welding....7
2.3.3 Contact Area or "a-spot"....11
2.3.4 Contact Area vs Bond Strength....12
2.3.5 Gold Surface Contaminants....13
2.4 Approach....14
Chapter 3: Gold Bond Strength in Adhesively Bonded Flip-Chip Joints: Experimental Results and Empirical Model....28
3.1 Abstract....19
3.2 Introduction and Problem Statement....30
3.3 Literature Review....33
3.4 Overall Approach....36
3.5 Test Specimens....38
3.6 Bond Process Matrix....41
3.7 Characterization of Gold Bump Surface Topology....42
3.8 Pull Test Setup and Procedure....45
3.9 Specimen Adaptor....46
3.10 Pull Strength Results....47
3.11 Empirical Bonding Model....49
3.11.1 Theoretical Basis for Bonding Model....42
3.11.2 Empirical Determination of Model Constants....53
3.12 Summary and Conclusions....56
Appendix 1....64

Chapter 4: Gold Bond Strength in Adhesively Bonded Flip-Chip Joints: Modeling and Simulation....69
4.1 Abstract....69
4.2 Introduction and Problem Statement....70
4.3 Literature Review....72
4.4 Approach....76

4.5 Experimental Characterization of Gold Properties…..77
4.6 Time-Independent Finite Element Model of Au-Au Bonding............................81
4.7 Time-Dependent Finite Element Model of Au-Au Bonding...........................…85
4.8 Response Surface Model………………………………………………...............88
4.9 Summary and Conclusion...…...........93
Chapter 5: Solder Interconnects in Adhesively Bonded Flip-Chip Joints: Crack Behavior at the Non-Planar Interfaces..101
5.1 Abstract...102
5.2 Introduction..…104
5.3 Literature Review..104
5.3.1 Nonplanar Interfacial Mechanics...104
5.3.2 Elastic-Plastic Interfaces………………………….................................106
5.3.3 Effect of Aging on Roughness……………………...............................106
5.3.4 Changes in Stress Intensity Factor due to Crack Shielding Mechanism.....107
5.3.5 Fracture Toughness Experiment for Wavy Solder Interface......................108
5.4 Approach...112
5.5 Finite Element Analysis……………………………………………….............113
5.5.1 Macroscale Model…………………………...113
5.5.2 Microscale Model……………………………......................................115
5.5.3 Calculation of Strain Energy Release Rate………...................................117
5.5.4 Combined Effect of Crack Length and Roughness…...............................118
5.5.5 Combined Effect of Loading Rate and Roughness….................................120
5.6 Summary and Conclusion...….........121
Chapter 6: Dissertation Contributions………………………..................................126
6.1 Gold Bumps in Flip-Chip Interconnects...126
6.2 Solder Bumps in Flip-Chip Interconnects………...126
Chapter 7: Limitations and Future Work...128
7.1 Gold Bumps in Flip-Chip Interconnects..…..128
7.2 Solder Bumps in Flip-Chip Interconnects...129
Appendix 1: Characteristics of the Pull Test Specimen (Chapter 3)..............….......…100
Appendix 2: Specifications of Pull Tester (Chapter 3)...131
Appendix 3: Aluminum Pull Test Fixture Design (Chapter 3)........................….......132
Appendix 4: Surface Characterization Plots (Chapter 3)..134
Appendix 5: Derivation of Rate of Change of Contact Area for Different Diffusion Models (Chapter 3)...138
Appendix 6: FEA Schematic (Chapter 4)...143
Appendix 7: Multi-Asperity 2D Model Details (Chapter 4)..147
Bibliography...154

List of Tables

Table 3-1: Specimen matrix..42

Table 3-2: Final statistics of the Surface Topology from AFM measurements.............45

Table 3-3: Emperical Model Constants..55

Table A1-1: Gold Property Constants..65

Table 4-1: Power-law Creep Constants for Gold...80

Table 4-2: Comparison of Plastic Deformation (Empirical vs FEA).............................84

Table 4-3: Parameter Levels..89

Table 4-4: Design of Experiment...90

Table 4-5: Response Surface Model Coefficient Values...91

Table 4-6: Ranking of the Variables and Interaction Terms..92

Table 5-1: IMC morphology dimensions...116

Table A1-1: Linear Properties for Solder-IMC Model...124

Table A5-1: Gold Property Constants...139

Table A5-2: Other Parameters...140

List of Figures

Figure 2-1: Adhesively Bonded Au-bumped Flip-chip on Flex (FCOF)…………........….4

Figure 2-2: NCA-Bonded FCOF Interconnect between an Au bump on a Silicon Chip and the Matching Au-plated Copper Pad on the Substrate......................................4

Figure 2-3: Decrease of Compressive Force due to Thermal Cycling as a Function of Time...5

Figure 2-4: Schematic of the Adhesive Avalanche Phenomenon.........................…..........9

Figure 2-5: Normalized Pull Test Results...10

Figure 2-6: Apparent Contact Surface and Atomistically-flat Load- bearing Areas..........12

Figure 2-7: Investigation Flowchart...15

Figure 3-1: Conductive Adhesive FCOF Interconnect with Conductive Particles Completing the Circuit...…..........................31

Figure 3-2: Non-conductive FCOF Interconnect...32

Figure 3-3: Schematic View of Growing Bond Showing Routes of Three Mechanisms of Mass Transfer...36

Figure 3-4: Investigation Flowchart...38

Figure 3-5: Test specimens Preparation..…........39

Figure 3-6: Test specimens with Dimensions and Bump Alignment Scheme...................39

Figure 3-7: Die Penetrant Test...…........40

Figure 3-8: AFM Side-View Image of a Gold Bump...43

Figure 3-9: AFM images of (A) an Unmated Surface and (B) a Mated Surface…............44

Figure 3-10: Experimental Setup...….............46

Figure 3-11: Normalized Pull Test Results...…............48

Figure 3-12: Normalized Pull Test Results (Effect of Temperature)................…............49

Figure 3-13: Contact Area Fraction vs Bonding Time trends for Different Mechanism....52

Figure 3-14: Model Fitted with the Experimental Data at Various Bonding Forces….......54

Figure 3-15: Model Fitted with the Experimental Data at Various Bonding Temperatures...55
Figure A1-1: Contacting Surfaces Modeled as Small Cells due to Assumed Symmetry...64
Figure 4-1: Investigation Flowchart..…....77
Figure 4-2: Cross-Sectioned Au Bumps (A) Topography, (B) Derivative of Topography...…........78
Figure 4-3: Roughness along x-x' Cross-Section..….......78
Figure 4-3: (a) Load vs time (b) Load vs indentation depth (c) Variation of elastic modulus & hardness on indentation depths…………………………….......................79
Figure 4-4: Stress-Strain Behavior of Gold………………………………………….........80
Figure 4-5: Multi-Asperity Model (a) Geometry (b)..82
Figure 4-6: Displacement contour plot at a selected offset configuration.........................82
.
Figure 4-7: Offset Modeling Results: (a) Percentage Contact Length vs Overlap Length (b) Force vs Displacement…………………………………….....................83
Figure 4-8: Force vs Contact Length for different configurations....................................84
Figure 4-9: Material Property Sensitivity Plots..85
Figure 4-10: Representative "a-spot" Finite Element Model.................................…......86
Figure 4-11: Schematic of FEA Approach...….........87
Figure 4-12: Comparison of Results: FEA vs Experiment.................................….........88
Figure 4-13: FEA result in DOE..…......90
Figure 4-13: Contour Plot of Bond Strength from Response Surface Model Predictions...…...93
Figure 5-1: Example of Scalloped IMC Layer in a Solder Joint...............................…......103
Figure 5-2: Graphical Representation of Eqn. (5-1)..…......105
Figure 5-3: Changes in interface morphology due to aging...107
Figure 5-4: Interface Microstructures in Eutectic Sn-Pb/Cu Solder Joints: (a) Water Quenching, (b) Air Cooling, and (c) Furnace Cooling………........……......109

Figure 5-5: Threshold Strain Energy Release Rate vs Cooling Rate…………….............111

Figure 5-6: Investigation Flowchart...112

Figure 5-7: Global Model Geometry..….......113

Figure 5-8: Global Model Displacement Plot..….....114

Figure 5-9: Global and Local Model..….......115

Figure 5-10: IMC Layer Morphology Details for 3 Cooling Rates.........................…......116

Figure 5-11: Geometric Comparison of the IMC layers in Shang's experiment and FEA...…...........117

Figure 5-12: Nodal Von-Mises StrainPlot at the Crack Tip...118

Figure 5-13: (a) J-Integral Contours around the Crack Tip (b) Convergence of the J-Integral Value..…..................118

Figure 5-14: Crack Length Effect on Strain Energy Release Rate...............................…..119

Figure 5-15: Comparisons of Results from Shang's experiment and FEA (I).................119

Figure 5-16: Comparisons of Results from Shang's experiment and FEA (without strain rate effect)…………..120

Figure 5-18: Comparisons of Results from Shang's experiment and FEA (with strain rate effect).............…...121

Figure A1-1: Stress-Strain Curves for 95Pb5Sn (Darveaux & Banerji) at Various Temperatures..…...124

Figure A1-2: Von Mises Stress vs Von Mises Strain Curves for SnPb (Qian) at Various Temperatures...….......125

Figure A1-1: Pull Test Specimen Schematic..131

Figure A2-1: Pull Tester..132

Figure A3-1: Pull Test Fixture Design...133

Figure A4-1 to 3: 3D Surface Profiles...134

Figure A4-4: Measured Cross-Sections..137

Figure A5-1: Contacting Surfaces Modeled as Small Cells Due to Assumed Symmetry..138

Figure A6-1: Schematic of FEA Approach..143

Figure A6-2: Representative "a-spot" Finite Element Model.................................143

Figure A6-3 to 7: Roughness Profiles..144

Figure A7-1: Multi-Asperity Model...147

Figure A7-2 to 12: Offset Models...148

Chapter 1: Introduction to the Thesis

From a structural perspective, electronic devices are a conglomeration of composite structures fabricated from highly dissimilar materials. Often, the interfaces between these materials are where failure is most likely to occur when the device is subjected to thermomechanical loading. Thus, understanding and being able to predict the behavior of critical interfaces in a device is directly related to the reliability of the system. For Flip-Chip interconnects two major durability issue lies at its bump interfaces that are susceptible to cracking under cyclic and other harsh environmental loading conditions. To mitigate this it's important to make the interfacial bonding robust by optimizing the bond formation process parameters. This study is on two different interconnect types - the first one involves gold-gold interconnect strength for flip-chips and the second problem is on the fracture behavior of the interface of solder joints in flip chip joints as well. The effect of various bonding, geometric parameters and constitutive properties on the strength behavior of these joints is quantified. This helps optimize the process variables to get the desired strength at these critical interfaces and therefore result in a reliable product. Chapters 2, 3 & 4 provide the background, approach and the work done in this study for the gold bump interface problem. Chapter 5 then provides the literature review and the work done on the solder bump interface problem. Finally the contributions, limitations and proposed future work have been sketched out in the final two chapters.

Chapter 2: Gold Bump Interconnects in Adhesively Bonded Flip-Chip Joints: Background Study

2.1 Problem Statement

In adhesively bonded FCOF (Flip-Chip On Flex) packages (Figure 2-1), thermal expansion and viscoplastic stress relaxation of the epoxy during temperature excursions due to power cycling or temperature cycling [84] can decrease the contact forces at the interface between the gold bump (contact structure) on the Flip-chip (FC) die and the gold-plated copper pad on the flex circuit. The decrease of contact force, in turn, can result in an increase of the electrical contact resistance and threaten interconnect reliability. Earlier studies [6, 86] proposed that the interconnection bonding may be due to combination of two mechanisms caused by compressive forces at the contact interface caused by curing-induced shrinkage of the adhesive: (a) mechanical interlocking between asperities on the mating Au surfaces due to compressive deformations, and (b) metallurgical joining due to solid state diffusion bonding between the Au-surfaces. Based on their empirical findings, these studies [6, 86] eliminated the possibility of mechanical interlocking and suggested that metallurgical bonding is the most likely mechanism.

In this study, we intend to explore in more detail, the possibility of metallurgical mechanisms at the Au-Au interface. Literatures [80, 81] suggest that the bond strength is related to the contact area and that the process of metallurgical bonding can be almost instantaneous if the contact surfaces are atomistically flat. We therefore assume in this study that the rate governing mechanism for interface bonding is the rate of growth of the contact area. Contact area is defined here as the area over which the interfaces come into intimate, atomistically flat

contact. An additional possible rate governing mechanism could be the time required for chemical reduction of gold oxides at the interface. In this study we assume the gold content is negligibly small at the temperature of interest, based on the literatures [82, 83]. Thus the only remaining mechanism to be examined here is the flattening rate of the contact interface.

In particular, the focus of this study is limited to the contribution of Coble creep deformation at the Au-Au interface asperities, on the growth rate of the contact area. Other diffusion mechanisms, such as Nabarrro-Herring creep and surface diffusion are ignored, based on preliminary estimates for gold, at the temperature and stress levels expected during the bonding process.

2.2 Background and Motivation

Flip-chip bonding has existed for more than 30 years and is known for its advantages in miniaturization, high interconnect density, and improved electrical performance because of minimal lead length [5]. As shown in Figure 2-1, flip-chip electronic assembly is the direct electrical connection of face-down ("flipped") electronic dies onto a substrate. The interconnection method used in this study is based on adhesively bonding flat gold bumps on the IC to matching Au-plated copper pads on flexible or rigid substrates, rather than soldered connections [6], because of the low cost and low process temperatures required (curing temperatures for the adhesive are usually approximately 200°-250°C). Non-conductive adhesives (NCAs) are increasingly replacing conductive adhesives as an important bonding method, to prevent lateral shorts in ultra high-pitch, high-density I/Os.

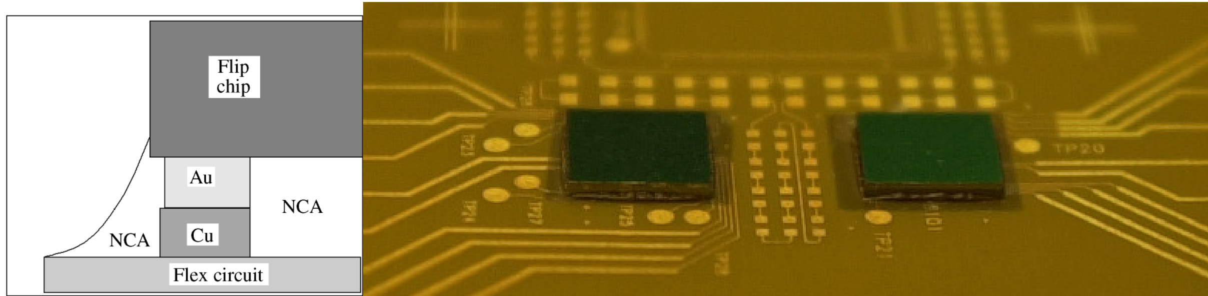

Figure 2-1: Adhesively Bonded Au-Bumped Flip-Chip on Flex (FCOF)

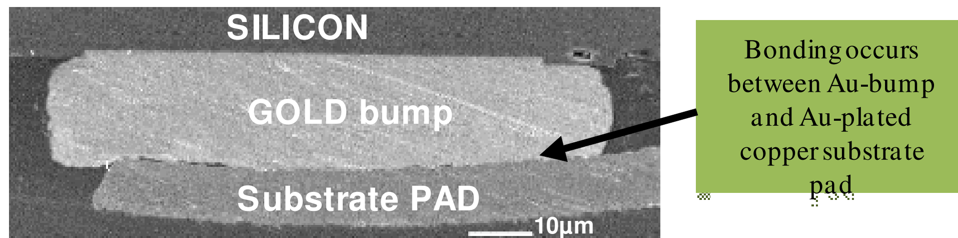

Figure 2-2: NCA-Bonded FCOF Interconnect between a Au Bump on a Silicon Chip and the Matching Au-Plated Copper Pad on the Substrate

There are few possible competing bonding mechanisms in this interconnect architecture at the Au-Au interface. They can be mechanical interlocking of mating asperities due to local compressive plastic deformations, or metallurgical bonding at the bump to pad interface. Although the bonding temperature for adhesive curing is too low for metallurgical bonding of rough Au-Au interfaces, preliminary experimental results [3, 84] do suggest the presence of metallurgical bonding in FCOF. The underlying phenomena are not fully understood.

In fact, solid-state bonding has also been suggested in Anisotropic Conductive Adhesives (ACA). Haase [3, 86] thermally cycled a FCOF package bonded with ACAs and reported no change in the mean contact resistance throughout the temperature cycle for 1000 cycles. The only change was cyclic due to temperature-induced changes in the bulk-resistivity of the gold

and copper in the interconnects. This suggests that interface contact is not just by compressive surface forces but by either mechanical interlocking between asperities due to local plastic deformations, or metallurgical bonding by solid-state diffusion [84]. The aim of this study is to provide insights into the fundamental nature of this interfacial contact.

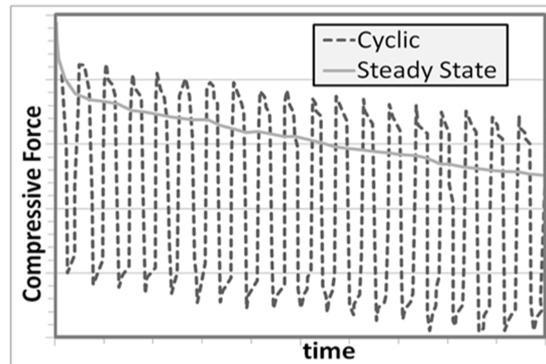

Figure 2-3: Decrease of compressive force due to thermal cycling as a function of time (ref. [8])

Here the focus is on Au bumps bonded with NCAs. Figure 2-2 shows a NCA interconnection between a gold bump on the silicon die and an Au-plated copper pad on the substrate. In order to achieve reasonable durability of NCA bonded FCOF joints, a high compression force is used during bonding, which results in plastic flattening of asperities at the interface of the mating Au bumps. Since each die has many bumps with coplanarity tolerances, extensive work has been done before on determining the requisite bonding force needed to bring all interconnect pairs into contact [3, 4 and 85]. Some researchers have postulated that the two mating surfaces are merely in physical contact without any metallurgical bonding or plastic interlocking, and that the interconnect will therefore lose mechanical integrity with temperature cycling because of cyclic loss of compressive interfacial stress due to viscoplastic relaxation of the epoxy, shown schematically in Figure 2-3. However, as discussed above, thermal cycling

tests conducted in [3, 86] do not show such cyclic degradation, thus suggesting a positive bond-strength that forms at the interface, perhaps by 'cold-welding' or by plastic interlocking, at the deforming asperities. Investigations by Farley, et al. [4] suggest that the bonding process is indeed metallurgical bonding rather than plastic interlocking. The reason is for plastic interlocking we would expect an instantaneous rise in bond strength but experimental findings show a delay in the development of any considerable bond strength. The purpose of the proposed study is to provide insights into the fundamental nature of this metallurgical bonding process so that the interfacial strength at this interface can be quantified and optimized, as a function of the bonding pressure, temperature and time. Clearly, the implications are enormous to the microelectronics industry, because of the potential for a very robust and durable, low-cost, low-temperature, Pb-free, 'green' interconnection method for ultra-fine-pitch ICs.

2.3 Literature Review

An extensive literature search has been conducted to understand the nature and history of the study of adhesively bonded interconnect failure mechanisms.

2.3.1 Adhesively Bonded Interconnects in FCOF

Flip chips started to see extensive use around 1999 [5]. Much work has been done since then to quantify the reliability and durability for specific packages mostly focused on cycles to failure, contact resistance, and effects of different bonding forces and bonding temperatures. Currently, the majority of papers on adhesively bonded flip chips center around a "top-down" approach. That is, the studies test specific package geometry and report package-specific reliability data, or that their package simply passed a certain number of temperature cycles without going into further details [30-39]. Simulation techniques have been used in conjunction with experimental

results in an attempt to fully characterize adhesively bonded flip-chips [36][41]. Mercado, et al. studied the failure mechanisms of ACF bonded packages, but concluded that the reliability was strongly dependent on moisture, and therefore ignored temperature cycling [40]. It has been observed that there is a relationship between interconnect resistance and compressive force [32][43][36][42]. Chan, et al. [35] and Li [37] worked on relating bonding pressure and bonding temperature to more reliable adhesively bonded flip chips. Chan, et al. based their conclusions of proper bonding pressure on proper ACA particle deformation. Fu, et al. agreed with Chan's work stating particle deformation as an important factor, and added that particle location in the interface is also important [45]. The further the particles are located from the center, the resistance of an interconnect increases.

Haase [86] found that the contact resistance in his Au-Au interconnect did not degrade through 1000 cycles, but Li, et al.'s Au-Ni system [37] did. Wu, et al. looked into the impact of bump height on interconnect reliability, concluding that higher bumps resulted in higher ACF stress [47]. Simon, et al. developed an analytical model to describe the development of mechanical properties during epoxy cure, using a combination of time temperature superposition, time-crosslink density superposition, and elasticity of the polymer network [24].

2.3.2 Solid-State Bonding

The effects of solid-state bonding have been noted since the 1940s. Holm's Electric Contacts Handbook [7] tells us that two clean metallic surfaces pressed together can have free electrons move across the interface and form metallic bonds. These bonds formed due to solid state bonding have strength along the same order of magnitude as that of the metallic crystal, and will increase in strength with time. Soft metals such as copper or gold owe their coherence largely to metallic bonds. They are able to transfer material from one surface to another if separated. In

1971, Johnson, Kendall, and Roberts reported what became known as the JKR equation for determining the surface energy of materials in contact [8]. Johnson et al. reported that, although surface roughness masks the deformation produced by attractive forces in normal metals, for soft metals that difficulty does not manifest. Cuthrell [9] tested the bonding strength of an aluminum alloy and investigated the mechanics of the a-spot formation. He pressed two annealed aluminum hemispheres under high vacuum and room temperature together and observed that existing cold welds under a load at room temperature can grow, resulting in an increased contact area, decreased contact resistance, and increased tensile strength [9].

Smith [1989] proposed "adhesive avalanche". Adhesive avalanche is where atomic layers fall together when they approach a certain separation distance. A new wear mechanism that involves avalanching is proposed in [87]. Ferguson, et al. [1991] observed "unexpected" cold welding under ambient and "dirty" conditions with experiments of ~20nm thick Au films on a poly(dimethylsiloxane) (PDS) support film [28]. Under low loads (up to 0.2 g/cm^2), ambient temperatures/pressures, and with weakly adsorbed surface impurities, substantial cold welding occurred. They hypothesized that the weld tangentially displaces loosely adhered contaminants, and forms cold welded islands. They also measured the electrical resistance, and found it to be less than 0.4 ohm-cm^2. Taylor [1991] observed the adhesive avalanche phenomenon, investigating atomically flat surfaces in close proximity. He found that adhesive avalanche occurs when surface layers approach the bulk value of atomic separation. Simulating adhesion between atomically flat surfaces, the study showed that avalanche and the resulting stress waves make determination of energetic data from experiment difficult [25]. Recently, Alcantar, et al. [2003] experimented on gold coated surfaces. Spontaneous "jump in" (adhesive avalanche) distances remained the same across all specimens, with different forces and approach rates.

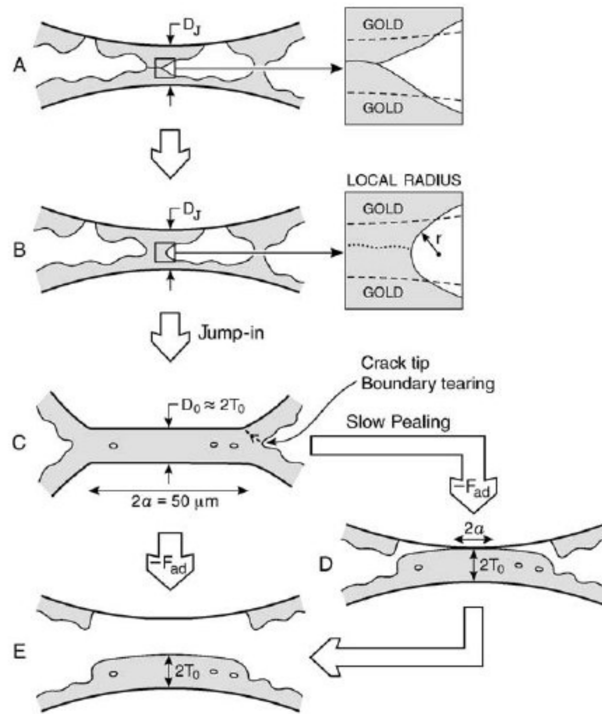

Figure 2-4: Schematic of the Adhesive Avalanche Phenomenon, Alcantar, et al. [33]

They showed high local pressure in contacting junctions result in flattening, followed by cold welding. On further compression, the diameter of welded zone increases and then slowly creeps more under constant force. Upon separation, some material would transfer to the other, mated surface (material added, material removed, shown schematically in Figure 2-4). Atomic force microscopy (AFM) was used to image the sites [88]. However, the hypothesis of adhesive avalanche doesn't hold in this case as there is a finite time delay in the build up to the bond strength.

Farley, et al. [4], conducted pull-test experiments on joined Au-Au interface specimens fabricated by bonding two Au-bumped Silicon flip-chips together face-to-face. The bonding parameters were parametrically varied, looking for evidence of metallurgical bonding and its

effect on interfacial strength. The specimen fabrication matrix included three parameters: (a) bonding force (F_b) (b) bonding temperature (T_b) and (c) Bonding time (t_b). The ranges of the above parameters used in the preliminary experiments were 230 MPa for nominal bonding stress, 200-250°C for bonding temperature and 5-120 seconds for bonding time. The interfacial pull force F_p was then evaluated through pull tests, which gave an indication of the interfacial bonding strength under tensile load. The dependence of this bond strength on bonding time (at two different bonding temperatures) provided important evidence of the possible presence of diffusion-assisted metallurgical bonding between the two gold bumps.

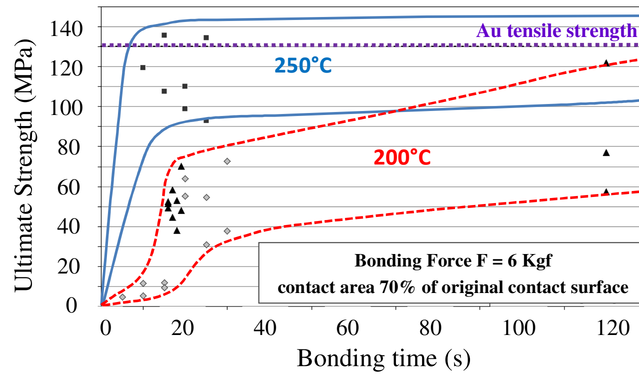

Figure 2-5: Normalized Pull Test Results [4]

The results, shown in Figure 2-5, describe how the interfacial bonding strength depends on bonding-temperature and bonding-time. There is a clear sigmoid trend with a sharp upward transition in bonding strength after a certain threshold time. Specimens bonded at 200°C, showed a strength transition at $t_b \approx 15$ seconds. After 20 seconds, the bond force asymptotically approached a maximum value that was close to the strength of bulk Au. There appeared to be significant scatter in the data caused by misalignment of the test force during the pull test (this is difficult to avoid due to the manufacturing tolerances of the specimen adapter and misalignment of the test vehicle on the testing machine) and variation in the contact area due to chip

misalignment during bonding. The fracture strength of the specimen with the elevated bonding temperature of 250°C (Figure 2-5) confirmed that the higher temperature enabled higher diffusion rates, such that the threshold time for strength transition reduced to about 10 seconds. Also, the elevated temperature could have enhanced plastic flattening of the asperities on the surface and thereby led to a larger contact area. The load bearing area was about 70% of the original bump surface area, which led to higher interfacial bond strength than it would have been had there been full contact between the mating bumps. Once again, the normalized values showed that the contact strength asymptotically approached the tensile strength of bulk soft Au, as the bonding time increased. The important insight that was gained from these experiments into the nature of the joint strength was that a metallurgical bond is likely to be forming at the interface due to stress-assisted solid-state diffusion.

2.3.3 Contact Area or "a-spot"

The conductive connection emerges through "full" contact between the two surfaces, which is facilitated by plastic deformation of asperities on one or both Au surfaces during the bonding process. The contact area clearly has an influence on the apparent bonding strength and is a function of the surface roughness and bonding force. If two contact members are pressed together by a load the initial contact points, induced by the surfaces roughness, becomes enlarged from small contact areas since the materials (gold) are deformable. Simultaneously, new contact points emerge by deforming the voids elastically and/or plastically that lowers the voids coming into contact (Fig. 2-6). These areas are called a-spots and its sum is called load-bearing area [24]. The interfaces between these contact areas are almost atomistically flat and are called "a-spots." The flatness over the "a-spot" is important since it governs the probability of cold-welding at these regions [25]. The sum of these "a-spots" is the actual load-bearing area [50] A_b, while the

entire interface is the apparent contact area A_a.

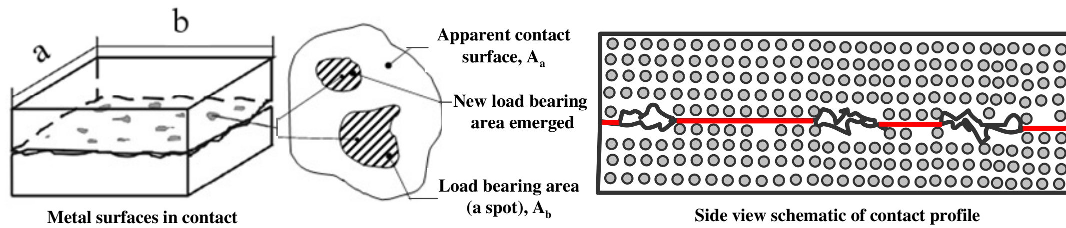

Figure 2-6: Apparent contact surface and Atomistically-flat Load- bearing Areas ('a-spots') [84]

The nature of the interfacial bonding at these 'a-spots' is of great interest in this case, and will be examined in this study through a combined experimental-theoretical, multi-scale approach. The Au surface undergoes some degree of oxidation. Although the oxide layer is partially disrupted by the contact forces at the 'a-spots', there are still oxide molecules and other chemical contaminant molecules (from process chemicals like the adhesive) present at the interface and the bonding mechanism therefore also involves some amount of chemical reduction. Models of this bonding process must therefore address the relevant chemical reactions in addition to the mechanical deformations and diffusion processes. Some of the reactions are exothermic and will change the interface temperature, thus further affecting the bonding kinetics.

2.3.4 Contact Area vs Bond Strength

One of the assumptions made in this study is that the numerically computed contact area at any given bonding time can be directly correlated to the bond strength. While the nature of bonding at the atomistic scale may not be so perfect, previous studies do indicate a good correlation between the two. [80] took into account that real joining is only located in some parts of the whole nominal contact area because all surfaces are rough with a random asperity distribution.

When the bond surfaces are pressed together, real contacts only exist in the high spots. So the actual bond strength should be calculated by introducing the contact ratio γ, as follows:

$$\gamma = S_r / S_{nom} \qquad (2\text{-}1)$$

$$\sigma_r = \sigma_{nom} * \gamma \qquad (2\text{-}2)$$

where S_r is the real contact area, S_{nom} the nominal contact area and σ_r the real bond shear strength.

The numerically estimated bond strength for thermosonic bonding from this assumption had a good match with the experimental values. Another study by Fu et al. [81] probed the interfacial structure between steel and concrete by measuring the contact electrical resistivity. Any fractional change in the measured contact resistivity indicated the fractional change in the true contact area. The bond strength was then measured for every interface sample for which the interfacial structure was analyzed. The bond strength vs contact resistivity plot showed a fairly linear pattern which indicated that the average bond strength in a macroscale can be traced back to its real contact area at the interface.

However for a more accurate correlation, the atomistic scale bonding patterns has to be taken into account to predict the real bond strength. This is beyond the scope of this study but must be taken into consideration while inferring from the results.

2.3.5 Gold Surface Contaminants

Gold is often viewed as inert metal because of the resistance it offers for chemisorptions or for dissociation of many gas phase molecules on its surface. Although gold is difficult to oxidize in air, different species of chemical contaminants and oxide layers on the surface can be expected from some of the recent works. Bazhutin et al. [82] found that at elevated temperatures (T >

900K), molecular oxygen adsorbs on gold surfaces forming a surface gold oxide. However, at lower temperatures like T=300 K atomic oxygen adsorbs and completely desorbs from the surface at T=500–600 K without transforming to surface oxide oxygen. It's not like the amount of surface oxide in that temperature range is absolutely zero but it's a very low percentage and doesn't change much. Oxygen chemisorbed on the surface is the primary species at low coverages or low surface temperatures. [83] also showed that at lower temperatures, surface oxides are very low percentage and stays consistent upto very high temperature.

Farley, et al. [4] conducted experiments that showed considerable increase in bond strength when the ambient temperature changed from 473K to 523K at lower bonding time region. This maybe because chemisorbed oxygen atoms got completely removed as it fell in that 500-600 K range and clean gold atoms could easily come into contact and form bonds more easily.

This study focuses on the diffusion phenomenon and it's interaction with bonding parameters, roughness features and constitutive properties. The contaminant factor on the gold surface might play a role too and needs a separate study to look into that. Most of the insight so far has been the change in cohesive strength due to presence of oxides but the effect of chemisorbed oxygen atoms on bond strength has hardly been looked into and would provide better explanation to the temperature effect.

2.4 Approach

The flowchart in Figure 2-7 illustrates the overall approach to the problem. Au-Au bonded flip-chip specimens are fabricated at various bonding conditions, based on a carefully designed process matrix intended to highlight the parametric influence of process parameters on the bond strength. Pull tests are then being conducted on these specimens to establish the time-dependent

trend of interfacial bond strength at different bonding force and bonding time conditions. Following that some of the separated Au surfaces are being carefully characterized. This surface topology (roughness) information is subsequently used to model the asperity flattening process during bonding due to localized plasticity at nano-to-micron length scales and creep deformation. A creep model is successfully fitted to the experimental results which show insights on the possible dominating bonding mechanisms. In parallel an elastic-plastic-creep FEA of a single-asperity model is developed. The constitutive properties for gold partly come from nanoindentation tests being conducted and partly from existing literature. The overall bond strength thus can be estimated and verified against the values measured in the pull test described above. The model is finally used as a tool to develop a response surface model within the design margin.

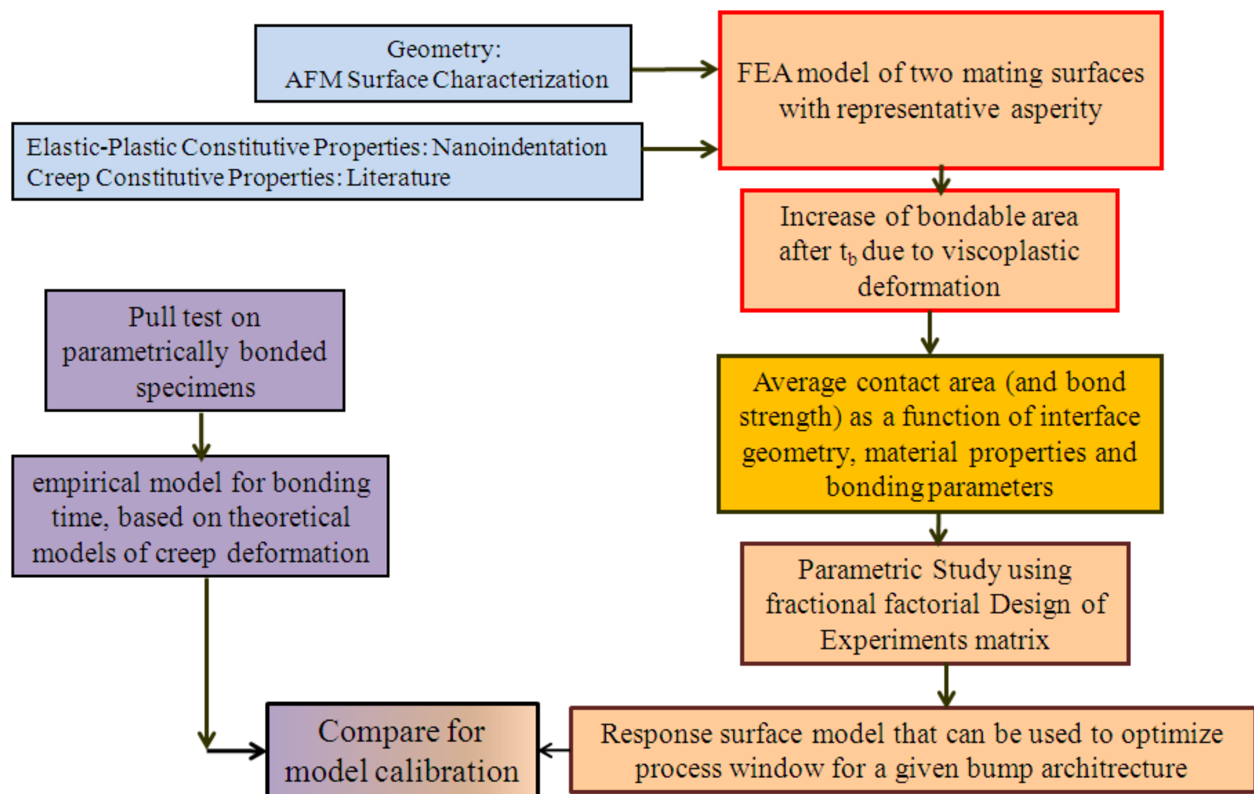

Figure 2-7: Investigation Flowchart

The work for this part of the thesis has been split into two journal papers. Paper 1 (in Chapter 3) focuses on experimental findings and corresponding development of the empirical model which has been fitted to the test data. It's important to mention that all the experimental data related to 6 kgf bonding force in this paper is not performed by the author of this dissertation. This is the first time it's being published in any journal and so has been included with the appropriate co-authors. Appropriate appendices are attached at the end of this dissertation to provide more details to some of the aspects of both experiments and modeling. Paper 2 (in Chapter 4) is then based on the development of a finite element model that takes material properties from a nanoindentation tests and existing literature. The model is calibrated to the test data in Paper 1. This is then used to perform a complete full blown DOE (Design of Experiment) and develop a response surface model based on the various bonding, roughness and material parameters.

References

1. Lau, J.; Wong, C.P.; Lee, N. and Lee, S.W., "Electronics Manufacturing with Lead-Free, Halogen-Free Conductive Adhesives," 1st Edition, McGraw Hill, 2002, ISBN: 0071386246.
2. Caers, J. F. J.; Zhao, X. J.; Sy, H. G.; Wong, E. H. and Mhaisalkar, S. G., "Towards a predictive behavior of nonconductive adhesive interconnects in moisture environment," in 54th Electronic Components and Technology Conference, Las Vegas, NV, 2004, pp. 106-112, DOI: 10.1109/ECTC.2004.1319322.
3. Haase, J., Iyer, P., Baumgartner, P., Farley, D., Dasgupta, A. and Caers, J., "Mechanics of Adhesively Bonded Flip-Chip-on-Flex Assemblies. Part I: Durability of Anisotropically

Conductive Adhesive Interconnect," Journal of Adhesion Science and Technology Vol 22, pp. 1733–1756, 2008, DOI: 10.1163/156856108X320564.

4. Farley, D.; Kahnert, T.; Sinha, K.; Solares, S.; Dasgupta, A.; Caers, J.F.J. and Zhao, X.J., "Cold welding: A new factor governing the robustness of adhesively bonded flip-chip interconnects," Proceedings, 59th Electronic Components and Technology Conference, 2009, pp. 67, DOI: 10.1109/ECTC.2009.5073998.
5. Obeid, I.; Morizio, J. C.; Moxon, K. A.; Nicolelis, M. A. L. and Wolf, P. D., "Two multichannel integrated circuits for neural recording and signal processing," IEEE Transactions on Biomedical Engineering, vol. 50, pp. 255-258, Feb 2003, DOI: 10.1109/TBME.2002.807643.
6. Aschenbrenner, R.; Gwiasda, J.; Eldring, J.; Zakel, E. and H. Reichl, "Gold Ball Bumps for Adhesive Flip Chip Assembly," in Adhesives in Electronics '94, VDI/VDE Tagung, 1994.
7. Holm R., "Electric Contacts Handbook", Springer-Verlag Berlin, 1958, 3rd ed., pp. 433.
8. Johnson, K. L.; Kendall, K. and Roberts, A. D., "Surface Energy and the Contact of Elastic Solids," Proceedings of the Royal Society of London, Series A, Vol. 324, No. 1558, 1971, pp. 301-313, DOI: 10.1098/rspa.1971.0141.
9. Cuthrell, R. E. and Tipping, D. W., "Electric Contacts. II. Mechanics of closure for gold contacts," Journal of Applied Physics, 44(10), 1973, pp. 4360-4365, DOI: 10.1063/1.1661964.
10. G. Garmong; N. E.P. Aton and A.S. Argon , "Attainment of Full Interfacial During Diffusion Bonding", Metallurgical and Materials Transactions A, Vol. 6, Number 6, 1269-1279, DOI: 10.1007/BF02658537.

11. Hamilton, C.H., “Superplastic Forming and Diffusion Bonding of Titanium Alloys”, Titanium Science and Technology, pp. 621-647, Plenum Press, New York, 1973, DOI: 10.1002/9780470686652.eae223.
12. A. A. L. White and D. J. Allen: in Proc. Conf. on 'Joining of metals', Vol. 2, 96; 1981, London, Institution of Metallurgists.
13. Derby, B. and Wallach, E. R., “Theoretical model for diffusion bonding”, Met. *Sci.,* 1982, 16, 49, DOI: http://dx.doi.org/10.1179/030634582790427028.
14. Derby, B. and Wallach, E. R., “Diffusion Bonding: Development of Theoretical model”, Met. Sci., Volume 18, Number 9, September 1984, pp. 427-431(5), DOI: http://dx.doi.org/10.1179/030634584790419809.
15. King W.H. and Owczarski W.A., “Diffusion Welding of Commercially Pure Titanium”, Welding Journal, 46 (1967) 289s.
16. Frost, H.J. and Ashby, M.F., “Deformation Mechanism Maps” Pergamon, Oxford 1982.
17. http://www.chemicool.com/elements/gold.html
18. http://www.kayelaby.npl.co.uk/general_physics/2_2/2_2_2.html
19. Needs R. J. and Mansfield M., “Calculations of the surface stress tensor and surface energy of the (111) surfaces of iridium, platinum and gold”, J. Phys.: Condens. Matter 1 (1989) 7555-7563, Printed in the UK, DOI: 10.1088/0953-8984/1/41/006.
20. Arcidiacono, S.; Bieri, N.R.; Poulikakos, D. and Grigoropoulos, C.P., “On the coalescence of gold nanoparticles”, International Journal of Multiphase Flow 30 (2004) 979-994, DOI: 10.1007/s11671-009-9298-6.

21. Lin, T.S. and Chung, Y.W., “Measurement of the activation energy for surface diffusion in gold by scanning tunneling microscopy”, Journal of Surface Science, Volume 207, Issues 2–3, 1 January 1989, Pages 539–546, DOI: 10.1016/0039-6028(89)90140-4.

22. Brown, C.; Rezvanian, O.; Zikry, M. A. and Krim, J., “Temperature dependence of asperity contact and contact resistance in gold RF MEMS switches”, J. Micromechanics and Microengineering, 19 (2009) 025006 (9pp), DOI: 10.1088/0960-1317/19/2/025006.

23. Sinha, K and Dasgupta A.,“Dependence of Bond Strength in Adhesively Bonded Flip-Chip Interconnects on Different Parameters: Part 2”, Proceeding paper in this issue.

24. Simon, S. L.; McKenna, G. B. and Sindt, O., “Modeling the Evolution of the Dynamic Mechanical Properties of a Commercial Epoxy During Cure after Gelation,” Journal of Applied Polymer Science, Vol. 76, 495–508 (2000)

25. Taylor, P. A.; Nelson, J. S. and Dodson, B. W.,"Adhesion between Atomically Flat Metallic Surfaces," Physical Review B, 44, 5834, 1991, DOI:10.1103/PhysRevB.44.5834

26. Sinha, K.; Farley, D.; Kahnert T.; Dasgupta A.; Caers J. F. J. and Zhao X.J., “Dependence of Bond Strength in Adhesively Bonded Flip-Chip Interconnects on Different Parameters: Part 1”, Preceding paper in this issue.

27. Ellis, T. W., “The Future of Gold in Electronics,” Gold Bulletin. Vol. 37, no. 1-2, pp. 66-71. 2004, DOI: 10.1007/BF03215518.

28. Ferguson G.; Chaudhury, M.; Sigal G. and Whitesides G., “Contact adhesion of thin gold films on elastomeric supports - Cold welding under ambient conditions,” Science, Vol. 253, pp. 776-778, 1991, DOI: 10.1126/science.253.5021.776.

29. Frisk, L. and Ristolainen, E., "Flip chip attachment on flexible LCP substrate using an ACF," Microelectronics Reliability 45 (2005) 583–588, DOI: http://dx.doi.org/10.1016/j.microrel.2004.10.009.

30. Teh L.K.; Wong C.C.; Mhaisalkar S.; Ong, K., Teo, P.S. and Wong, E.H., "Characterization of Nonconductive Adhesives for Flip-Chip Interconnection," Journal of Electronic Materials, Vol. 33, No. 4, pp. 271-276, 2004, DOI: 10.1007/s11664-004-0132-8.

31. Teo, M.; Mhaisalkar, S. G.; Wong, E. H.; Teo, P.-S.; Wong, C. C.; Ong, K.; Goh C. F. and Teh L. K., "Correlation of Material Properties to Reliability Performance of Anisotropic Conductive Adhesive Flip Chip Packages," IEEE Transactions on Components and Packaging Technologies, Vol. 28, No. 1, March 2005, DOI: 10.1109/TCAPT.2004.843175.

32. Yim M.J.; Hwang J.S.; Kwon W.; Jang K.W. and Paik, K.W., "Highly reliable nonconductive adhesives for flip chip CSP applications," Electronics Packaging Manufacturing, IEEE Transactions on, Vol. 26, No. 2, pp.150–155, April 2003, DOI: 10.1109/TEPM.2003.817715.

33. Yin, C.; Lu, H.; Bailey, C. and Chan, Y-C., "Effects of Solder Reflow on the Reliability of Flip-Chip on Flex Interconnections Using Anisotropic Conductive Adhesives," IEEE Transactions on Electronics Packaging Manufacturing, Vol. 27, No. 4, 2004, DOI: 10.1109/TEPM.2004.843152.

34. Aschenbrenner, R.; Miessner, R. and Reichl, H., "Adhesive flip chip bonding on flexible substrates," The First IEEE International Symposium on Polymeric Electronics Packaging, Oct 1997, DOI: 10.1109/PEP.1997.656478.

35. Chan, Y.C.; Hung, K.C.; Tang, C.W. and Wu, C.M.L., "Degradation Mechanisms of Anisotropic Conductive Adhesive Joints for Flip Chip on Flex Applications," Adhesive

Joining and Coating Technology in Electronics Manufacturing, 2000, DOI: 10.1109/ADHES.2000.860588.

36. Chiang, K.N.; Chang, C.W. and Lin, J.D., “Analysis of ACA/ACF package using equivalent spring method,” Electronics Packaging Technology Conference, 2000, DOI: 10.1109/EPTC.2000.906358.
37. Li, L. and Fang, T., “Anisotropic Conductive Adhesive Films for Flip Chip on Flex Packages,” Adhesive Joining and Coating Technology in Electronics Manufacturing, 2000, Proceedings on 4th International Conference, DOI: 10.1109/ADHES.2000.860586.
38. Ferrando, F.; Zaberli, J.F.; Clot, P. and Chenuz, J.M., “Industrial approach of a Flip-Chip method using the stud-bumps with a non-conductive paste,” Adhesive Joining and Coating Technology in Electronics Manufacturing, Proceedings. 4th International Conference on, pp. 205-211, 2000, DOI: 10.1109/ADHES.2000.860600.
39. Pajonk, J., “New flip chip technology utilizing non-conductive adhesive adapted for high volume chip card module production,” Electronics Manufacturing Technology Symposium, 2004, DOI: 10.1109/IEMT.2004.1321653.
40. Mercado, L. L.; White, J.; Sarihan V. and Lee, T., “Failure Mechanism Study of Anisotropic Conductive Film (ACF) Packages,” IEEE Transactions on Components and Packaging Technologies, Vol. 26, No. 3, September 2003, DOI: 10.1109/TCAPT.2003.817640.
41. Jang, C.; Han, S.; Kim, Y.; Kim, H.; Yoon, S.; Cho, S.; Han, C. and Han, B., “Development of Predictive Modeling Scheme for Flip-chip on Fine Pitch Flex Substrate,” EuroSimE 2005, DOI: 10.1109/ESIME.2005.1502868.

42. Kristiansen, H.; Gulliksm, M.; Haugerud, H. and Friberg, R., "Characterization of Electrical Contacts Made By Non-Conductive Adhesive," Adhesive Joining and Coating Technology in Electronics Manufacturing, 1998, DOI: 10.1109/ADHES.1998.742051.
43. Caers, J.; Zhao, X.; Wong E. and S. Mhaisalkar, "Towards a predictive behavior of non-conductive adhesive interconnects in moisture environment," ECTC 2004, DOI: 10.1109/ECTC.2004.1319322.
44. Chan, Y.C. and Luk, D.Y., "Effects of bonding parameters on the reliability performance of Anisotropic conductive adhesive interconnects for Flipchip-on-flex packages assembly II. Different bonding pressure," Microelectronics Reliability 42 (2002) 1195–1204, DOI: http://dx.doi.org/10.1016/S0026-2714(02)00089-6.
45. Fu, Y.; Wang, Y.; Wang, X.; Liu, J.; Lai, Z.; Chen, G. and Willander, M., "Experimental and theoretical characterization of electrical contact in anisotropically conductive adhesive," IEEE Transactions on Advanced Packaging, Vol. 23, No. 1, 2000, DOI: 10.1109/6040.826757.
46. Yeo, A.; Teo, M. and Lee, C., "Thermo- and Hydro-mechanical Modeling of an Adhesive Flip Chip Joint," Electronics Packaging Technology Conference, 2004, DOI: 10.1109/EPTC.2004.1396583.
47. Wu C.M.L.; Liu, J. and Yeung N.H., "Reliability of ACF in Flip-Chip with Various Bump Height," Adhesive Joining and Coating Technology in Electronics Manufacturing, 2000, DOI: 10.1109/ADHES.2000.860580.
48. Johnson, K.L., "Contact Mechanics", Cambridge: Cambridge University Press, 1985.
49. Johnson, K.L., "Contact Mechanics", Cambridge University Press , London, 1998.
50. Holm, R., "Electric Contacts: Theory and Applications", Berlin, Germany: Springer, 1969.

51. Dickrell, D.J.; Dugger, M.T.; Hamilton M.A. and Sawyer, W.G., "Direct Contact-Area Computation for MEMS Using Real Topographic Surface Data," J. Microelectromech. Syst., Vol.16, No.5, pp.1263-1268, Oct. 2007, DOI: 10.1109/JMEMS.2007.901120.
52. Chang, W.; Etison, I. and Bogy, D., “An elastic-plastic model for the contact of rough surfaces,” ASME J. Tribol., 109, pp. 257-263, 1987, DOI: http://dx.doi.org/10.1115/1.3261348.
53. Majumder, S.; McGruer N.E.; Adams, G.G.; Zavracky, P.M.; Morrison, R.H. and Krim, J., “Study of contacts in an electrostatically actuated microswitch,” Sensors and Actuators A, vol.93, no.1, pp. 19-26, 2001, DOI: 10.1109/HOLM.1998.722437.
54. Rezvanian, O.; Zikry, M.A.; Brown, C. and Krim, J., “Surface roughness, asperity contact and gold RF MEMS switch behavior,” J. Micromech. Microeng. 17, pp. 2006-2015, 2007, DOI: 10.1088/0960-1317/17/10/012.
55. Choi, Y. and Suresh, S., “Nanoindentation of patterned metal lines on a Si substrate”, Scripta Materialia 48, 249, 2003, DOI: http://dx.doi.org/10.1016/S1359-6462(02)00377-9.
56. Shan, Z. and Sitaraman, K., “Elastic-plastic characterization of thin films using nanoindentation techniques”, Thin Solid Films *437,* 176, 2003, DOI: http://dx.doi.org/10.1016/S0040-6090(03)00663-1.
57. Giannakopoulos, A. E.; Larsson P.-L. and Vestergaard, R., “Analysis of Vickers indentation", Int. J. Solids and Struct., 31, 2679-2708, 1994, DOI: http://dx.doi.org/10.1016/0020-7683(94)90225-9.
58. Larsson, P.-L.; Giannakopoulos, A. E.; So¨derlund, E.; Rowcliffe, D. J. and Vestergaard, R., “Analysis of Vickers indentation", Int. J. Solids Struct. 33, 221, 1996, DOI: 10.1016/0020-7683(95)00033-7.

59. Giannakopoulos, A. E. and Suresh S., “Determination of elastoplastic properties by instrumented sharp indentation”, Scripta Mater. 40, 1191, 1999, DOI: 10.1016/S1359-6462(99)00011-1.
60. Suresh, S. and Giannakopoulos, A. E., “A new method for estimating residual stresses by instrumented sharp indentation", Acta Materialia, vol. 46 (16), 1998, pp. 5755-5767, DOI: http://dx.doi.org/10.1016/S1359-6454(98)00226-2.
61. Frost, H.J. and Ashby, M.F., “Deformation Mechanism Maps” Pergamon, Oxford 1982.
62. Brown, C.; Rezvanian, O.; Zikry, M.A. and Krim, J., “Temperature dependence of asperity contact and contact resistance in gold RF MEMS switches”, J. Micromech. Microeng. 19 (2009) 025006 (9pp), DOI: 10.1088/0960-1317/19/2/025006.
63. Song, B.; Azarian, M.H.; Varghese, J.; Dasgupta, A. and Pecht, M., “Dynamic Loading Durability and Failure Site Transition in Enig-Sn37pb Interconnects in a Stacked Die BGA Package”, IEEE Transactions on Components and Packaging Technologies, 2006.
64. Xu, L. and Pang, J.H.L., “Effect of Intermetallic and Kirkendall Voids Growth on Board Level Drop Reliability for SnAgCu Lead-free BGA Solder Joint ”, Proceedings of the IEEE Electronic Components and Technology Conference, 275-282, 2006.
65. Yao, D. and Shang, J.K., “Effect of cooling rate on interfacial fatigue-crack growth in Sn-Pb solder joints”, IEEE Trans. Components, Packaging, and Manufacturing Technology, Part B, 19(1):, 154-165, 1996.
66. Evans A.G. and Hutchinson, J.W., “Effects of Non-Planarity on the Mixed Mode Fracture Resistance of Bimaterial Interfaces”, Acta Metallurgica, 1989. 37(3): p. 909- 916.
67. Rice, J. R., “Elastic Fracture Mechanics Concepts for Interface Cracks”, Journal of Applied Mechanics, 1988. 55: p. 98–103.

68. Suo, Z. and Hutchinson, J. W., “Sandwich Test Specimens for Measuring Interface Crack Toughness”, Materials Science & Engineering A: Structural Materials: Properties, Microstructure and Processing, 1989. A107 (1-2): p. 135-143.

69. Hutchinson, J. W. and Suo, Z., “Mixed Mode Cracking in Layered Materials. Advances in applied mechanics”, 1992. 29: p. 63-191.

70. Tu, P. L.; Chan, Y. C.; Hung, K. C. and Lai, J. K. L., “Growth Kinetics of Intermetallic Compounds in Chip Scale Package Solder Joints”, Scripta Materialia, 2001. 44(2): p.317-323.

71. Evans, A. G., Ruhle, M., Dalgleish, B. J. and Charalambides, P. G., “The fracture energy of bimaterial interfaces in Metal-Ceramic Interfaces”, 1990, Metall. Trans. *A* 21A:2419–29.

72. Wei, Y and Hutchinson, J. W., " Models of interface separation accompanied by plastic dissipation at multiple scales”, 1999, Int. J. Fract 95:1–17.

73. Suo, Z.; Shih, C. F. and Varias, A. G., “A theory for cleavage cracking in the presence of plastic flow”, Acta Metall. Mater., 1993, 41:1551–57.

74. Tvergaard, V. and Hutchinson, J. W., “Toughness of an Interface along a Thin Ductile Layer joining Elastic Solids”, 1994, Philos Mag. A 70:641–56.

75. Lane, M.W.; Dauskardt, R.H.; Vainchtein, A. and Gao, H. “Plasticity contributions to interface adhesion in thin-film interconnect structures”, 2000, J. Mater. Res. 15:2758–69.

76. Wei, Y. and Hutchinson, J.W., “Interface strength, work of adhesion and plasticity in the peel test." Int. J. of Fracture, 93, 315-333, (1998).

77. Jang, J.W.; Lin, J.K. and Frear, D. R., ‘Failure Morphology after the Drop Impact Test of the Ball Grid Array Package with Lead-Free Sn-3.8Ag-0.7Cu on Cu and Ni Under-Bump Metallurgies”, Journal of Electronic Materials, 2007. 36(3): p. 207-213.

78. Tu, P. L.; Chan, Y. C.; Hung, K. C. and Lai, J. K. L., "Growth Kinetics of Intermetallic Compounds in Chip Scale Package Solder Joints", Scripta Materialia, 2001. 44(2): p.317-323.

79. P. L. Liu and J. K. Shang, "A Comparative Fatigue Study of Solder/Electroless-Nickel and Solder/Copper Interfaces", Journal of Material Research, 2000. 15(11): p. 2347- 2355.

80. He, J.; Guo, Y. and Lin, Z., " Numerical and experimental analysis of thermosonic bond strength considering interfacial contact phenomena", Journal of Physics D: Applied Physics, vol. 41, 2008, 165304 (13pp), DOI:10.1088/0022-3727/41/16/165304.

81. Fu, X. and Chung, D.D.L., "Sensitivity of the bond strength to the structure of the interface between reinforcement and cement, and the variability of this structure", Journal of Cement and Concrete Research, Volume 28, Issue 6, June 1998, Pages 787-793, DOI: http://dx.doi.org/10.1016/S0008-8846(98)00055-6.

82. Bazhutin, N. B., G. K. Boreskov and V. I. Savchenko, "Adsorption of molecular and atomic oxygen on gold", React. Kinet. Catal. Lett., Vol. 10, No. 4,337-340 (1979), DOI: 10.1007/BF02075320.

83. Baker, T. A.; Xu B., Liu X.; Kaxiras E. and Friend, C.M., "Nature of Oxidation of the Au(111) Surface: Experimental and Theoretical Investigation", Journal of Physical Chemistry C Letters, 2009, *113,* 16561–16564, DOI: 10.1021/jp9052192.

84. Kahnert, T., "Au/Au bonding study for adhesively bonded flip chip packages," Master's Thesis, University of Applied Science Mannheim, 2008.

85. Farley, D.; Dasgupta, A. and Caers, J.F.J, "Mechanics of Adhesively Bonded Flip-Chip-on-Flex Assemblies. Part II: Effect of Bump Coplanarity on Manufacturability and Durability of Non-Conducting Adhesive Assemblies," Journal of Adhesion Science and Technology, *22,* 1757, 2008.

86. Haase, J., “Characterization of a Selected Anisotropic Conductive Adhesive,” M.S. Thesis, University of Maryland, College Park, Maryland, 2001.

87. Smith, J. R.; Bozzolo, G.; Banerjea, A. and Ferrante, J., “Avalanche in Adhesion,” Physical Review Letters, Vol. 63, No. 12, 1989.

88. Alcantar, N. A.; Park, C.; Pan, J-M. and Israelachvili, J. N., “Adhesion and coalescence of ductile metal surfaces and nanoparticles,” Acta Materialia 51 (2003)

89. Varghese, J., “Effect of Dynamic Flexural Loading on the Durability and Failure Site of Solder Interconnects in Printed Wiring Assemblies,” PhD Thesis, University of Maryland, College Park, Maryland, 2007.

90. Lane, M., “Interface Fracture”, Annu. Rev. Mater. Res, 2003, 33:29–54, DOI: 10.1146/annurev.matsci.33.012202.130440.

Chapter 3: Gold Bond Strength in Adhesively Bonded Flip-Chip Joints: Experimental Results and Empirical Model

In this chapter, test specimens bonded at various bonding conditions are pulled apart to estimate the growth rate of the bond strength with time. Literature [26, 27] suggests that the bond strength is directly related to the contact area. Thus, contact area is used as a proxy for the bond strength and a diffusion-assisted creep model of contact area as a function of bonding time is fitted to the experimentally measured bond strength. At the temperature and stress levels expected during the bonding process, bulk creep deformation was found to contribute much more than surface or interfacial diffusion, to the growth rate of the contact area. This model can be useful for predicting bond strength and thus for optimizing the process parameters for flip-chip bonding. The original draft of this chapter is a journal paper that will be submitted for peer-review to Journal of Adhesion Science and Technology.

Influence of Fabrication Parameters on Bond Strength in Adhesively Bonded Flip-Chip Interconnects Part I: Experimental Measurements

K.Sinha[1], D. Farley, T. Kahnert[1], S.Solares[2], A. Dasgupta[1], J. F. J. Caers[3] and X.J. Zhao[3]

[1]CALCE Electronic Products and Systems Consortium
[1,2]Mechanical Engineering Department
University of Maryland, College Park, MD, USA

[3]Philips Research, Electronic Packaging & Thin Film
Eindhoven, Netherlands

3.1 Abstract

This is Part I of a two-part paper investigating the contribution of Au-Au bond strength on the robustness of adhesively bonded flip-chip interconnects in microelectronic structures. The push

for miniaturization in microelectronics, coupled with conversion towards Pb-free electronics has led to increasing interest in adhesive bonding of flip-chip dies directly to printed wiring boards (PWBs) [1]. However, the interconnect strength and durability hasn't been adequately studied which hampers proper reliability assessment. Early theories suggested that degradation is by cyclic stress relaxation of the adhesive [2] but durability data from thermal cycling tests raised questions about this hypothesis and suggested the presence of direct metal-to-metal bonding instead [3]. To further explore this issue, detailed experiments are conducted in this study on specially fabricated specimens that consist of a pair of gold-bumped flip-chip dies that are bonded to each other without any adhesive between them. An experimental matrix is designed, where the bonding pressure, bonding temperature and bonding time are systematically varied within typical process windows, in order to attempt to understand the bonding mechanism(s). The specimens are characterized on an AFM to quantify the initial roughness of the bond pads, as well as the amount of plastic flattening that occurs locally at asperities ('a-spots') due to the application of the bonding force. Bonded specimens are then mounted and aligned in specially designed test fixtures and pulled apart to establish the bond strength. The average contact area is recorded through post failure destructive analysis, so that an average bonding strength can be measured as a function of different bonding parameters. The bond strength is found to increase with bonding pressure, bonding temperature and bonding time. The results suggest that bonding occurs by a sequence of plastic flattening at the Au-Au interfacial asperities, possibly followed by a time-dependent bonding mechanism. Theoretical diffusion models, commonly used in the literature for solid-state diffusion bonding studies, are found to provide a good fit to the experimental data. Since the temperature is too low for classical diffusion bonding between Au, a possible explanation is that the growth of bonding strength with bonding time/temperature, could

be partially due to creep-assisted growth of the area of atomistically flat contact ‘a-spots,’ followed by avalanche ‘cold welding’ [9]. Part II of this sequence will contain description and results of modeling and simulation, conducted to better understand and utilize these experimental results.

Keywords: Interconnect, Microelectronics, Welding, Durability, Pull, Strength, Flip-Chip, Diffusion

3.2 Introduction and Problem Statement

Flip chip bonding has existed for more than 30 years and is known for its advantages in miniaturization, high interconnect density, and improved electrical performance because of minimal lead length [5]. A flip chip electronic assembly is the direct electrical connection of face-down ("flipped") electronic dies onto a substrate. The interconnection method examined in this study uses adhesively bonded flat gold bumps, rather than solder connections [6], because of the low cost and low process temperatures (curing temperatures for the adhesive are usually < 200°C). Non-conductive adhesives are increasingly replacing conductive adhesives as an important bonding method to avoid bridging and shorts across neighboring bumps for very fine I/Os. However, all the underlying bonding mechanisms are not fully understood here.

Conventional hypothesis suggests that interconnection between mating bumps is achieved by mechanical compressive forces caused by curing-induced shrinkage of the adhesive [1]. Subsequent degradation and loss of reliability during temperature cycling was believed to be due to cyclic viscoeleastic relaxation of the epoxy, with accompanying loss of contact force and consequent rise in contact resistance. However, in a former experimental study, Haase [3] reported that the only change in interconnect electrical resistance measured during temperature

cycling of a flip-chip-on-flex assembly, bonded with Anisotropic Conductive Adhesive (ACA), was solely due to that caused by the temperature-dependence of the bulk resistivity of the metals in the interconnect system, not by any changes in the interfacial resistance. This suggested that the viscoelastic relaxation of the contact force had no effect on the contact resistance. Haase concluded that there must be some interfacial metal-to-metal bonding mechanism such as mechanical interlocking of mating asperities due to local compressive plastic deformations, or metallurgical "cold welding" [7]. The material system explored by Haase consisted of Au plated soft conductive particles, and gold metallization on the mating interconnect pads on the chip and substrate. The aim of the present study is to further explore the nature of this interfacial Au-Au contact and to examine how it may contribute to the robustness of the adhesively bonded interconnect.

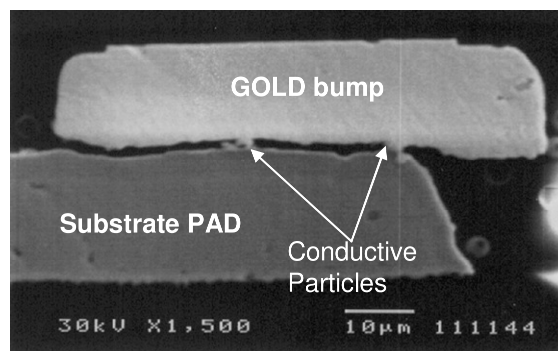

Figure 3-1: FCOF Interconnect Bonded with Conductive Adhesive. Conductive Particles are Used to Complete the Circuit.

Fig. 3-1 shows an ACA interconnection between a gold bump and substrate pad. The conductive connection is facilitated by the spring-action of the compliant conductive particles in the ACA. In this study the attention is on Au bumps bonded with NCA (Non Conductive Adhesive). Fig. 3-2 shows a Non Conductive Adhesive (NCA) interconnection between a gold bump and substrate pad. The conductive connection here is by direct contact between the two

metal (gold, in this study) surfaces which is facilitated by plastic deformation of asperities on one or both Au surfaces during the bonding process.

Figure 3-2: FCOF Interconnect Bonded with Non-Conductive Adhesive (NCA)

The nature of the interfacial bonding is of great interest in this case since the interfacial stresses are higher than in ACAs, because of the absence of the compliant particles. The experimental study presented here suggests that the observed interfacial solid-state bonding process can be explained not by plastic mechanical interlocking but instead by creep-assisted growth of contact area, followed by 'cold-welding'. In Part II of this sequence, the bonding process will be modeled to explore the role of the surface topology and other bonding parameters on the observed bond strength.

Section 3.3 below summarizes the current literature on the experimental findings and diffusion models for solid-state bonding. Section 3.4 explains the overall approach of this study. Sections 3.5 to 3.9 provide details of the pull test setup, sample types and sample surface topology characterization. Section 3.10 presents the details of the pull-test results. In Section 3.11, an empirical model is derived from solid-state diffusion theory and fitted to the experimental results of Section 3.10.

3.3 Literature Review

The Au-Au bonding process in adhesively bonded flip chip interconnects is believed to be a result of cold-welding across atomistically flat ‘a-spots’ that are caused by elastic-plastic deformation followed by diffusion-driven growth of the contact area. The literature on these phenomena is reviewed here to understand the nature and history of the study of solid state bonding. Most of the studies test specific package geometry and report package-specific reliability data, or that their package simply passed a certain number of temperature cycles without going into further detail [43-53]. Mercado, et al. studied the failure mechanisms of ACF bonded packages, but concluded that the reliability was strongly dependent on moisture, and therefore ignored temperature cycling [54].

3.3.1 Cold Welding

Soft metals such as copper or gold owe their coherence largely to metallic bonds. They are able to transfer material from one surface to another if separated. Johnson, Kendall, and Roberts [40] reported what became known as the JKR equation for determining the surface energy of materials in contact [8]. Johnson, et al. reported that, although surface roughness masks the deformation produced by attractive forces in normal metals, for soft metals that difficulty does not manifest. Cuthrell [41] tested the bonding strength of an aluminum alloy and investigated the mechanics of the a-spot formation. He pressed two annealed aluminum hemispheres under high vacuum and room temperature together and observed that existing cold welds under a load at room temperature can grow, resulting in an increased contact area, decreased contact resistance, and increased tensile strength [9]. In the experiments conducted in this study, the dependence of this bond strength on bonding time (at two different bonding temperatures) provided important evidence of the possible presence of diffusion-assisted metallurgical bonding between the two

gold bumps.

3.3.2 Contact Area or "A-Spot"

The conductive connection emerges through "full" contact between the two surfaces, which is facilitated by plastic deformation of asperities on one or both Au surfaces during the bonding process [7]. If two contact members are pressed together by a load the initial contact points, induced by the surfaces roughness, becomes enlarged from small contact areas since the materials (gold) are deformable. Simultaneously, new contact points emerge by deforming the voids elastically and/or plastically that lowers the voids coming into contact. These areas are called a-spots and their sum results in the total load-bearing area A_b, while the entire interface is the apparent contact area A_a [7, 24]. The interfaces between these contact areas are almost atomistically flat and are called "a-spots." The flatness over the "a-spot" is important since it governs the probability of solid-state bonding at these regions [25].

3.3.3 Diffusion Bonding Mechanisms

Diffusion bonding is a solid-state joining process capable of bonding together a wide range of small and large metal and ceramic part combinations. Joints may be autogenous, that is, between two pieces of the same metal or alloy or they may be between different metals or non-metals. In all cases it is necessary to invoke the interatomic forces within the metals which are responsible for their cohesion. Since these forces are effective only within a range of the order of 10 Å, the metal surfaces must be as free as possible from adsorbed or other impurities [10]. When cold welding is at low deformations for short times, `necks' of welded material are interspersed with voids. As the temperature is increased after contact has been established, various diffusional processes take place. First, surface diffusion, which is not so temperature dependent, allows material to move into and enlarge the `necks' of the contact areas. According to this work [10],

more temperature dependent processes of grain boundary and volume diffusion occur next, which on the whole has little effect on the bond strength until temperature approaches the melting point. However, current study shows contradictory findings where even at relatively lower temperature, bulk diffusion plays a dominant role in the bond strength growth. This will be further discussed later on in this paper. Diffusion can be markedly accelerated (by as much as three orders of magnitude) when a suitable metal is used as an intermediate between the two pieces of metal to be joined. Two special attributes of gold contribute to making it the easiest of metals to bond to other metals by the simple application of pressure and or heat at temperatures below its melting point. These are firstly its ductility, and secondly the fact that it does not form oxide films on its surface, even when heated in air.

Modeling of diffusion bonding has been carried out by several authors [10-14]. First phenomenological model due to King and Owczarski [15] generated insights that have guided much later work. In the earlier approaches [10-12] only one or two mechanisms for diffusion bonding were considered and some relationships were restricted to specific alloys. New models are often based on improvement of the limitations of this in two aspects: void shape and diffusion bonding mechanism. Hamilton et al. [91] attempted to quantify the initial plastic deformation by representing surface roughness as a series of long ridges. Gamong et al. [92] extended Hamilton's analysis by modeling the ridge as a series of horizontal slices and summing the response of each slice to the applied stress. A more recent model proposed by Derby and Wallach [13, 14] has included all possible bonding mechanisms (Fig. 3-3) and the predictions have shown reasonable agreement with the experimental results for copper and iron.

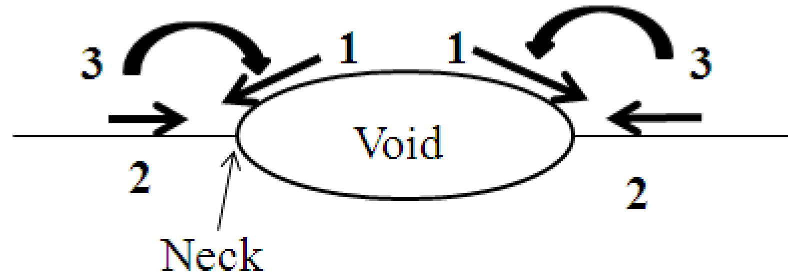

Figure 3-3: Schematic View of Growing Bond Showing Routes of Three Mechanisms of Mass Transfer [13]

Derby and Wallach modeled the original surface as a series of long parallel straight-sided ridges. This geometry is highly idealized and has limited capability for realistic representation of rough Au surfaces. In their work, the total bonding time was taken as the sum contribution of 3 individual mechanisms:

1. Surface & Volume diffusion from surface sources to a neck
2. Surface & Volume Diffusion along the bond interface from interfacial sources to a neck
3. Power law creep deforming the ridge

Derby and Wallach simplify the bonding process into two main stages: (1) the interfacial void turns from a diamond shape to a cylindrical shape; (2) the cylindrical void gradually shrinks and closes. The Derby-Wallach model is adapted and extended in this study because of its comprehensive features and wide acceptance in the literature.

3.4 Overall Approach

The flowchart in Fig. 3-4 illustrates our overall approach to the problem. Specially designed Au-Au bonded flip-chip specimens were fabricated at various bonding conditions, based on a

carefully designed process matrix intended to highlight the parametric influence of process variables on interfacial bonding. The parameters being investigated include: bonding force, bonding temperature, bonding time. The surface roughness and topography of the gold bump is carefully characterized to explain its role on the bond strength and for subsequent model development. Pull tests are conducted on all the bonded specimens to quantify the interfacial strength of the bond, as a function of different bonding conditions. Cross-sectioning, microscopic analysis, and dye penetrant studies are used on the tested specimens, to investigate the features of the metallurgical interconnection. An empirical diffusion model is developed by modifying the Derby-Wallach model for solid-state diffusion-assisted interfacial bonding [13, 14]. This model is found to provide a reasonably good fit to the experimental data, suggesting that solid diffusion is potentially one of the dominant contributors to the bonding process. For this fitting process, bond strength observed experimentally is scaled here to the area fraction in contact with full contact denoting saturated strength. This is based on the assumption that the bond strength is directly related to the contact area and that the process of 'cold welding' can be almost instantaneous if the contact surfaces are atomistically flat. The literature [80, 81] supports this scaling process. Details of the experimental approach, results of the tests and the fitting of the empirical bonding model are discussed in the remainder of this paper. Part II of this sequence will contain description and results of modeling and simulation, conducted to better understand the role of the surface topologies on the bond strength.

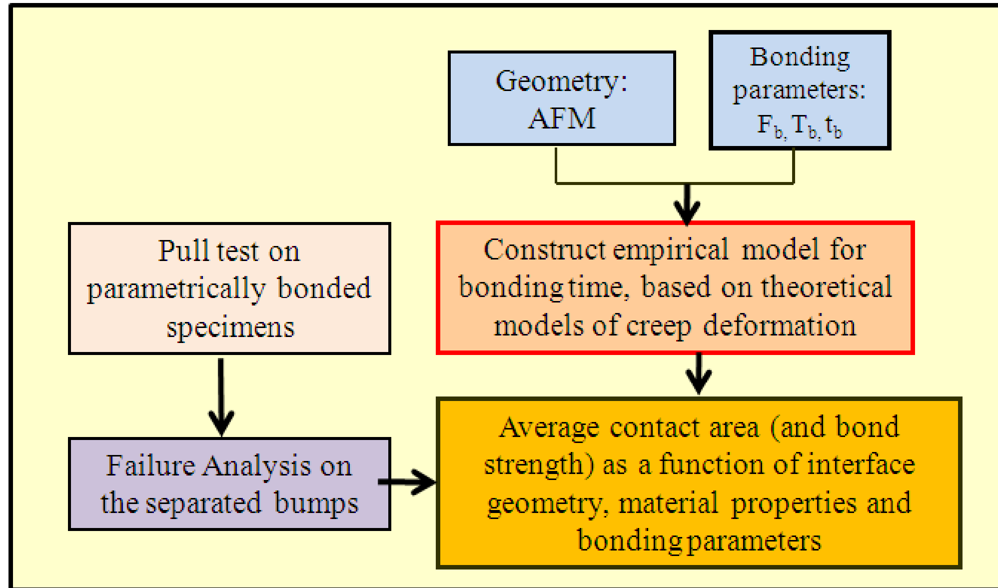

Figure 3-4: Investigation Flowchart

3.5 Test Specimens

Specially designed test specimens (Appendix 1 of [39]) are fabricated to study the effect of various bonding parameters on the interface strength in the flip-chip joint. The specimen consists of two silicon dies with matching gold bumps, bonded together under different bonding conditions, without any adhesive. In actual application, these dies are usually bonded to matching gold-plated copper pads on a flex or rigid substrate, and held in place with an adhesive. For test purposes, two dies are attached to each other without any adhesive (as shown in Fig. 3-5), to isolate and measure the interfacial strength between the matching gold bumps.

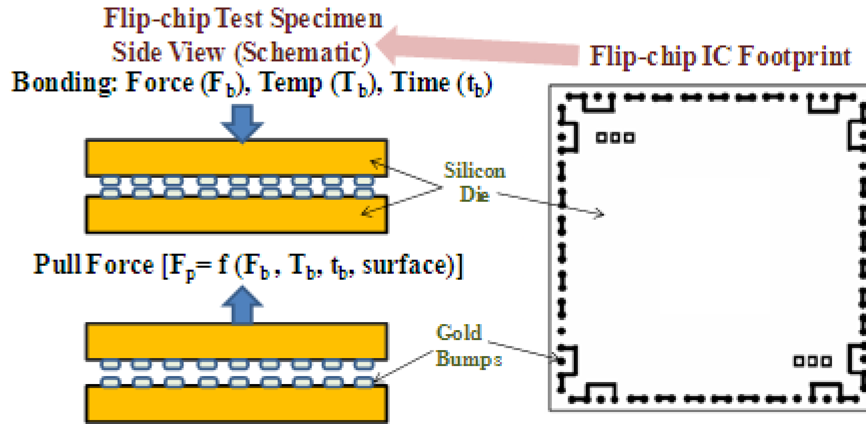

Figure 3-5: Test Specimen Preparation

The size of the entire die is 5 by 5 mm with 84 bumps overall spread out along all 4 edges, as shown in Figure 3-6 (Appendix 1 of [39]). Each bump here has an octagonal footprint with geometric details shown in Figure 3-7. The distance between the parallel sides varies from 86µm to 89µm. The idealized contact surface varies from $6.13\text{x}10^{-3}$ mm^2 to $6.57\text{x}10^{-3}$ mm^2. Since the bumps are asymmetrically placed on the die, as shown in Figure 3-6, it is not possible to align every bump with a mating one on the opposing die. As a result, 58 of 84 bumps are connected while the remaining 26 are not. Fig. 3-7 shows the bump design and indicates with a red box the bumps that do not mate with the opposite chip. Thus, only 69% of the total number of bumps bond with mating bumps.

Furthermore, due to placement misalignment during specimen fabrication, there was only partial overlapping between the mating bumps. In order to estimate the misalignment, some of the pull-test specimens were selected for dye-penetrant tests to estimate the actual contact surface area. The dye penetrant study gave an idea about the real contact area; microscopic analysis showed the alignment of chips to each other as well as the approximate alignment of the bonding force. A close look at the bumps confirms that roughly 65% of the bumps are in contact because of the misalignment between the mating dies, as shown in Figure 3-7.

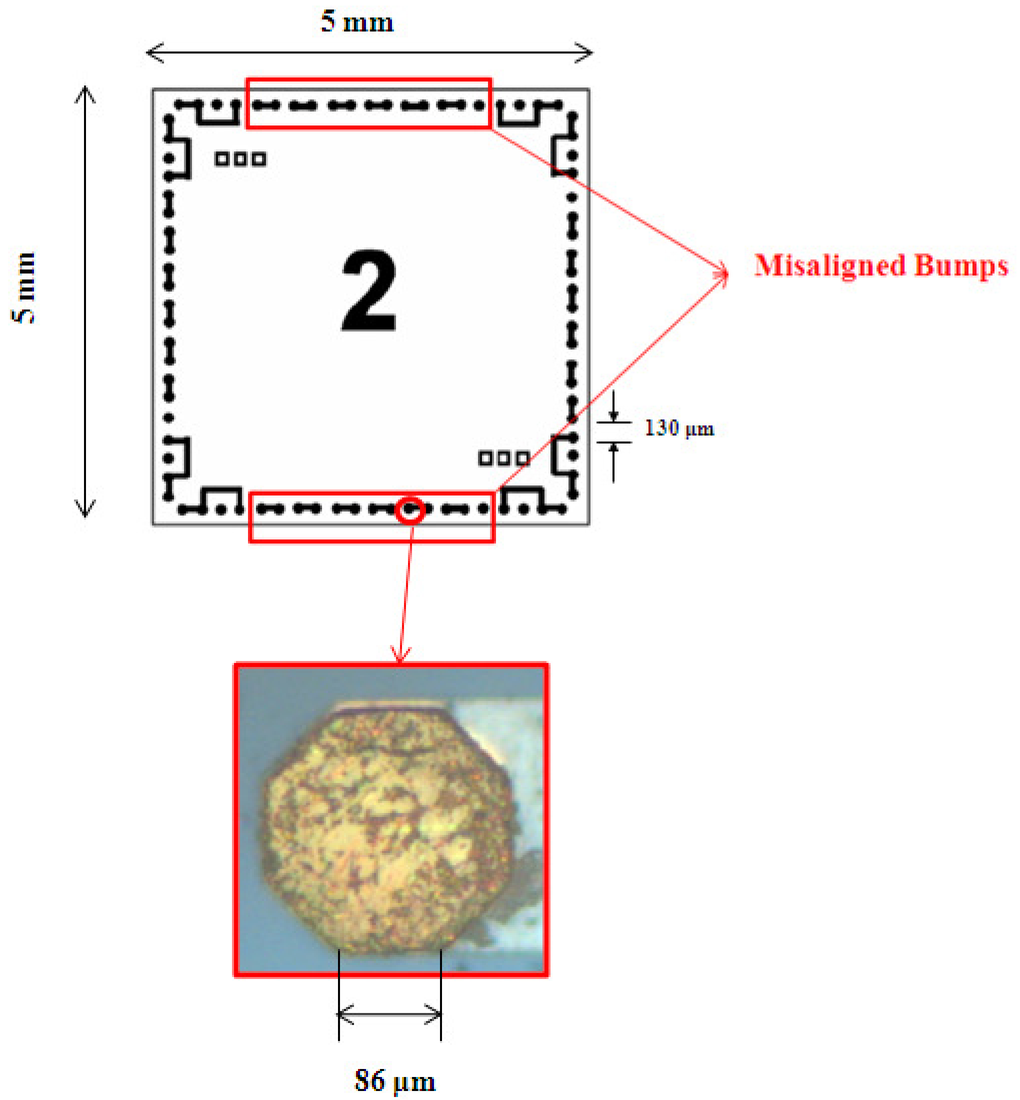

Figure 3-6: Test Specimens with Dimensions and Bump Alignment Scheme. Joints in the red boxes do not mate with the opposing chip.

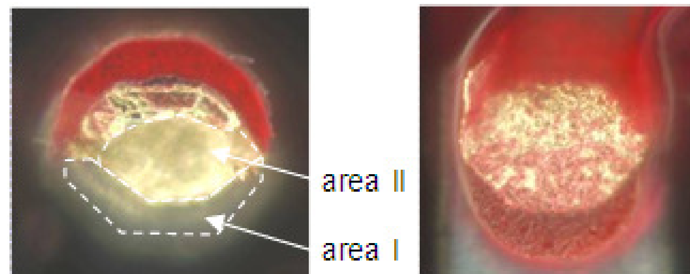

Figure 3-7: Die Penetrant Test

This mating area is important for accurately estimating the contact pressure on the bonding surfaces. The bonding parameters are listed in the next section.

3.6 Bonding Process Matrix

Specimens were fabricated by parametrically varying the bonding force, bonding temperature and bonding time, to examine their effect on the interfacial strength.

The bonding force affects the amount of plastic deformation of the asperities, thus increasing the "diameter" of a-spots up to 200% and also flattening the asperities (and reducing the effective surface roughness). This plastic flattening forms atomistically flat interfacial contacts. The bonding forces used in this study are 4 Kgf, 6 Kgf and 8 Kgf.

The bonding temperature is important, as the activation energy for diffusion and creep is provided by thermal energy. An Arrhenius model [42] effectively explains the dependency. Since the activation energy is constant, the diffusion coefficient is strongly dependent on the temperature:

$$D = D_0 \cdot e^{-\frac{Q}{RT}} \qquad (3\text{-}1)$$

D_0 = Diffusion constant

Q = Activation energy for self diffusion

R = General gas constant

T = Diffusion temperature

The bonding temperature is limited by the properties of the substrate (glass transition temperature etc.) and the die. Two different bonding temperatures are considered in this study: 200°C and 250°C.

The bonding time has a strong influence on the diffusion distance. The diffusion distance x is proportional to the square root of the product of diffusion coefficient D and diffusion time t:

$$x = \sqrt{D \cdot t} \tag{3-2}$$

The bonding time was parametrically varied from 1 sec to 120 sec. To understand the effect the temperature, some of the 6 Kgf samples were made at 250°C. Table 3-1 gives further details of the specimen sets made available for these experiments.

Temp (°C)	Force (Kgf)	t (sec)
200	4	10
200	4	20
200	4	30
200	4	40
200	4	50
200	4	60
200	4	70
200	4	80
200	4	90
200	4	100
200	4	110
200	4	120

Temp (°C)	Force (Kgf)	t (sec)
200	6	1
200	6	5
200	6	10
200	6	15
200	6	16
200	6	17
200	6	18
200	6	19
200	6	20
200	6	20
200	6	25
200	6	30
200	6	120

Temp (°C)	Force (Kgf)	t (sec)
200	8	2
200	8	4
200	8	6
200	8	8
200	8	10
200	8	12
200	8	14
200	8	16
200	8	18
200	8	20
200	8	30
200	8	60
200	8	120

Temp (°C)	Force (Kgf)	t (sec)
250	6	10
200	6	15
200	6	20
200	6	25

Table 3-1: Specimen Matrix

3.7 Characterization of Gold Bump Surface Topology

The roughness of the bump surfaces before and after plastic flattening by the bonding force is characterized with an Atomic Force Microscope (AFM). These measurements were made on samples that had failed to bond (due to insufficient bonding time) and had some initial misalignment. As discussed in Section 3.6, the misalignment resulted in partial overlap of

bumps. Thus a part of each bump was plastically deformed by the mating force while the remaining exposed part retained the original surface roughness. These two sets of surface measurements provide important insights into the role of the initial surface roughness on the bond strength and also into the amount of plastic flattening that occurs when the two surfaces are forced into contact by the applied bonding force.

A tapping mode AFM image was acquired from the sample surface. The tip diameter used was 10 nm and the cantilever force constant was about 2 N/m. At first a 90 by 90 micron scan of the bumps was used to obtain a qualitative over-view of the two kinds of surfaces in the same bump. This also helped confirm the suitability of the bumps selected for more detailed characterization. Fig. 3-8 shows such a scan with the exposed half clearly showing higher roughness and also higher average height, than the mated half.

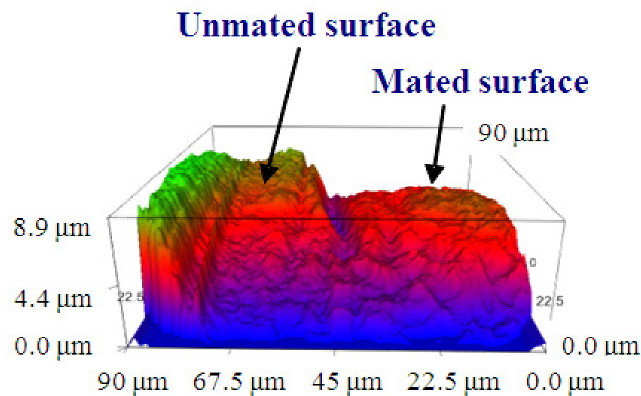

Figure 3-8: AFM Side-View Image of a Gold Bump

Once the whole bump was imaged, the individual halves were separately characterized with multiple times more resolution (same pixel size of 256 by 256 but for a smaller scan area). Mostly, these scan-zones had a size of 25 by 25 microns. Fig. 3-9 shows that there is a big contrast in the roughness profiles before and after deformation due to plastic flattening.

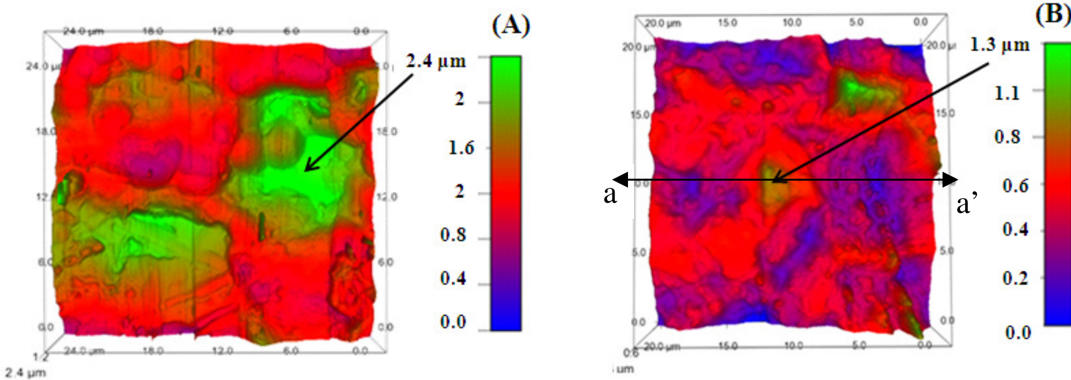

Figure 3-9: AFM Images of (A) an Unmated Surface and (B) a Mated Surface

Six scans were performed over the smaller sub-regions, three each for unmated and mated surfaces (details in Appendix 4 of [39]). The statistics of the resulting roughness parameters are listed in Table 3.2. Clearly the mean and RMS roughness changed significantly with plastic deformation. The average RMS roughness height is 0.22 microns for the unmated region and 0.12 microns after the plastic flattening in the mated region. The third (skewness) and fourth (kurtosis) moments of the roughness profile also changed. In order to estimate the initial RMS roughness wavelength, 2D surface profiles were generated at the equatorial region of the scanned images (section a-a' in Fig. 3-9). Three cross-sections were chosen from three different mated bumps characterized at their equatorial regions. Based on the number of major peaks and the surface length, the wavelengths of the surface profiles are estimated. The wavelength values ranged from 4 to 5 micron. An approximate estimate of 4.5 microns was obtained as the average wavelength of the unmated surfaces. These values are used in the empirical model discussed in the next section and also in the detailed modeling reported in Paper II of this two part series.

Roughness Parameters	Unmated Surface			Mated Surface		
	Average	Min	Max	Average	Min	Max
Mean	63 nm	0 nm	192 nm	14 nm	0 nm	68 nm
RMS	218 nm	116 nm	430 nm	124 nm	23 nm	244 nm
Skewness	0.13	-0.46	0.8	-0.38	-2.7	1.6
Kurtosis	2.12	2	4.2	3.1	2.4	5

Table 3-2: Final Statistics of the Surface Topology from AFM Measurements

3.8 Pull test Setup and Procedure

The bonded flip chip specimens were pulled apart on a commercial multipurpose bond tester ; which provides directional pull/push options as well as shear options. In this experiment a pull test cartridge has been used with the standard pull option in the z-direction. Specially designed fixtures are used to hold and align the small flip-chip specimens (Appendix 3 of [39]). The machine is used with a 10 Kg pull test cartridge and a hook on its front. The hook is the interface between the cartridge and adaptor. The pull test parameters are as follows:

- Deformation rate: 0.1μm/s
- Maximum test force: 10 Kg

To minimize transient stresses, a slow test speed is used. The maximum force is chosen to be as low as possible, to ensure the highest possible resolution. The details of the specification of the pull tester have been listed in Appendix 2 of [39].

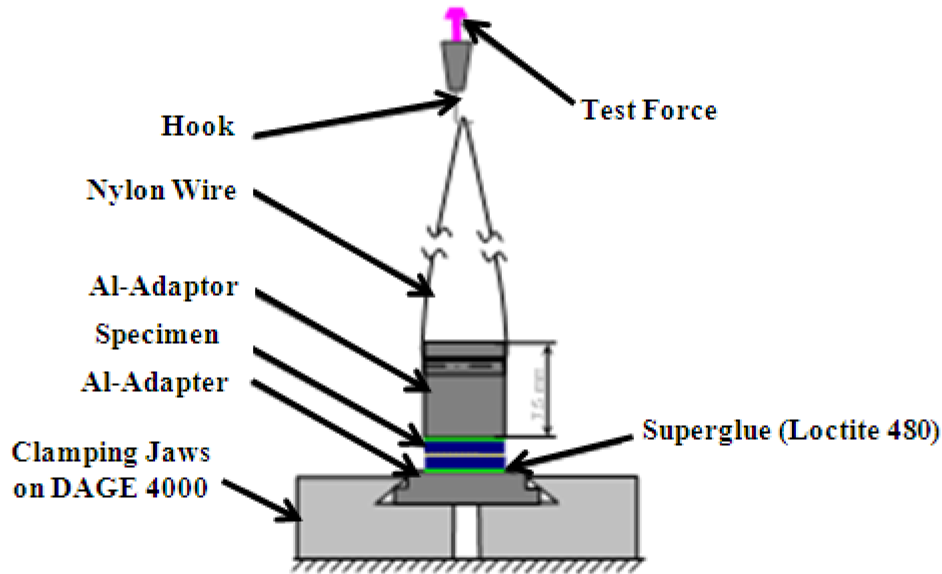

Figure 3-10: Experimental Setup

3.9 Specimen Adaptor

The specimens are fragile because they are bonded together only at the gold-gold interface and not with any adhesive. Therefore, specimens have to be mounted very carefully in the test machine to avoid accidental overstress during this process. This means that the installation of the fixture on the test specimen, as well as the mounting of the fixture on the testing machine should be executed without any accidental over-load to the specimen. The distribution of the testing force should be constant over the die, which is square (5x5 mm). Figure 3-1. shows a schematic of the final testing configuration. The specimen is mounted between two milled Aluminum adaptors, with superglue which has a very low viscosity. This ensures that the adhesion layer is very thin, and the risk of angular misalignment is minimal. The required bonding pressure during mounting is also minimized. The upper Aluminum-adapter has a drill hole in the middle to attach a Nylon wire to it. The prepared specimen and adaptors are fixed in clamping jaws on the table of the pull tester, to ensure that the Al-Adapter is mounted sufficiently flat. The Nylon wire on

the upper adapter connects the hook to the cartridge. To align the hook to the adapter the table is moveable. The top of the upper specimen adaptor has a cross which shows the midpoint where the hook has to be moved to by adjusting the table. Once the assembly is aligned the pull test can begin. Detailed specifications of the fixture design (on which the specimens were glued) are in Appendix 3 of [39].

The failure analysis and pull strength estimates from these tests are discussed in the next two sections.

3.10 Pull Strength Results

The maximum pull force at failure is recorded and used to estimate the average interfacial pull strength. The maximum fracture load was 3286 gf for 120s bonding time at 8 Kgf bonding force. Based on the number of bumps in contact, this translates to a bonding force per bump of 38.7 gf. Considering the 65% misalignment, discussed earlier, this translates to an average interface pull strength of 130 MPa at each bump. The fact that the steady-state contact strength approaches the tensile strength of bulk soft gold (130 MPa), suggests a metallic bond between the surfaces.

The pull test results (Figures 3-11 and 3-12) show that the bond strength is strongly dependent on bonding-temperature, bonding force and bonding time. Figure 3-11 shows how the dependence on bonding time changes with bonding force, for bonding temperature of 200°C. Figure 3-12 shows how the dependence on bonding time changes with bonding temperature, for bonding force of 6 Kgf [4].

Figure 3-11 shows an initial incubation period of about 15-20 seconds (at 200°C) before the interface begins to develop bond strength. After this initial period the bond strength increases rapidly. The growth rate slowly decreases and at about 120 seconds, the interfacial bond strength asymptotically saturates approximately at the strength of bulk gold (130 MPa). The incubation

period and bonding time (time to reach saturated value) decreases sharply at 250°C, as shown in in Figure 3-12. These trends are explored later in Section 3.11 with the analytic Derby-Wallach model and later again in Part II of this sequence with more detailed computational models that better capture actual surface topologies.

There appears to be significant scatter in the data because of loading eccentricities and misalignments, caused by manufacturing tolerances of the adapter and alignment of the test vehicle on the pull-testing machine. Also the scatter can come from variations in contact geometry because of the misalignments during the bonding.

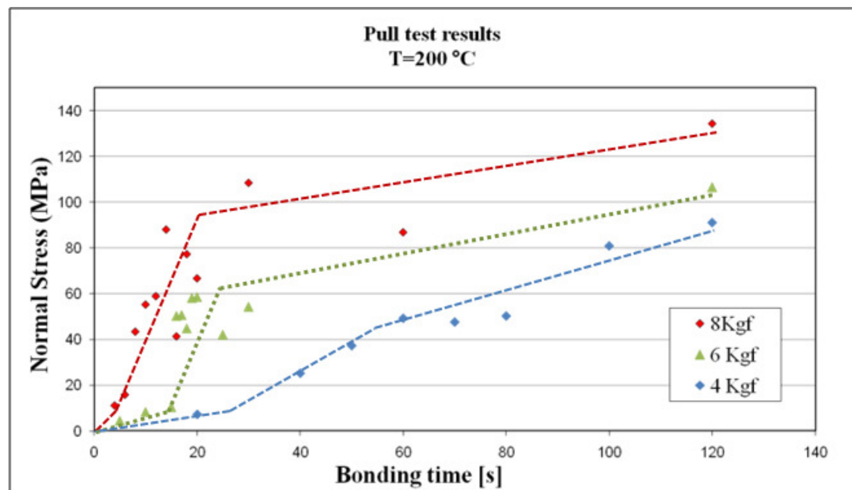

Figure 3-11: Normalized Pull Test Results (All Specimens)

The comparative fracture strength of the specimens with the elevated temperature of 250°C & 200°C is shown in Fig. 3-12 [4]. A probable reason behind the change in slope is that higher temperature causes higher diffusion rates. As a result, the contact area can grow faster, resulting in faster 'cold-welding' at the interface, thus requiring shorted bonding periods to reach the

maximum saturated bond strength. Also the elevated temperature could have produced more plastic deformation of the asperities on the surface this increasing the initial surface contact.

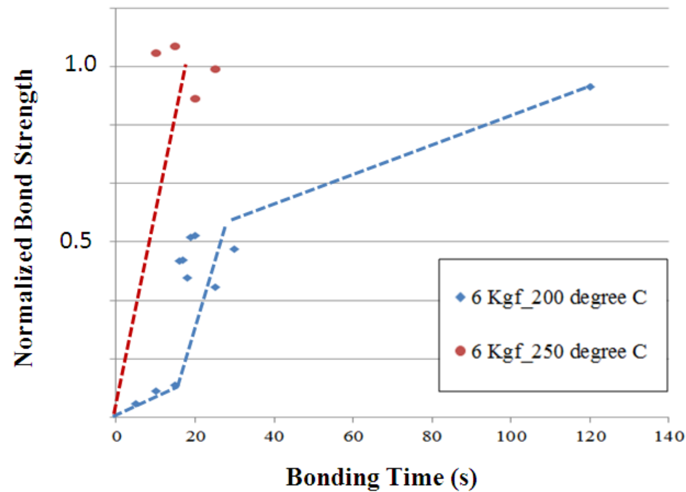

Figure 3-12: Normalized Pull Test Results (Effect of Temperature) [4]

3.11 Empirical Bonding Model

The experimental results show a definitive trend in the change of bond strength with respect to the different bonding parameters (bonding time, bonding temperature and bonding force). Clearly, process engineers will benefit from a simple parametric response-surface model that can predict bond strength, based on the process variables. The best model will be one that is based on simple fundamental theory of the bonding process and has empirical model constants that can be obtained from the data presented in this paper. Therefore this paper focuses on models in the literature that have successfully modeled diffusion bonding processes before. One of the critical tasks will be to verify if this model sufficiently captures the observed dependencies of the bonding strength on bonding parameters. The theoretical basis of the model is discussed in the Subsection 3.11.1 and the model calibration is discussed in Subsection 3.11.2.

3.11.1 Theoretical Basis for Bonding Model

The Derby-Wallach model [13, 14], previously discussed in Section 3.3.3, provides a good framework for parametric representation of the test results presented earlier in Section 3.10. This model is modified in this study to develop an empirical model for Au-Au bonding at low temperatures. The modification process consists of two steps. The first step involves down-selecting which of the multiple diffusion mechanisms, suggested by Derby and Wallach, play a significant role in this particular flip chip bonding problem. The second step involves fitting an empirical model derived from the dominant mechanism(s) of the first step.

The bond strength scales with the area fraction in contact [26, 27], with full contact denoting saturated strength. The initial contact of asperities leads to plastic deformation because of the bonding force, causing an initial contact area f_o in Eqn. (3-3). The three mechanisms (as explained in section 3.3.3) act in parallel and so the area fraction changes from time t to t+Δt due to the sum of the contribution of each of them. Eqn. (3-3) is a mathematical representation of this. The weight factors, w_1, w_2 and w_3 represent the percentage contribution from each individual mechanisms while f_1, f_2, f_3 are the area fractions at t+Δt, if these mechanisms operated separately.

$$w_1 f_1(t+\Delta t) + w_2 f_2(t+\Delta t) + w_3 f_3(t+\Delta t) + f_o = f(t+\Delta t) \tag{3-3}$$

Wallach and Derby derived the rate of increase in bonded area for each individual mechanism. This was transformed to rate of increase in fraction of bonded area and integrated numerically for small time steps. The area fraction at each time step was then expressed as a weighted sum

along with the contribution from the plastic deformation, to get the final area fraction at every time step.

The coefficients w_i are model constants and are calculated by fitting this bond area model to the measured bond strength reported in Section 3.11. Under the bonding conditions, the bulk creep deformation is found to have orders of magnitude higher contribution to interfacial bonding. Fig. 3-13 shows comparative contact area vs time curves at the expected temperature and stress level in the bonding process, based on gold properties available in the literature (see Table A1-1 in Appendix 1). It's clear that the creep mechanism has an order of magnitude higher contribution than the other two mechanisms, to the growth of the contact area (and hence to bond strength). This agrees with Derby-Wallach's own experimental fits [14]. The detailed derivations for contact area growth rates as per the Derby Wallach model are in Appendix 5 of [39]. The physical constants for gold used here are tabulated in the Appendix 1.

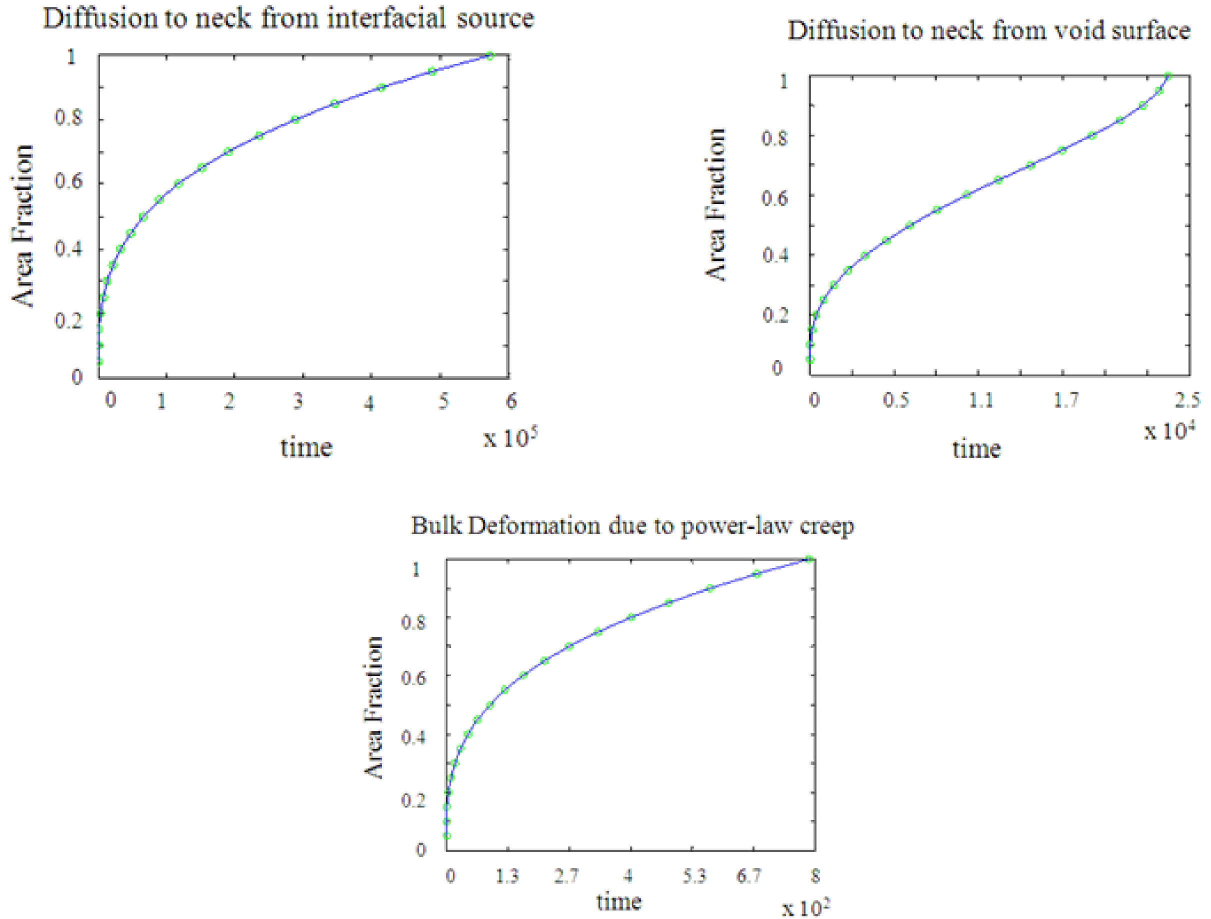

Figure 3-13: Contact Area Fraction vs Bonding Time Trends for Different Mechanisms as per Derby Wallach Model [13]

The creep term of the Derby Wallach model is therefore used to describe the growth rate of the contact area as a function of time. The details of the derivation are in Appendix 1 which has 3 model constants and takes bonding force, bonding temperature, bonding time, RMS roughness height and RMS roughness wavelength as inputs. The final model, shown in Eqn. (3-4) is derived in Appendix 1.

$$t = t_o + \frac{1}{6}A\frac{h}{b}Tx(t)e^{B/T}(6n^2 x(t)^{\frac{2}{n}}(-\frac{x(t)(Cn - nP + P)}{2(n+1)} + \frac{n(C-P)}{n+2} + \frac{Px(t)^2}{3n+2}) + 3x(t)(Cn - nP + P) - 6n(C-P) - 2Px(t)^2)$$
$$-\frac{1}{6}A\frac{h}{b}Tf_o e^{B/T}(6n^2 f_o^{\frac{2}{n}}(-\frac{f_o(Cn - nP + P)}{2(n+1)} + \frac{n(C-P)}{n+2} + \frac{Pf_o^2}{3n+2}) + 3f_o(Cn - nP + P) - 6n(C-P) - 2Pf_o^2) \quad (3\text{-}4)$$

where,

A, B, C: Model Constants

f_o: Initial Area Fraction (Model Constant)

t_o: Minimum time required to form any substantial strength (Model Constant)

x(t): Instantaneous Area Fraction

t: Bonding Time

P: Bonding Load

b: Half of bonded length between two adjacent voids (Half of average wavelength from the AFM measurement)

h: Half of interfacial cavity height (RMS roughness in the AFM measurement)

T: Bulk Temperature

3.11.2 Empirical Determination of Model Constants

This model is next fitted to the experimental results at 200°C bonding temperature, to estimate the model constants A, B, C, t_o, f_o. The experimental results obtained are in terms of total bond strength. This is first converted to normalized contact area by normalizing the strength with the saturated bond strength. This is based on the assumption that the saturated strength denotes full contact. The constants have a least square fit across all bonding forces. The model constants are shown in Table 3-3. The experimental data and this model matched reasonably well in all 3 cases

of 200°C (Fig. 3-14) and 6 Kgf bonding force at 250°C (Fig. 3-15). The best match was for the 6 Kgf bonding force. The integration constant (t_o), denoting the initial incubation period, increases with decreasing bonding force. This is the minimum time required to attain any measurable strength and may be the time required to reduce traces of oxygen atoms on the surface. Thus, for this gold to gold bonding, the model's predictions agree reasonably with experimental results, based on power-law creep deformation.

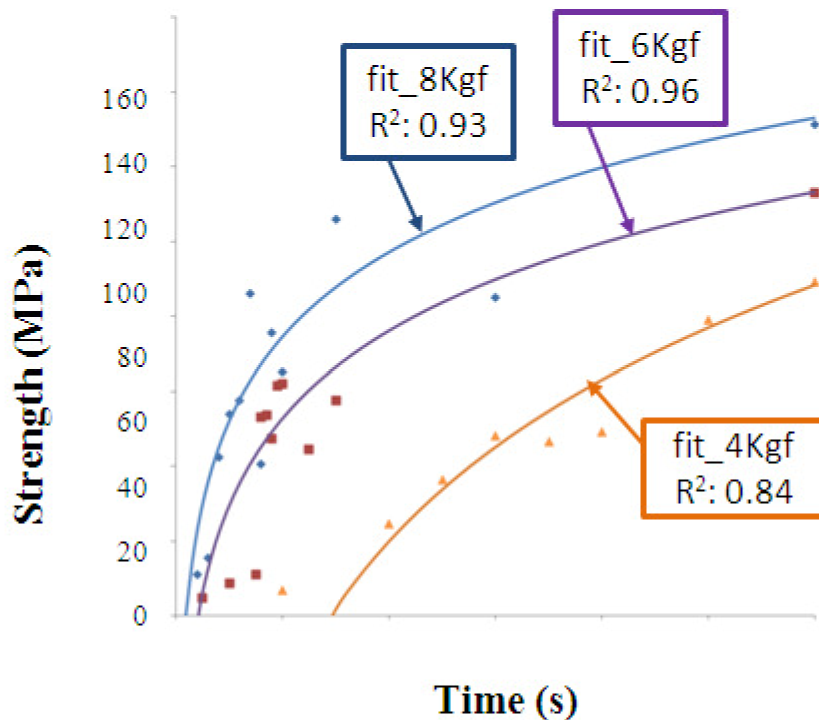

Figure 3-14: Model Fitted with the Experimental Data at Various Bonding Forces (200°C)

Interestingly, irrespective of the bonding force, the contact area corresponding to this time lag period is about 22% of the full contact. This time lag can be possibly traced to the energy required to reduce the oxygen atoms that form a thin layer on the gold surface and stays constant irrespective of the bonding parameters. This hypothesis needs to be verified in future studies using experiments and/or atomistic simulations.

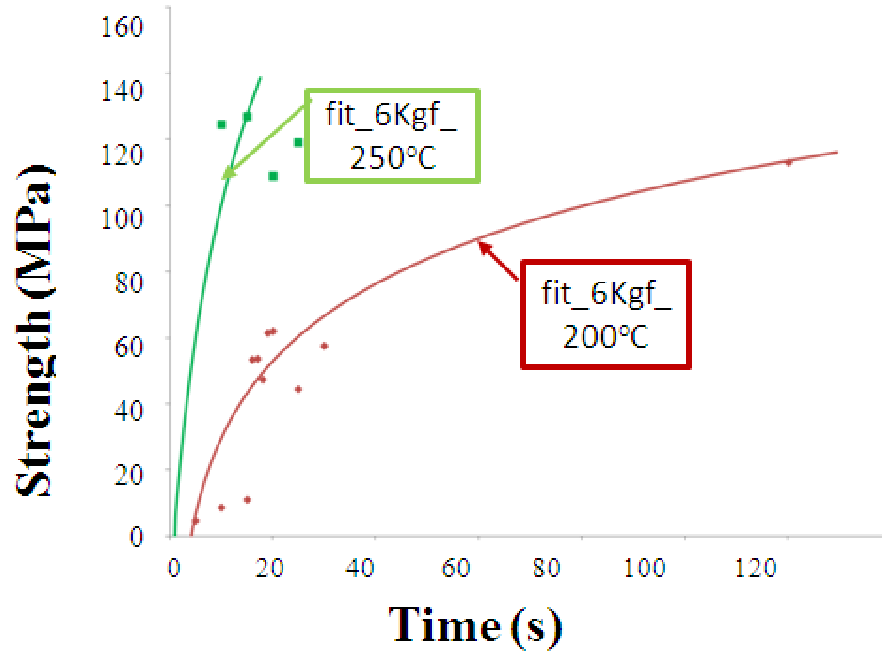

Figure 3-15: Model Fitted with the Experimental Data at Various Bonding Temperatures (250°C)

Table 3-3 shows the values of A, B, C, t_o and f_o for different bonding forces. The values in the brackets denote the statistical scatter of these model constants for a 95% confidence bound. With only 5 model constants and involving all of the bonding parameters, it is a comprehensive model that can be a useful prediction tool for the bond strength in similar metallic bonds where creep deformation plays the major role.

Bonding Force (Kgf)	A (Kg $m^{-1} s^{-1} K^{-1}$)	B (Kg $m^{2} s^{-2} K^{-1}$)	C (Kg $m^{-1} s^{-3}$)	t_o (s)	f_o
8 (@200°C)	1.9 x 10^{-14} (0.9E-14, 2.9E-14)	10.62 (8.2, 12.9)	0.843 (0.71, 0.97)	2.3 (2.1, 2.5)	0.071 (0.052, 0.09)
6 (@200°C)	1.9 x 10^{-14} (0.65E-14, 3.2E-14)	10.62 (9.7, 11.4)	0.843 (0.76, 0.92)	4.7 (4.5, 4.9)	0.042 (0.033, 0.51)
6 (@250°C)	1.9 x 10^{-14} (0.2E-14, 3.6E-14)	10.62 (7.1, 14.1)	0.843 (0.55, 1.13)	1.1 (0.69, 1.67)	0.11 (0.085, 0.37)
4 (@200°C)	1.9 x 10^{-14} (0.3E-14, 3.5E-14)	10.62 (7.9, 13.2)	0.843 (0.61, 1.07)	29.5 (26, 33)	0.03 (0.015, 0.45)

Table 3-3: Empirical Model Constants (95% Confidence Bounds Presented in Parentheses)

3.12 Summary and Conclusions

This study experimentally explores the contribution of Au/Au bond strength on the integrity of adhesively bonded flip chip interconnects as a function of the different bonding parameters (force, temperature and time). The results suggest that diffusion-assisted power-law bulk creep deformation can explain the contact area (and bond strength) growth rate as a function of the bonding parameters. The bond strength grows and saturates at the strength of bulk gold. Higher bonding force or bonding temperature makes the strength of the bond grow and saturate faster. There is an initial incubation period for the strength to develop, suggesting perhaps, the presence of a chemical species on the surface that has to be removed for bonding to occur. This threshold period decreases proportionally with higher bonding force. An empirical model based on the basic principles of diffusion bonding shows good match with the experimental data. It was found that power-law creep deformation has the major influence on interfacial contact area growth at the interface. This mechanism shows a close correlation with the measured interfacial strength development. This model can be useful in the prediction of the robustness of adhesively bonded flip-chip interconnects and thus in process parameter optimizations in the manufacturing of such flip-chip assemblies.

Acknowledgments

The work reported here was sponsored by the members of the Electronic Products and Systems Consortium at the Center for Advanced Life Cycle Engineering at the University of Maryland.

References

1. Lau, J.; Wong, C.P.; Lee, N. and Lee, S.W., "Electronics Manufacturing with Lead-Free, Halogen-Free Conductive Adhesives," 1st Edition, McGraw Hill, 2002, ISBN: 0071386246.
2. Caers, J. F. J.; Zhao, X. J.; Sy, H. G.; Wong, E. H. and Mhaisalkar, S. G., "Towards a predictive behavior of nonconductive adhesive interconnects in moisture environment," in 54th Electronic Components and Technology Conference, Las Vegas, NV, 2004, pp. 106-112, DOI: 10.1109/ECTC.2004.1319322.
3. Haase, J., Iyer, P., Baumgartner, P., Farley, D., Dasgupta, A. and Caers, J., "Mechanics of Adhesively Bonded Flip-Chip-on-Flex Assemblies. Part I: Durability of Anisotropically Conductive Adhesive Interconnect," Journal of Adhesion Science and Technology Vol 22, pp. 1733–1756, 2008, DOI: 10.1163/156856108X320564.
4. Farley, D.; Kahnert, T.; Sinha, K.; Solares, S.; Dasgupta, A.; Caers, J.F.J. and Zhao, X.J., "Cold welding: A new factor governing the robustness of adhesively bonded flip-chip interconnects," Proceedings, 59th Electronic Components and Technology Conference, 2009, pp. 67, DOI: 10.1109/ECTC.2009.5073998.
5. Obeid, I.; Morizio, J. C.; Moxon, K. A.; Nicolelis, M. A. L. and Wolf, P. D., "Two multichannel integrated circuits for neural recording and signal processing," IEEE Transactions on Biomedical Engineering, vol. 50, pp. 255-258, Feb 2003, DOI: 10.1109/TBME.2002.807643.
6. Aschenbrenner, R.; Gwiasda, J.; Eldring, J.; Zakel, E. and H. Reichl, "Gold Ball Bumps for Adhesive Flip Chip Assembly," in Adhesives in Electronics '94, VDI/VDE Tagung, 1994.
7. Holm R., "Electric Contacts Handbook", Springer-Verlag Berlin, 1958, 3rd ed., pp. 433.

8. Johnson, K. L.; Kendall, K. and Roberts, A. D., "Surface Energy and the Contact of Elastic Solids," Proceedings of the Royal Society of London, Series A, Vol. 324, No. 1558, 1971, pp. 301-313, DOI: 10.1098/rspa.1971.0141.
9. Cuthrell, R. E. and Tipping, D. W., "Electric Contacts. II. Mechanics of closure for gold contacts," Journal of Applied Physics, 44(10), 1973, pp. 4360-4365, DOI: 10.1063/1.1661964.
10. G. Garmong; N. E.P. Aton and A.S. Argon , "Attainment of Full Interfacial During Diffusion Bonding", Metallurgical and Materials Transactions A, Vol. 6, Number 6, 1269-1279, DOI: 10.1007/BF02658537.
11. Hamilton, C.H., "Superplastic Forming and Diffusion Bonding of Titanium Alloys", Titanium Science and Technology, pp. 621-647, Plenum Press, New York, 1973, DOI: 10.1002/9780470686652.eae223.
12. A. A. L. White and D. J. Allen: in Proc. Conf. on 'Joining of metals', Vol. 2, 96; 1981, London, Institution of Metallurgists.
13. Derby, B. and Wallach, E. R., "Theoretical model for diffusion bonding", Met. *Sci.,* 1982, 16, 49, DOI: http://dx.doi.org/10.1179/030634582790427028.
14. Derby, B. and Wallach, E. R., "Diffusion Bonding: Development of Theoretical model", Met. Sci., Volume 18, Number 9, September 1984, pp. 427-431(5), DOI: http://dx.doi.org/10.1179/030634584790419809.
15. King W.H. and Owczarski W.A., "Diffusion Welding of Commercially Pure Titanium", Welding Journal, 46 (1967) 289s.
16. Frost, H.J. and Ashby, M.F., "Deformation Mechanism Maps" Pergamon, Oxford 1982.
17. http://www.chemicool.com/elements/gold.html
18. http://www.kayelaby.npl.co.uk/general_physics/2_2/2_2_2.html

19. Needs R. J. and Mansfield M., "Calculations of the surface stress tensor and surface energy of the (111) surfaces of iridium, platinum and gold", J. Phys.: Condens. Matter 1 (1989) 7555-7563, Printed in the UK, DOI: 10.1088/0953-8984/1/41/006.

20. Arcidiacono, S.; Bieri, N.R.; Poulikakos, D. and Grigoropoulos, C.P., "On the coalescence of gold nanoparticles", International Journal of Multiphase Flow 30 (2004) 979-994, DOI: 10.1007/s11671-009-9298-6.

21. Lin, T.S. and Chung, Y.W., "Measurement of the activation energy for surface diffusion in gold by scanning tunneling microscopy", Journal of Surface Science, Volume 207, Issues 2–3, 1 January 1989, Pages 539–546, DOI: 10.1016/0039-6028(89)90140-4.

22. Brown, C.; Rezvanian, O.; Zikry, M. A. and Krim, J., "Temperature dependence of asperity contact and contact resistance in gold RF MEMS switches", J. Micromechanics and Microengineering, 19 (2009) 025006 (9pp), DOI: 10.1088/0960-1317/19/2/025006.

23. Sinha, K and Dasgupta A.,"Dependence of Bond Strength in Adhesively Bonded Flip-Chip Interconnects on Different Parameters: Part 2", Proceeding paper in this issue.

24. Simon, S. L.; McKenna, G. B. and Sindt, O., "Modeling the Evolution of the Dynamic Mechanical Properties of a Commercial Epoxy During Cure after Gelation," Journal of Applied Polymer Science, Vol. 76, 495–508 (2000)

25. Taylor, P. A.; Nelson, J. S. and Dodson, B. W.,"Adhesion between Atomically Flat Metallic Surfaces," Physical Review B, 44, 5834, 1991, DOI:10.1103/PhysRevB.44.5834

26. He, J.; Guo, Y. and Lin, Z., " Numerical and experimental analysis of thermosonic bond strength considering interfacial contact phenomena", Journal of Physics D: Applied Physics, vol. 41, 2008, 165304 (13pp), DOI:10.1088/0022-3727/41/16/165304.

27. Fu, X. and Chung, D.D.L., "Sensitivity of the bond strength to the structure of the interface between reinforcement and cement, and the variability of this structure", Journal of Cement and Concrete Research, Volume 28, Issue 6, June 1998, Pages 787-793, DOI: http://dx.doi.org/10.1016/S0008-8846(98)00055-6.

28. Bazhutin, N. B., G. K. Boreskov and V. I. Savchenko, "Adsorption of molecular and atomic oxygen on gold", React. Kinet. Catal. Lett., Vol. 10, No. 4,337-340 (1979), DOI: 10.1007/BF02075320.

29. Baker, T. A.; Xu B., Liu X.; Kaxiras E. and Friend, C.M., "Nature of Oxidation of the Au(111) Surface: Experimental and Theoretical Investigation", Journal of Physical Chemistry C Letters, 2009, *113,* 16561–16564, DOI: 10.1021/jp9052192.

30. Kahnert, T., "Au/Au bonding study for adhesively bonded flip chip packages," Master's Thesis, University of Applied Science Mannheim, 2008.

31. Farley, D.; Dasgupta, A. and Caers, J.F.J, "Mechanics of Adhesively Bonded Flip-Chip-on-Flex Assemblies. Part II: Effect of Bump Coplanarity on Manufacturability and Durability of Non-Conducting Adhesive Assemblies," Journal of Adhesion Science and Technology, *22,* 1757, 2008.

32. Haase, J., "Characterization of a Selected Anisotropic Conductive Adhesive," M.S. Thesis, University of Maryland, College Park, Maryland, 2001.

33. Smith, J. R.; Bozzolo, G.; Banerjea, A. and Ferrante, J., "Avalanche in Adhesion," Physical Review Letters, Vol. 63, No. 12, 1989.

34. Alcantar, N. A.; Park, C.; Pan, J-M. and Israelachvili, J. N., "Adhesion and coalescence of ductile metal surfaces and nanoparticles," Acta Materialia 51 (2003)

35. Varghese, J., "Effect of Dynamic Flexural Loading on the Durability and Failure Site of Solder Interconnects in Printed Wiring Assemblies," PhD Thesis, University of Maryland, College Park, Maryland, 2007.
36. Lane, M., "Interface Fracture", Annu. Rev. Mater. Res, 2003, 33:29–54, DOI: 10.1146/annurev.matsci.33.012202.130440.
37. Hamilton, C. H., "Pressure requirements for diffusion bonding titanium", Proceedings of the Second International Conference, Cambridge, Mass; United States; 2-5 May 1972. pp. 625-648. 1973
38. Garmong, G.; Paton, N. E. and Argon, A. S., "Attainment of Full Interfacial Contact during Diffusion Bonding", Metallurgical Transactions A Volume 6A, June 1975-1269
39. Sinha, K., "Mechanics of Non Planar Interfaces in Flip-Chip Interconnects," PhD Thesis, University of Maryland, College Park, Maryland, 2012
40. Johnson, K. L.; Kendall and K., Roberts, A. D., "Surface Energy and the Contact of Elastic Solids," Proceedings of the Royal Society of London, Series A, Vol. 324, No. 1558, 1971.
41. Cuthrell, R. E. and Tipping D. W., "Electric Contacts. II. Mechanics of closure for gold contacts," Journal of Applied Physics, 44(10), 1973.
42. Laidler, K. J., "The Development of the Arrhenius Equation", Journal of Chemical Education, Vol. 61, Number 6, June 1984.
43. Frisk, L. and Ristolainen, E., "Flip chip attachment on flexible LCP substrate using an ACF," Microelectronics Reliability 45 (2005) 583–588, DOI: http://dx.doi.org/10.1016/j.microrel.2004.10.009.

44. Teh L.K.; Wong C.C.; Mhaisalkar S.; Ong, K., Teo, P.S. and Wong, E.H., "Characterization of Nonconductive Adhesives for Flip-Chip Interconnection," Journal of Electronic Materials, Vol. 33, No. 4, pp. 271-276, 2004, DOI: 10.1007/s11664-004-0132-8.

45. Teo, M.; Mhaisalkar, S. G.; Wong, E. H.; Teo, P.-S.; Wong, C. C.; Ong, K.; Goh C. F. and Teh L. K., "Correlation of Material Properties to Reliability Performance of Anisotropic Conductive Adhesive Flip Chip Packages," IEEE Transactions on Components and Packaging Technologies, Vol. 28, No. 1, March 2005, DOI: 10.1109/TCAPT.2004.843175.

46. Yim M.J.; Hwang J.S.; Kwon W.; Jang K.W. and Paik, K.W., "Highly reliable nonconductive adhesives for flip chip CSP applications," Electronics Packaging Manufacturing, IEEE Transactions on, Vol. 26, No. 2, pp.150–155, April 2003, DOI: 10.1109/TEPM.2003.817715.

47. Yin, C.; Lu, H.; Bailey, C. and Chan, Y-C., "Effects of Solder Reflow on the Reliability of Flip-Chip on Flex Interconnections Using Anisotropic Conductive Adhesives," IEEE Transactions on Electronics Packaging Manufacturing, Vol. 27, No. 4, 2004, DOI: 10.1109/TEPM.2004.843152.

48. Aschenbrenner, R.; Miessner, R. and Reichl, H., "Adhesive flip chip bonding on flexible substrates," The First IEEE International Symposium on Polymeric Electronics Packaging, Oct 1997, DOI: 10.1109/PEP.1997.656478.

49. Chan, Y.C.; Hung, K.C.; Tang, C.W. and Wu, C.M.L., "Degradation Mechanisms of Anisotropic Conductive Adhesive Joints for Flip Chip on Flex Applications," Adhesive Joining and Coating Technology in Electronics Manufacturing, 2000, DOI: 10.1109/ADHES.2000.860588.

50. Chiang, K.N.; Chang, C.W. and Lin, J.D., "Analysis of ACA/ACF package using equivalent spring method," Electronics Packaging Technology Conference, 2000, DOI: 10.1109/EPTC.2000.906358.

51. Li, L. and Fang, T., "Anisotropic Conductive Adhesive Films for Flip Chip on Flex Packages," Adhesive Joining and Coating Technology in Electronics Manufacturing, 2000, Proceedings on 4th International Conference, DOI: 10.1109/ADHES.2000.860586.

52. Ferrando, F.; Zaberli, J.F.; Clot, P. and Chenuz, J.M., "Industrial approach of a Flip-Chip method using the stud-bumps with a non-conductive paste," Adhesive Joining and Coating Technology in Electronics Manufacturing, Proceedings. 4th International Conference on, pp. 205-211, 2000, DOI: 10.1109/ADHES.2000.860600.

53. Pajonk, J., "New flip chip technology utilizing non-conductive adhesive adapted for high volume chip card module production," Electronics Manufacturing Technology Symposium, 2004, DOI: 10.1109/IEMT.2004.1321653.

54. Mercado, L. L.; White, J.; Sarihan V. and Lee, T., "Failure Mechanism Study of Anisotropic Conductive Film (ACF) Packages," IEEE Transactions on Components and Packaging Technologies, Vol. 26, No. 3, September 2003, DOI: 10.1109/TCAPT.2003.817640.

Appendix 1: Calculation of Creep Diffusion Empirical Model

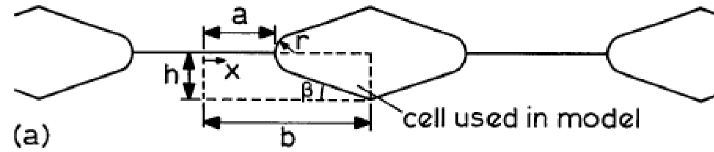

Figure A1-1: Contacting Surfaces Modeled as Small Cells due to Assumed Symmetry (Derby et al.)

List of Symbols-

a: Half of interfacial void width

A: Modified creep constant

A_c: Strain rate power law creep constant

A_c' : Creep constant from uniaxial creep testing

b: Half of bonded length between two adjacent voids (Half of average wavelength from the AFM measurement)

h: Half of interfacial cavity height (RMS roughness in the AFM measurement)

k: Boltzmann's constant

Q_v: Activation energy of volume diffusion

t: Bonding time

T: Bonding Temperature

P: Bonding Force

γ: Surface Tension

R: Universal Gas Constant

μ: Chemical Potential

S: Sign of Bonding Pressure (negative for compression)

V: Volume transferred in bonding

b_v : Modulus of the burgers vector

$\dot{V}$: Rate of change of V with respect to time

f: Fraction of Bonded Area

Following are the values of gold for the above material parameters:

Parameters	Unit	Value	Reference
Atomic Volume	Ω (m^3)	1.7×10^{-29}	[17]
Burgers Vector	b_v (m)	2.56×10^{-10}	[16]
Shear Modulus	μ_o (Mpa)	2.7×10^4	[18]
Melting Temperature	T_m (K)	1337.33	[17]
Temperature coeff. of shear modulus	(K)	4×10^{-4}	[18]
Density	ρ (Kg m^{-3})	19.32×10^3	[17]
Surface Energy	γ (J m^{-2})	1.25	[19]
Bulk Diffusion Coeff	D_v (m^3 sec^{-1})	3×10^{-5}	[20]
Bulk Diffusion Activation Energy	Q_v (KJ mol^{-1})	207	[16]
Grain-Boundary Diffusion Coeff	$\delta_B D_B$ (m^3 sec^{-1})	5×10^{-15}	[16]
Grain-Boundary Diffusion Activation Energy	Q_B (KJ mol^{-1})	105	[16]
Surface Diffusion Coeff.	$\delta_s D_s$ (m^3 sec^{-1})	6×10^{-10}	[16]
Surface Diffusion Activation Energy	Q_s (KJ mol^{-1})	88	[21]
Power-Law Creep Constant	A (hr^{-1})	1.9×10^{-15}	[22]
Power-Law Creep Exponent	n_c	7	[22]

Table A1-1: Gold Property Constants

From the Derby-Wallach derivation for bulk creep deformation-

$$\dot{V} = \frac{\sqrt{3} S A_c a^2 \tan\beta}{2[1-(\frac{a}{b})^{2/n_c}]^{n_c}} \left\{ \frac{2[P(\frac{b}{a}-1)-\frac{\gamma}{a}]}{\mu n_c} \right\}^{n_c} \tag{A1-1}$$

$$\dot{h} = -\frac{\dot{V}}{a} \tag{A1-2}$$

$$\dot{a} = -\frac{\dot{h}}{h}(b+a) \tag{A1-3}$$

Combining Eqn. (A1-2) & (A1-3)

$$\dot{V} = -\dot{h}\,a = \frac{a\,\dot{a}\,h}{(b+a)} \tag{A1-4}$$

Combining Eqn. (A1-1) & (A1-4)

$$\frac{a\,\dot{a}\,h}{(b+a)} = \frac{\sqrt{3} S A_c a^2 \tan\beta}{2[1-(\frac{a}{b})^{2/n_c}]^{n_c}} \left\{ \frac{2[P(\frac{b}{a}-1)-\frac{\gamma}{a}]}{\mu n_c} \right\}^{n_c} \tag{A1-5}$$

$$a=bf \qquad 0<f<1 \tag{A1-6}$$

Combining Eqn. (A4-5) & (A4-6)

$$\frac{b^2 fhdf}{(b+bf)} = \frac{\sqrt{3}SA_c b^2 f^2 \tan\beta}{2[1-(\frac{bf}{b})^{2/n_c}]^{n_c}} \{\frac{2[P(\frac{b}{bf}-1)-\frac{\gamma}{bf}]}{\mu n_c}\}^{n_c} dt$$

$$=> \frac{bfhdf}{(1+f)} = \frac{\sqrt{3}SA_c b^2 f^2 \tan\beta}{2[1-(f)^{2/n_c}]^{n_c}} \{\frac{2[P(\frac{1}{f}-1)-\frac{\gamma}{bf}]}{\mu n_c}\}^{n_c} dt$$

$$=> dt = \frac{2h[1-(f)^{2/n_c}]^{n_c}}{\sqrt{3}A_c bf(1+f)\tan\beta\{\frac{2[P(\frac{1}{f}-1)-\frac{\gamma}{bf}]}{\mu n_c}\}^{n_c}} df$$

(A1-7)

Now,

$$A_c = \frac{A_c{}^{/} b_v \mu}{kT} \exp(-\frac{Q_v}{RT})$$

(A1-8)

Combining Eqn. (A1-7) & (A1-8)

$$dt = \frac{2h[1-(f)^{2/n_c}]^{n_c} \exp(\frac{Q_v}{RT})}{\sqrt{3}\frac{A_c{}^{/} b_v \mu}{kT} bf(1+f)\tan\beta\{\frac{2[P(\frac{1}{f}-1)-\frac{\gamma}{bf}]}{\mu n_c}\}^{n_c}} df$$

$$= \frac{A\frac{h}{b}[1-(f)^{2/n_c}]^{n_c}\exp(\frac{B}{T})}{f(1+f)\{P(\frac{1}{f}-1)-\frac{C}{f}\}^{n_c}}df$$

where A, B and C are model constants

(A: $\frac{2(\mu n_c)^{n_c}}{\sqrt{3}\frac{A_c{}^{l}b_v\mu}{k}\tan\beta}$, B: $\frac{Q_v}{R}$, C: $\frac{\gamma}{b}$)

$$=> dt = A\frac{h}{b}T[1-n_c(f)^{2/n_c}]\exp(\frac{B}{T})(1-f)[n_c(P-C)+Pf]df$$

Integrating both sides-

$$\int_{t_0}^{t}dt = \int_{f_0}^{x}A\frac{h}{b}T[1-n_c(f)^{2/n_c}]\exp(\frac{B}{T})(1-f)[n_c(P-C)+Pf]df$$

$$=> t = t_o + \frac{1}{6}A\frac{h}{b}Txe^{B/T}(6n^2x(t)^{\frac{2}{n}}(-\frac{x(t)(Cn-nP+P)}{2(n+1)}+\frac{n(C-P)}{n+2}+\frac{Px(t)^2}{3n+2})+3x(t)(Cn-nP+P)-6n(C-P)-2Px(t)^2)$$
$$-\frac{1}{6}A\frac{h}{b}Tf_oe^{B/T}(6n^2f_o^{\frac{2}{n}}(-\frac{f_o(Cn-nP+P)}{2(n+1)}+\frac{n(C-P)}{n+2}+\frac{Pf_o{}^2}{3n+2})+3f_o(Cn-nP+P)-6n(C-P)-2Pf_o{}^2)$$

(A1-9)

Chapter 4: Gold Bond Strength in Adhesively Bonded Flip-Chip Joints: Modeling and Simulation

In this chapter, a finite element model is developed that captures the bulk deformation creep process that influences significantly the development of bond strength. The inputs to this model are parametrically varied in a systematic way within the design space to obtain the variability expected in the bond strength. A response surface model is constructed from this that can predict bond strength from the given manufacturing conditions. This model then serves as a prediction tool to obtain the optimum interconnect strength that drives the durability of such systems. The original draft of this chapter is a journal paper that will be submitted for peer-review to Journal of Adhesion Science and Technology.

Influence of Fabrication Parameters on Bond Strength in Adhesively Bonded Flip-Chip Interconnects Part II: Modeling and Simulation

K.Sinha, A. Dasgupta
CALCE Electronic Products and Systems Consortium
Mechanical Engineering Department
University of Maryland, College Park, MD, USA

4.1 Abstract

This is Part II of a two-part paper investigating the role of gold-to-gold interfacial metallurgical bonding, on the bond strength of adhesively bonded flip-chip interconnects in microelectronic assemblies. Part I dealt with experimental investigation of the effect of bonding parameters on Au-Au interfacial bond strength. One of the major conclusions in Part I was that interfacial

creep deformation closely correlated with the measured evolution of bond strength over time. This study presents a viscoplastic finite element analysis to capture the physical creep mechanisms that drive the development of this strength, so that the effect of the system architecture and bonding parameters can be effectively quantified. Based on the studies in literature [42, 43], the strength is assumed to depend on the area of the contact "a-spots," which are defined here as the area over which the interfaces come into intimate, atomistically flat contact.

The most important inputs to the finite element model consist of (i) interfacial geometry (with special emphasis on the surface roughness topology); (ii) viscoplastic mechanical properties of gold; and (iii) bonding parameters (force, temperature and time). The viscoplastic constitutive properties for gold are obtained partly from experiments conducted in this study and partly from the existing literature. The model inputs are parametrically varied in a systematic way within the design space, to obtain the variability expected in the bond strength. The simulation results are captured in a response surface model that can predict bond strength for a given set of fabrication conditions. The response surface model thus serves as a prediction tool critical for optimizing the interconnect strength and the durability of adhesively bonded flip chip assemblies .

Keywords: Interconnect, Microelectronics, Flip-Chip, Diffusion, Indentation, Modeling

4.2 Introduction and Problem Statement

In the conversion towards Pb-free electronics, there has been increasing interest in conductive adhesive interconnects, as they combine Pb-free materials with an attractive, low temperature,

processing. One such promising packaging concept is direct bonding of flip-chip dies onto printed wiring boards (PWBs), with adhesive bonds between a gold-bumped flip-chip IC and matching gold-plated copper pads on a substrate. The goal is to achieve very high I/O densities per unit area, that are currently difficult to achieve, but are critical enablers for next-generation flexible electronic system. The fabrication process relies on adhesive joining methods and requires the simultaneous application of adhesive, pressure, temperature, and time to form the interconnection. As discussed in Part I of this two-part paper, the reliability of this interconnection under cyclic thermal excursions is traditionally believed to be governed by stress relaxation mechanisms in the adhesive. However, experiments reported in the literature [38] and also reported in Part I of this paper [1] for flip-chip interconnects with gold metallization [1], suggest that under typical bonding conditions, a metallurgical bond may form between the mating gold surfaces, due to “cold-welding.” Results in Part I specifically found that time-dependent creep deformation at the interface has a close correlation to the growth of bond strength with time. A computational model that can capture this driving mechanism will provide a valuable prediction method for the bond strength. This will enable significant cost-effective improvements in the design and manufacture of reliable flip-chip packaging technologies.

Section 4.3 of this paper summarizes the current literature on the different interconnect failure mechanisms and contact models in solid-state bonding. Section 4.4 explains the overall approach of this study. Section 4.5 presents the material properties used in the subsequent FEA models, and the experimental procedure for obtaining them. Section 4.6 illustrates the details of the time-independent FEA for a multi-asperity model while Section 4.7 shows the details of a time-dependent FEA for a single asperity model. Finally in Section 4.8 a response surface model is

developed from the FEA results and used to construct a bond strength contour plot with respect to bond force and bond temperature.

4.3 Literature Review

Flip chips became really popular around 1999 [2]. Much work has been done since then to quantify the reliability and durability, usually for specific packages. In cyclic thermal loading studies, these works have mostly focused on cycles to failure, contact resistance, and effects of different bonding forces and bonding temperatures. The concept of cold welding has been around since the 1940s. Studies have mentioned the possibilities of its inclusion into electronics packaging studies [2 and 3], but it has yet to become commonly considered. The literature on modeling of adhesively bonded interconnect failure mechanisms, is reviewed here.

4.3.1 Adhesively Bonded Interconnect Failure Mechanisms

Currently, the majority of papers on adhesively bonded flip chips center around a “top-down” approach. Simulation techniques have been used in conjunction with experimental results in an attempt to fully characterize adhesively bonded flip-chips [11][16]. Some authors have a relationship in their models, between interconnect resistance and compressive force [7] [18][11][17]. Chan, et al. [19] and Li [22] worked on relating bonding pressure and bonding temperature to the reliability of adhesively bonded flip chips. Chan, et al. based their conclusions of proper bonding pressure on proper flip-chip interconnect particle deformation. They also reported that the optimal bonding temperature for these interconnects was 200°C. Bonding temperatures in excess of 200°C resulted in higher interconnect resistance. Fu, et al. [20] agreed with Chan’s work, stating particle deformation as an important factor, and added that particle location in the interface is also important. The resistance of an interconnect was found to

increase with the distance of the particles from the pad center. The work of Chan, et al. [22], and Yeo, et al. [21] confirmed the dependence of resistance on temperature, but Yeo conceded that more work was needed to fully understand the failure mechanisms. Haase [38] found that the contact resistance in his Au-Au interconnect did not degrade through 1000 cycles, but Li, et al.'s Au-Ni system [12] did. Wu, et al. looked into the impact of bump height on interconnect reliability, concluding that higher bumps resulted in higher ACF stress [22]. Haase suggested the possibility of metallurgical bonding in Au-Au metallizations, as the dominant contributor to the interconnect bond strength and how the failure mechanisms might change because of that. Part I of this sequence presents similar evidence, and reports correlations between viscoplastic growth of the contact area and the bonding strength. Additionally, the growth rate of the contact area was correlated to the surface topology and to the bonding parameters. However, there has been no detailed modeling in the flip-chip literature, to address these issues.

There has been significant modeling effort in other research groups (other than in electronic packaging), to correlate the surface topology to the contact area that dictates the metallurgical strength developed at the interface. In the following section, we review the literature on interfacial contact growth and the role of the surface topology on that process.

4.3.2 Interfacial Contact Models

Surface roughness and asperity behavior are critical factors that affect interfacial contact behavior at scales ranging from the nanometer to the micrometer in microelectromechanical, electronic, and photonic devices. In Part I [1], we reported the complex surface topology in the Au-Au flip-chip interconnect system and the plastic deformations experienced by these asperities during the bonding process. Various analytical and numerical methods have been employed to study the contact physics of ideally smooth surfaces [23]. Hertzian contact theory was one of the

first methods to calculate the contact area between two interacting bodies [24]. The model assumed completely elastic contact and neglected surface roughness effects. Despite neglecting the importance of surface area, Hertzian contact is still used because of its simplicity. Holm followed with an ‘elastic - perfectly plastic’ model without strain hardening where stresses at the local contact sites may be much higher than the overall stress, allowing for plastic deformation [25]. Holm’s approach resolves contact area through the use of material hardness and normal load at the contacts. Contact geometry does not play a part in the contact area calculation. The Holm theory is widely accepted, but like Hertzian contact, it does not take full account of the surface topography. Greenwood and Williamson’s (GW) 1966 theory on contact proposed a statistically-based asperity contact [26] model. This work assumed that all contact asperities were spherical with the same radius of curvature, there was no interaction between asperities, and the heights of the asperities were normally distributed. Contact area and the supported load are computed by knowing the material properties, height distribution, and size of surface asperities. While the Hertz model and GW model cover elastic and plastic contact modeling, there are instances where some contact area is plastically deformed but is surrounded by elastically deformed material. In these cases, the Chang, Etison, and Bogy (CEB) model may be used [27]. The CEB model was applied to multi-asperity rough surface modeling by Majumder et al [28]. Although the Hertzian, GW, and CEB models have provided the basis for contact modeling for the past twenty years, the actual topography of the contact surface can often be much more complex than the idealized geometries assumed in these papers. In cases where a large contact force is applied, allowing a large number of asperities to come into contact, the GW model is still valid. At lower contact loads, fewer asperities are forced into contact, and the good correlation between the mathematical distribution functions and the actual surface topography

diverges. In the case of low force applications, like in flip-chip interconnect, an alternative surface area calculation is needed.

The most feasible approach for providing the correct topography for contact modeling is through direct acquisition of three-dimensional surface data from surface microscopy. The topographical data can be provided through stylus profilometry, optical profilometry, or atomic force microscopy (AFM). Each provides the surface height data required to compute the parameters needed for surface modeling or to directly compute the surface area. Dickrell et al. [29] used measured device surface topography to directly calculate the interfacial contact area [26]. Rezvanian et al. used AFM roughness data from a wiSpry RF MEMS switch to build an accurate surface representation for contact area modeling through fractal geometry [29]. The random and multiscale nature of the surface roughness is often described by fractal geometry [39, 40]. Following the asperity-based model of Greenwood and Williamson, the asperities are dealt with individually; however, the deformation behavior of a contact asperity is influenced by other contact asperities, in that the share of the total applied load for each individual contact asperity will be determined by the set of all asperities that are in contact. Rezvanian et al.'s model [29] predicted thermomechanical asperity deformations of contacting surfaces as a function of time. Regardless of the contact model used, the end result is the same and that is to determine the real instantaneous contact area. The real contact area is an integral part of the models used to calculate constriction resistance for micro-contacts. Validated modeling methods can provide designers with insights on the evolution and inter-relationships of of the contact resistance, surface roughness of the contact surfaces, and contact pressure.

With a firm understanding of contact physics in hand, guidelines can be formulated and incorporated in the design and fabrication process to effectively size critical components and

forces to provide stable contact resistance for significantly improved device durability and performance. In this paper we present numerical modeling and simulation to capture the complex inter-relationships between these parameters and to quantify the viscoplastic growth rate of the contact area. The models are compared to the measured evolution of bond strength, reported earlier in Part I [1] of this sequence. It's assumed here based on [42, 43] in this study that the rate governing mechanism for interface bonding is the rate of growth of the contact area. Contact area is defined here as the area over which the interfaces come into intimate, atomistically flat contact.

4.4 Approach

The flowchart in Fig. 4-1 illustrates the modeling steps to investigate the evolution of the contact surface area as a function of contact surface topology, material properties and bonding parameters.. In Part I of this sequence, pull tests were conducted to quantify the strength of the bond as a function of bonding parameters (force, temperature and time). Further, the surface topology of the gold bumps was carefully characterized for use in the modeling effort below. In this second part of this two-part sequence, Au material properties are measured from nanoindentation tests and combined with the data from Part I, to develop a viscoplastic, large-deformation finite element model with nonlinear contact surfaces. This model is used to explore the bonding mechanisms and to examine the sensitivity of the predicted contact area to the different architectural variables and to the bonding parameters.

Finally a fractional factorial parametric study (based on design of experiments) is conducted with this computational model, to understand the effect of the various parameters. The

results are used to generate a response surface model that can be used to optimize the design conditions to obtain the appropriate contact area (and hence, the appropriate bond strength).

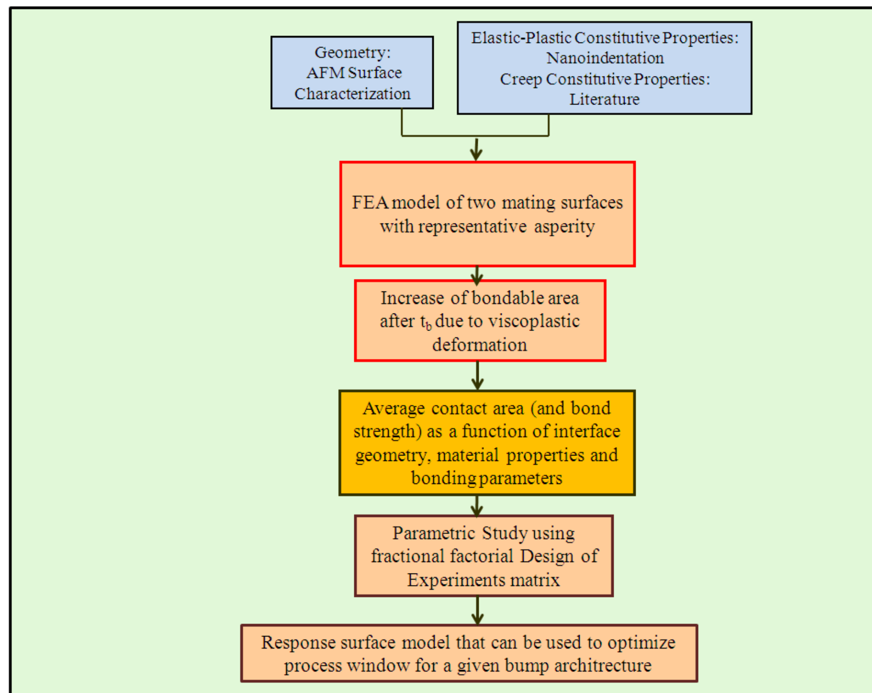

Figure 4-1: Investigation Flowchart

4.5 Experimental Characterization of Gold Properties

The FEA analysis requires elastic-plastic-creep material properties of gold. The accuracy of prediction of the model is heavily dependent on the properties that are used as inputs. The creep properties were obtained from the literature as discussed below, but the elastic-plastic properties were obtained using nanoindentation experiments [30, 31] with a 300nm Berkovich tip..

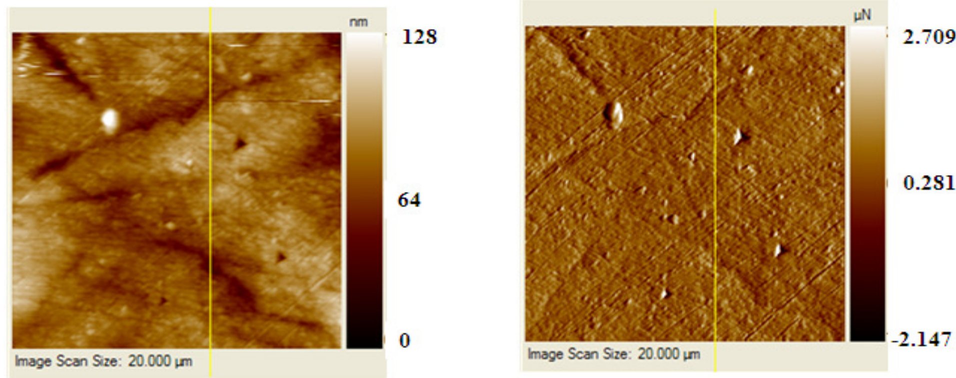

Figure 4-2: Cross-Sectioned Au Bumps (A) Topography, (B) Derivative of Topography

Fig. 4-2 shows sample polished gold bump surface that was used as a sample for the indentation test. Regions with very low roughness heights (<10nm) were chosen (red plus sign in Fig. 4-3), as shown with red cross-hairs in Fig. 4-3, to minimize the effect of roughness on the extracted material properties.

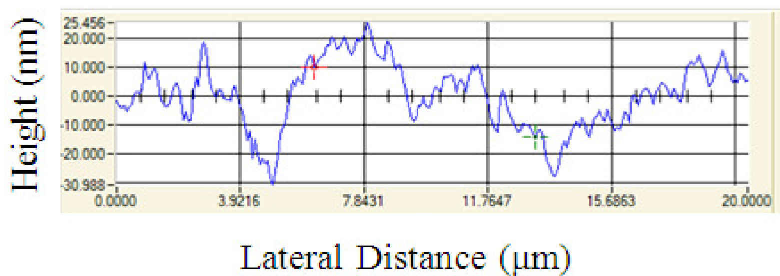

Figure 4-3: Roughness along x-x' Cross-Section (in Fig. 4-2)

An indent array of 13 points with depths ranging from 50 to 300nm was placed on the surface of the bump. A sample loading profile and subsequent load-displacement curve are shown in Fig. 4-3 (a, b). The load-displacement curves were further post-processed to obtain the elastic-plastic behavior of gold. Fig. 4-3 (c) shows both modulus and hardness as a function of indentation depth. The mean modulus value is 93 GPa and mean hardness is 1.4 GPa, with low standard deviation values.

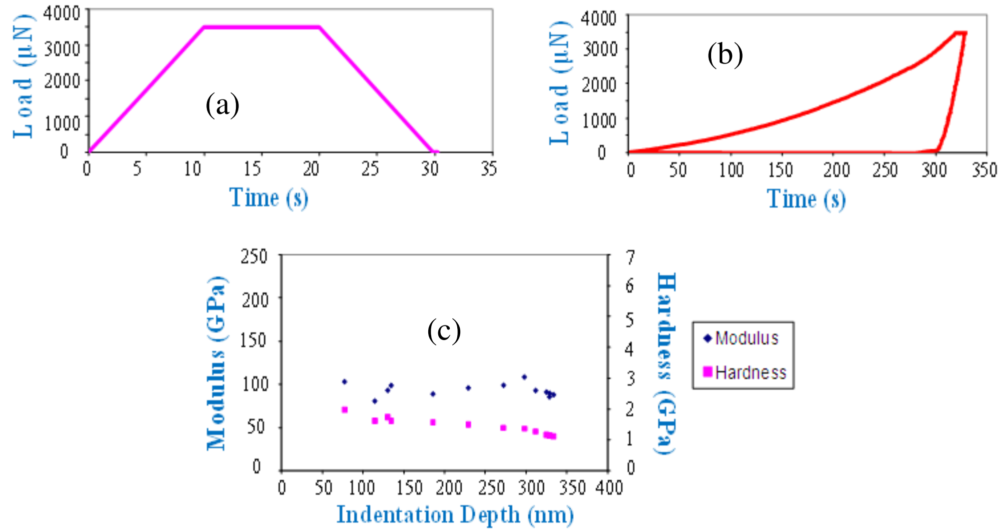

Figure 4-3: (a) Load vs Time (b) Load vs Indentation Depth (c) Variation of Elastic Modulus & Hardness on Indentation Depths

The post-yield stress-strain behavior is extracted from the measured load-displacement curves with the help of a theoretical framework developed by Suresh et al. for instrumented sharp indentation [22-25]. With this method, properties such as Young's modulus, compressive yield strength, strain hardening exponent, strength at a plastic strain of 0.29 and hardness can be determined from the Force-Displacement curves. The method circumvents, by design, the need for visual observations of the contact area and incorporates into the analysis the effects of pile-up and sink-in. The resulting stress-strain curves are shown in Fig. 4-4. 4 indentation results were used to extract the post-yield stress-strain behavior. The mean stress-strain (indicated by blue curve) curve obtained here is used for the FEA analysis

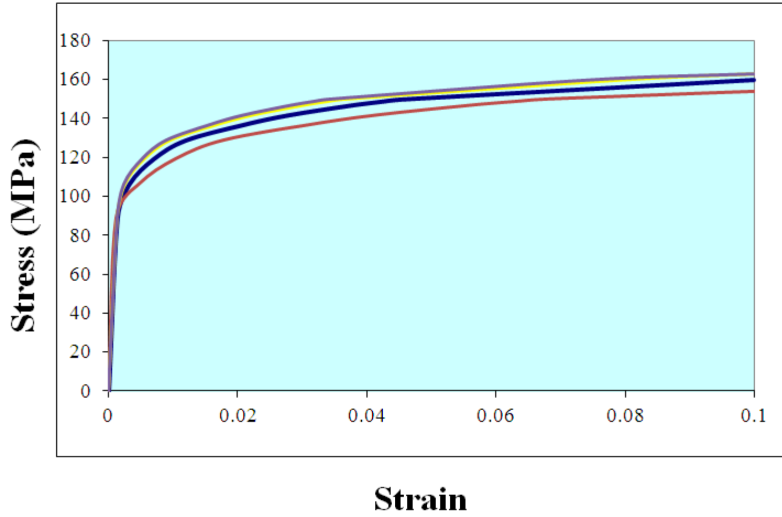

Figure 4-4: Stress-Strain Behavior of Gold

The time dependent normal finite deformations of contact asperities can be represented by a power law constitutive relation as in Eqn. (4-1) where $\dot{\varepsilon}_{cr}$ is the strain rate, A_c is a parameter relating to the material properties and the creep mechanism, σ is the stress, Q_c is the activation energy for creep, T is the absolute temperature and k is the Boltzmann constant (k = 1.38 x 10^{-23} J/K). [41]

$$\dot{\varepsilon}_{cr} = A_c \sigma^p \exp(-\frac{Q_c}{kT})$$

(4-1)

Gold has the following properties obtained from the literature [36, 37]-

Parameters	Values
Power Exponent, p	7
Coefficient, A	1.9 x 10^{-15}
Activation Energy, Qc (Joule)	3 x 10^{-21}

Table 4-1: Power-law Creep Constants for Gold

4.6 Time-Independent Finite Element Model of Au-Au Bonding

The bonding process is modeled as a two-step process. The first step consists of elastic-plastic deformation at the contacting asperities due to the action of the bonding force. This plastic contact area depends on plastic properties of Au and is the initial condition for subsequent viscoplastic growth of the contact area. This plastic deformation is believed to be the reason for atomistically flat 'a-spots' [1] at the interface. An elastic-plastic 2D finite element model is used to capture this plastic "flattening" of mating asperities at the rough Au surfaces, when the bonding pressure is applied. A representative cross-section of the measured surface through AFM measurements [1] was chosen and a FEA model was developed with matching asperity dimensions.

A sample 2D cross-section profile of the actual gold-bump surface is shown in Fig. 4-5. Two identical rough surfaces were mated with a fixed displacement and the response parameter (total contact area or 'a' spots at the interface) was calculated. The boundary conditions to this model are that the bottom surface is fixed in y-direction; the left hand edge is fixed in x-direction while the right hand edge has a coupled displacement in x-direction. A displacement boundary condition is applied from the top. 8 noded plane elements were used in the mesh with total of 10,761 nodes. The type of surface in contact is parametrically varied by offsetting the top surface stepwise by 0.5 microns. Below are the various configurations from which the Force vs Displacement and Force vs Contact Area curves are derived.

The top surface was then parametrically offset to bring different asperities into contact and observe how the response parameter (contact area) changes with misalignment. Fig. 4-6 shows the deformation contour plot of a sample offset configuration where the overlap length is the region where the two surfaces are directly facing each other.

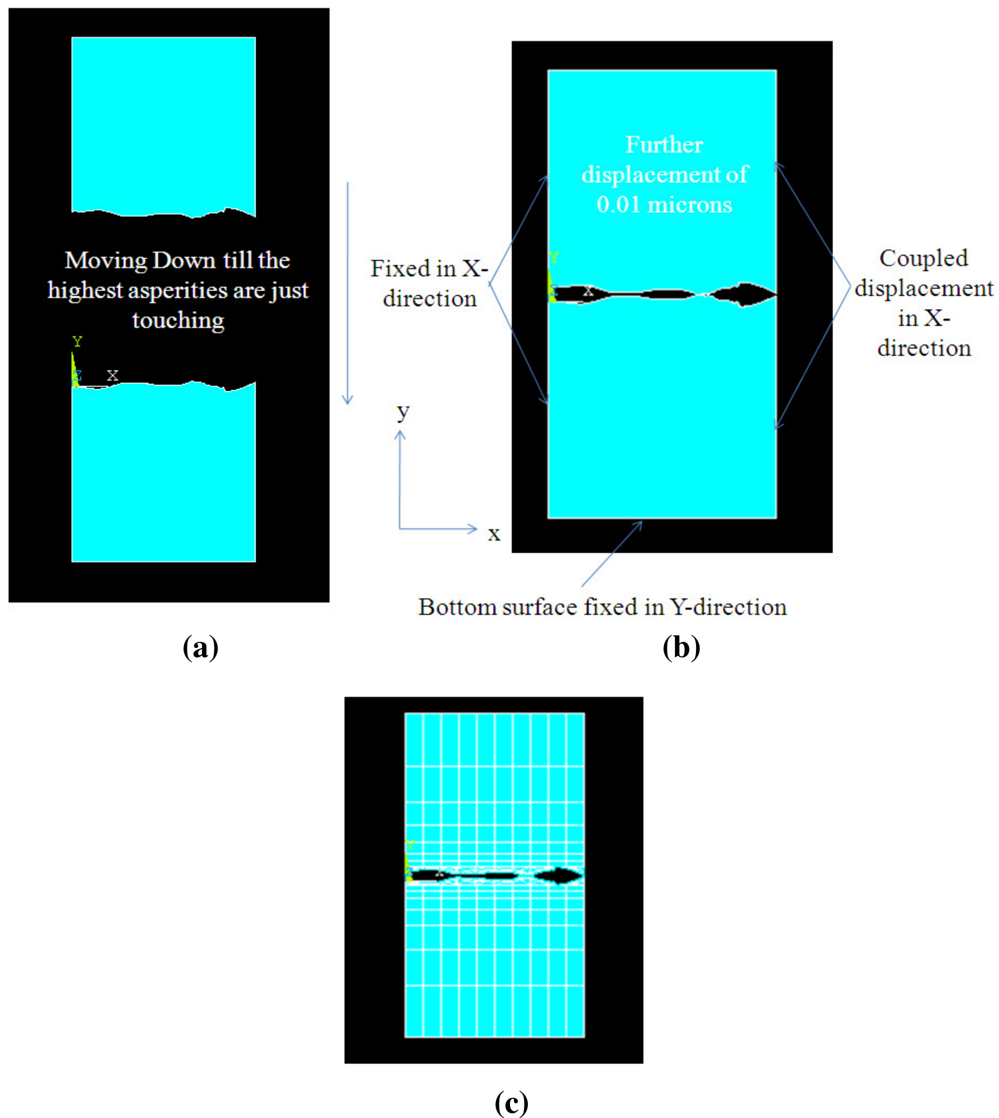

Figure 4-5: Multi-Asperity Model (a) Geometry (b) Boundary Conditions (c) Meshing

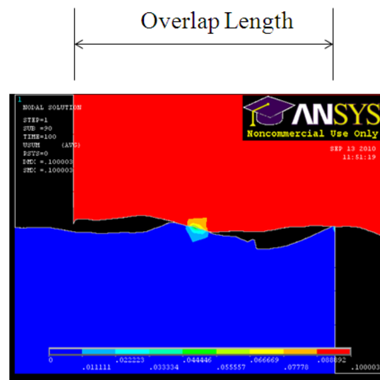

Figure 4-6: Displacement Contour Plot at a Selected Offset Configuration

The Force vs Displacement curve showed stochastic variation with the lateral shift and in most cases it resulted in stiffer curves than the one without offset.

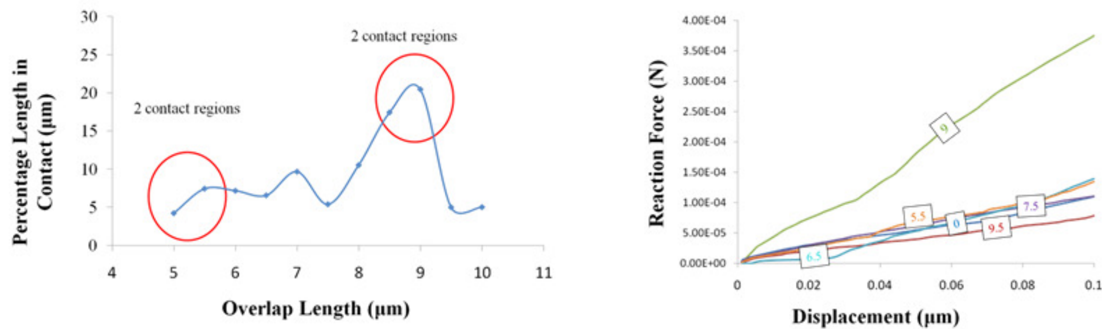

Figure 4-7: Offset Modeling Results: (a) Percentage Contact Length vs Overlap Length (b) Force vs Displacement

However, interestingly the Force vs Contact Area response was not very sensitive to changes in the magnitude of surface roughness. So, the instantaneously bonded contact area is not expected to vary much with the geometry of the asperities that come into contact. This may not hold true if the roughness is drastically changed but the statistical variation of roughness from bump to bump for unmated surfaces stays within the same order of magnitude [1]. The details of the roughness geometries and meshing are in Appendix 7 of [44]. The Force vs Contact Area response however was quite sensitive to the material properties. Fig. 4-9 shows how changing the properties affect the response curves.

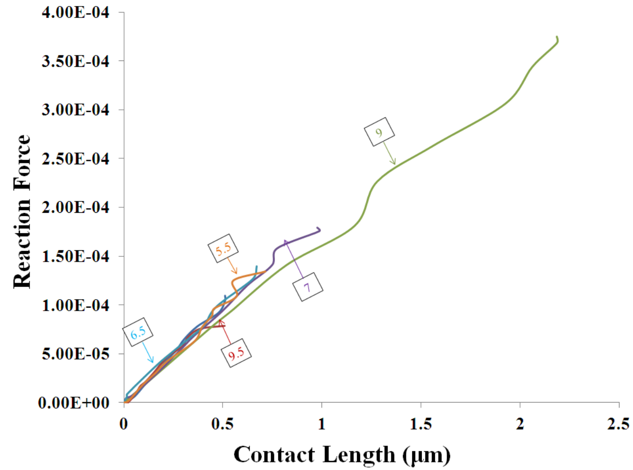

Figure 4-8: Force vs Contact Length for Different Configurations

The plastic deformation values obtained here at the experimental bonding forces were compared to the f_o values obtained from the experimental results by fitting the Derby-Wallach model. Table 4-2 compares the two results which show that the FEA results fit well with the empirical model's output.

Bonding Force (Kgf)	f_o (Empirical Model [1])	f_o (FEA)
8	0.071	0.076
6	0.042	0.045
4	0.03	0.033

Table 4-2: Comparison of plastic deformation (Empirical Model vs FEA)

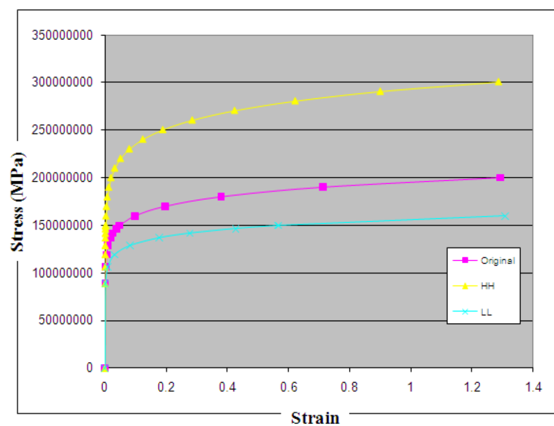

$\varepsilon = (\sigma/E)+(\sigma/a)^{(1/b)}$

HH-> a increased by 50%
b increased by 10%

LL-> a decreased by 20%
b decreased by 10%

(a)

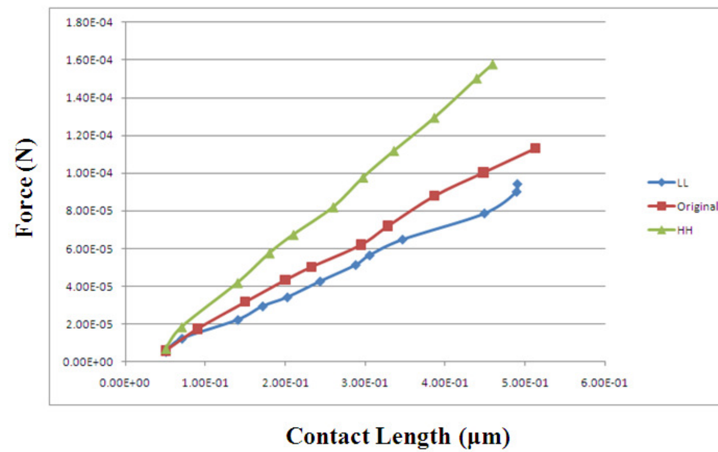

(b)

Figure 4-9: Material Property Sensitivity (a) Parametric Variation of Gold Property (b) Force vs Contact Area curves

4.7 Time-Dependent Finite Element Model of Au-Au Bonding

As observed from pull test experiments performed in [1], the bond strength was found to increase with bonding time and the viscoplastic increase in the contact area (based on a simple analytic power-law bulk creep deformation) was found to correlate well with the measured strength data. The FEA modeling effort is therefore extended to include this time-dependent behavior. The multi-asperity model has been simplified to an axisymmetric single asperity model to investigate this behavior. The RMS height (0.22 microns) and average wavelength (4.5 microns) observed from the AFM scans in [1] are used for this sinusoidal asperity. Assuming it mates with another identical asperity, the target surface was represented with a rigid flat surface.

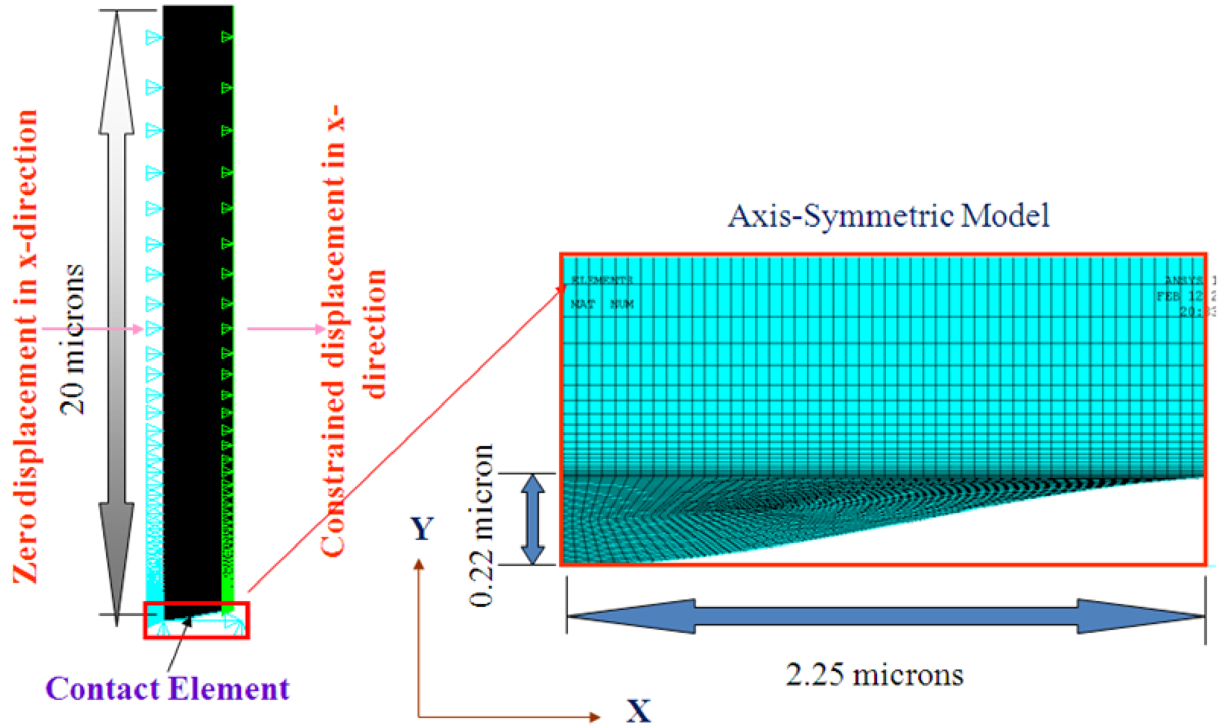

Figure 4-10: Representative “a-spot” Finite Element Model

The schematic of the FEA approach is shown in Fig. 4-11. The finite element model is compressed from the top with a scaled constant force that is scaled from the total bonding force on the entire die. In order to obtain the scaled force the total force is divided by an estimate of the number of asperities. The number of asperities is calculated by dividing the total surface area (0.24 mm^2) (after taking into account the misalignment and bump positions) with the area of each asperity (1.59E-5 mm^2) and we get a total of approximately 15094 asperities. This of course assumes a uniform isotropic distribution of self-similar asperities, to idealize the surface topology, and that the force is uniformly distributed across all asperities. This approximation is needed to simplify the computational model. The constant force is then applied for 100 seconds, allowing the asperity to deform with time. The contact area at each time step is extracted from the FEA. The normalized contact area history is then compared to the normalized bond strength history from the experimental results, as shown in Fig. 4-12. For this comparison, the two results

are normalized to the same scale (0 to 1) with contact area being proportionally transformed to bond strength. The two plots show very similar behavior, as seen in the plot (Fig. 4-12).

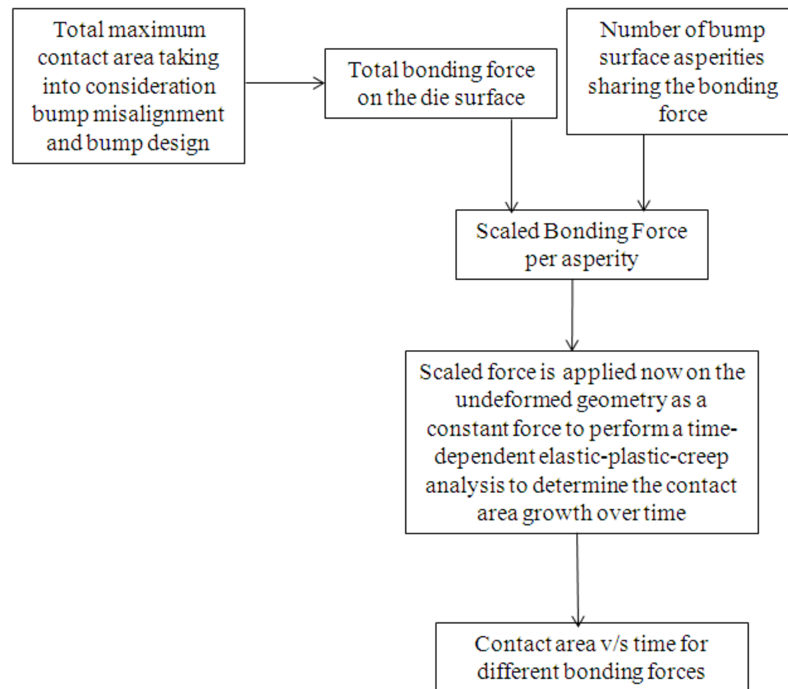

Figure 4-11: Schematic of FEA approach

This process is then repeated for all 3 bonding forces (4 Kgf, 6 Kgf and 8 Kgf) as per the pull test experiments in [1]. The initial time lag period (t_o) reported from experiments in [1] varies with bonding force, with lower bonding forces having considerable t_o values [1]. So, the curve generated from the FEA model is shifted by this t_o amount in the horizontal axis and then compared with the experimental results and with the predictions from the Derby-Wallach model [1].

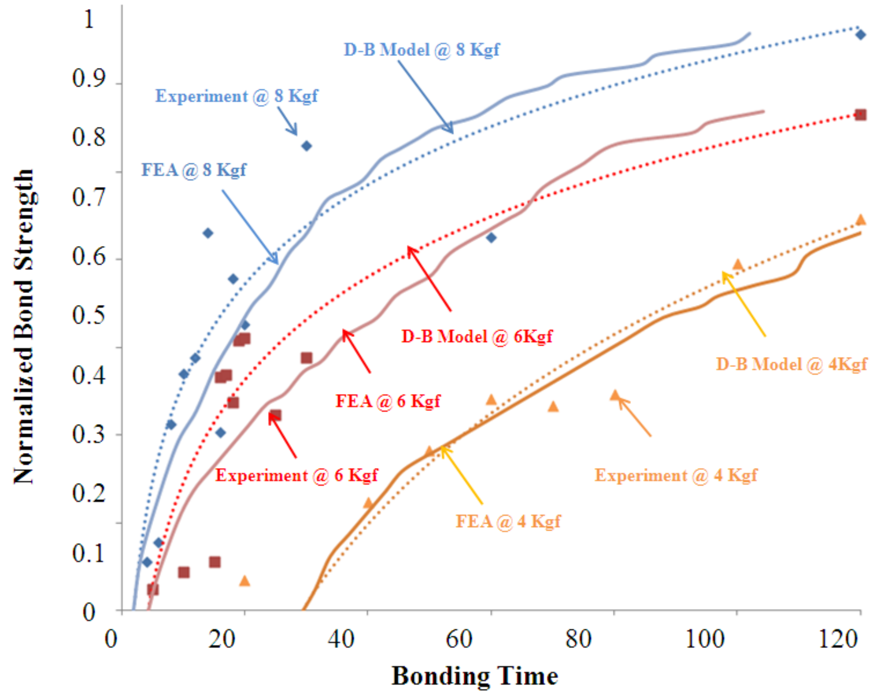

Figure 4-12: Comparison of FEA Results (solid lines) with Experiment (data points) and with the Empirical Derby-Wallach Model (dashed lines)

Thus the FEA model is found to adequately represent the bond growth history, as obtained from the experiments and the empirically calibrated Derby Wallach model. The instantaneous area fraction of contact area due to plastic deformations predicted by Derby Wallach model matches well too with the FEA results. Hence the FEA can be used for reasonable assessment of the sensitivity to the input bonding parameters. The next section attempts to use this FEA model to explore the design space and to generate a response surface model.

4.8 Response Surface Model

First the important parameters are identified that can vary depending on the manufacturing process, surface finish or constitutive behavior. Eight of these are captured in the response surface model, because of their criticality in this study. The parameters include two bonding

parameters (force and temperature), roughness parameters (mean, rms, skewness and kurtosis) and material parameters (plasticity and creep exponents). The other bonding parameter which is bonding time is fixed at t_0+100 seconds (where t_0 is the experimentally observed incubation period before the bond strength starts to grow [1]) for this particular response surface model. Other variables like surface oxygen content are beyond the scope of this study and hence not included. Next, the 2 minimum and maximum possible values are identified. Thus we obtain 8 parameters with 2 levels (Table 4-3) each and we can have many combinations taking the extremes of each parameter. The Level-1 for plastic properties denotes 10% increase in Ramberg-Osgood exponents and Level-2 denotes 10% decrease in the exponents compared to the average stress-strain behavior obtained in section 4.5. The levels for the rest of the parameters are chosen either by measurements or based on the expected range.

Parameters	Sign	Levels	Level-1	Level-2
Force (F)	A	2	3 Kgf	9 Kgf
Temperature (T)	B	2	200°C	300°C
Roughness Mean Height (R_m)	C	2	0 nm	192 nm
Roughness RMS Height (R_{rms})	D	2	116 nm	430 nm
Skewness (R_q)	E	2	-0.46	0.8
Kurtosis (R_k)	F	2	2	4.2
Plasticity Exponent (P)	G	2	LL	HH
Creep Exponent (n)	H	2	5	7

Table 4-3: Parameter Levels

To economize the number of FEA runs, a standard Taguchi fractional factorial approach was taken to develop a design of experiment (Table 4-4) matrix. These parameters are then input in the FEA model reported in the previous section, to obtain the contact area vs bonding time behavior. The roughness profiles involved in this parametric study is documented in Appendix 6 of [44].

Variable / Run #	A	B	C	D	E	F	G	H
1	1	1	1	1	1	1	1	1
2	1	1	1	1	1	2	2	2
3	1	1	2	2	2	1	1	1
4	1	2	1	2	2	1	2	2
5	1	2	2	1	2	2	1	2
6	1	2	2	1	2	2	2	2
7	1	2	2	2	2	1	2	2
8	2	1	2	1	2	2	2	1
9	2	1	1	2	2	2	1	2
10	2	2	2	1	1	1	1	2
11	2	2	1	2	1	2	1	1
12	2	2	1	1	2	1	2	1

Table 4-4: Design of Experiment

Fig. 4-13 shows the output of all 12 runs having various kinds of curves as output. The final contact area at $t=t_0 + 100s$ (where t_0 is the empirically observed initial incubation time before bond strength starts to grow [1]) varied to quite some extent depending on the combination.

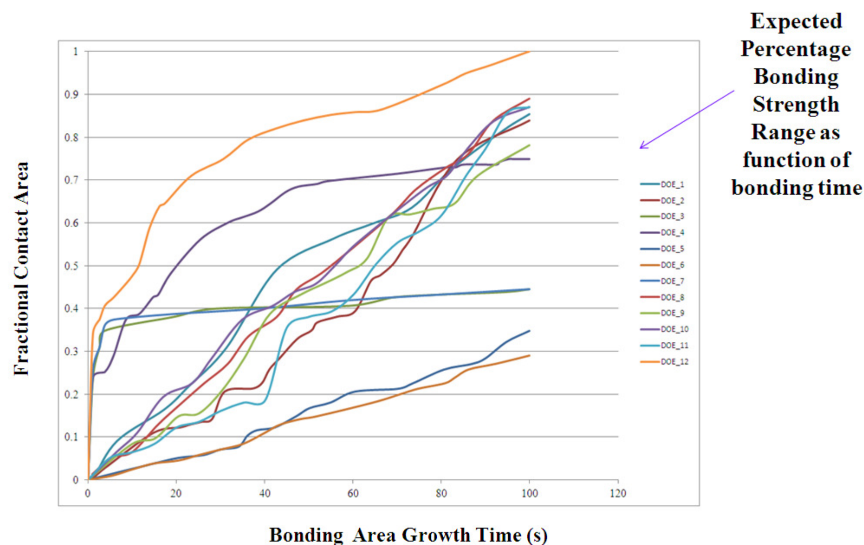

Figure 4-13: FEA Results from DOE

The outputs from these FEA runs were next used to generate a response surface model. The response parameter here is the contact area at the end of 100 seconds of bonding (RS). The model consists of constant and linear terms for all the parameters with different coefficients and selected interaction terms that were found to have a strong influence on the response parameter. The model constants are obtained by a least square fit to the FEA output, using commercial software. The maximum value of each variable was input as +1 and minimum value was input as -1. Any value in between can be normalized by scaling it in that range. The detailed structure of the model and the fitted constants are as follows-

$$RS = a_1 + a_2 *F + a_3*T + a_4*R_m + a_5*R_{rms} + a_6 *R_q + a_7 *R_k + a_8 *Pl + a_9*n + a_{10}*F*T + a_{11}*F*R_m + a_{12}*T*R_{rms} \quad (4-2)$$

Coefficients	Values
a_1	0.6
a_2	0.24
a_3	0.13
a_4	-0.022
a_5	0.08
a_6	0.11
a_7	-0.18
a_8	-0.03
a_9	0.06
a_{10}	0.05
a_{11}	0.14
a_{12}	0.015

Table 4-5: Response Surface Model Coefficient Values

As evident, the bonding force has the highest influence on the contact area. The ranking of the other parameters and interaction terms are in Table 4-6. An F-test was performed to get the

relative significance of each of these variables.

Parameters	Ranking	Sum of Squares	F-Ratio
Force	1	0.19	4.89
Force*R_m	2	0.17	4.16
Temperature	3	0.16	3.85
Kurtosis	4	0.12	2.54
Skewness	5	0.08	1.53
Roughness Mean	6	0.04	0.76
Creep Exponent	7	0.02	0.34
Force*Temp	8	0.01	0.26
Plasticity	9	0.002	0.05
Roughness RMS	10	0.002	0.03
Temp*R_{rms}	11	0.001	0.015

Table 4-6: Ranking of the Variables and Interaction Terms

This model is then used to predict the bond strength for all combinations of bonding force and bonding temperature at the average roughness values and actual material properties. Again, based on the previous assumptions, the predicted bond strength has been correlated to the predicted contact area.

Fig. 4-14 is a contour plot from which it is possible to choose a suitable combination of bond force and temperature for desired bond strength. The scope and limitations of the manufacturing process will enable the decision of which combination fits best here.

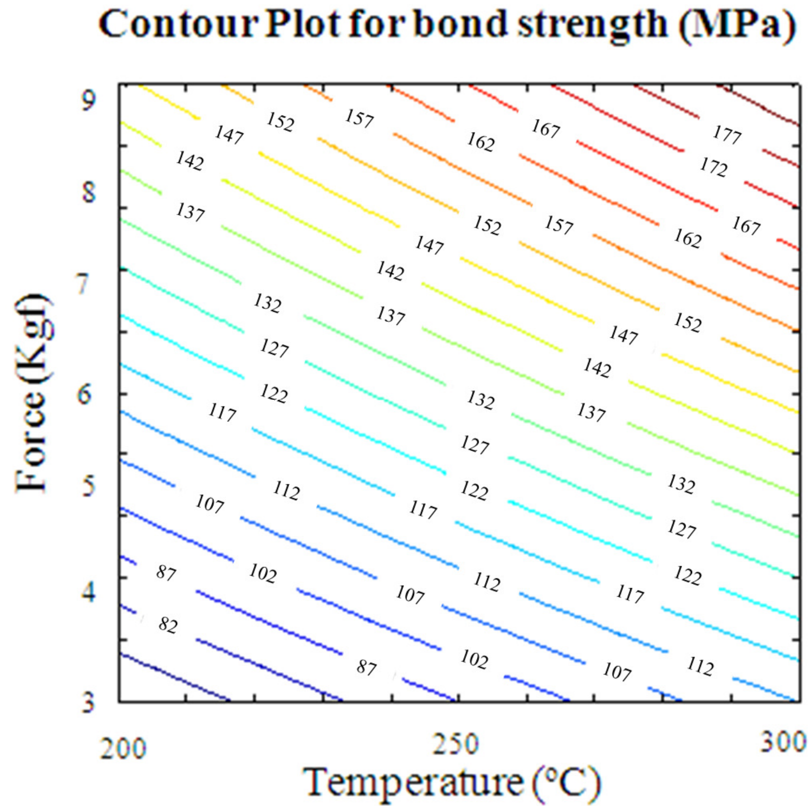

Figure 4-14: Contour Plot of bond strength from Response Surface Model Predictions

4.9 Summary and Conclusion

In this second part of the two-part sequence, the contact area (and hence bonding strength) trends of Au/Au bonded flip chips with respect to different bonding parameters (force, temperature and time) was comprehensively captured in a viscoplastic finite element model. The model takes roughness parameters of the surface profile and elastic-plastic-creep material properties as inputs. The bonding parameters have been varied systematically so that the FEA model can be matched with the experimental measurements in Part 1 of this sequence [1]. The time independent analysis shows the plastic deformation predicted by the FEA model is close to the empirical models prediction in [1]. The time dependent model then shows close results both to

the experiment and Derby-Wallach empirical model validating it effectively. Next a systematic fractional factorial parametric study is conducted with this FEA model by varying the different parameters within their realistic ranges. These results provide a response surface model that can be used as a prediction tool for the bond strength. Bonding force has the strongest influence here among all the parameters followed by the other terms. This model can be useful for strength prediction and thus process parameter optimization in the manufacturing of such flip-chip joints.

Acknowledgments

The work reported here was sponsored by the members of the Electronic Products and Systems Consortium at the Center for Advanced Life Cycle Engineering at the University of Maryland.

References

1. Sinha, K.; Farley, D.; Kahnert T.; Dasgupta A.; Caers J. F. J. and Zhao X.J., "Dependence of Bond Strength in Adhesively Bonded Flip-Chip Interconnects on Different Parameters: Part 1", Preceding paper in this issue.
2. Ellis, T. W., "The Future of Gold in Electronics," Gold Bulletin. Vol. 37, no. 1-2, pp. 66-71. 2004, DOI: 10.1007/BF03215518.
3. Ferguson G.; Chaudhury, M.; Sigal G. and Whitesides G., "Contact adhesion of thin gold films on elastomeric supports - Cold welding under ambient conditions," Science, Vol. 253, pp. 776-778, 1991, *DOI:* 10.1126/science.253.5021.776.
4. Frisk, L. and Ristolainen, E., "Flip chip attachment on flexible LCP substrate using an ACF," Microelectronics Reliability 45 (2005) 583–588, DOI: http://dx.doi.org/10.1016/j.microrel.2004.10.009.

5. Teh L.K.; Wong C.C.; Mhaisalkar S.; Ong, K., Teo, P.S. and Wong, E.H., "Characterization of Nonconductive Adhesives for Flip-Chip Interconnection," Journal of Electronic Materials, Vol. 33, No. 4, pp. 271-276, 2004, DOI: 10.1007/s11664-004-0132-8.
6. Teo, M.; Mhaisalkar, S. G.; Wong, E. H.; Teo, P.-S.; Wong, C. C.; Ong, K.; Goh C. F. and Teh L. K., "Correlation of Material Properties to Reliability Performance of Anisotropic Conductive Adhesive Flip Chip Packages," IEEE Transactions on Components and Packaging Technologies, Vol. 28, No. 1, March 2005, DOI: 10.1109/TCAPT.2004.843175.
7. Yim M.J.; Hwang J.S.; Kwon W.; Jang K.W. and Paik, K.W., "Highly reliable nonconductive adhesives for flip chip CSP applications," Electronics Packaging Manufacturing, IEEE Transactions on, Vol. 26, No. 2, pp.150–155, April 2003, DOI: 10.1109/TEPM.2003.817715.
8. Yin, C.; Lu, H.; Bailey, C. and Chan, Y-C., "Effects of Solder Reflow on the Reliability of Flip-Chip on Flex Interconnections Using Anisotropic Conductive Adhesives," IEEE Transactions on Electronics Packaging Manufacturing, Vol. 27, No. 4, 2004, DOI: 10.1109/TEPM.2004.843152.
9. Aschenbrenner, R.; Miessner, R. and Reichl, H., "Adhesive flip chip bonding on flexible substrates," The First IEEE International Symposium on Polymeric Electronics Packaging, Oct 1997, DOI: 10.1109/PEP.1997.656478.
10. Chan, Y.C.; Hung, K.C.; Tang, C.W. and Wu, C.M.L., "Degradation Mechanisms of Anisotropic Conductive Adhesive Joints for Flip Chip on Flex Applications," Adhesive Joining and Coating Technology in Electronics Manufacturing, 2000, DOI: 10.1109/ADHES.2000.860588.

11. Chiang, K.N.; Chang, C.W. and Lin, J.D., "Analysis of ACA/ACF package using equivalent spring method," Electronics Packaging Technology Conference, 2000, DOI: 10.1109/EPTC.2000.906358.
12. Li, L. and Fang, T., "Anisotropic Conductive Adhesive Films for Flip Chip on Flex Packages," Adhesive Joining and Coating Technology in Electronics Manufacturing, 2000, Proceedings on 4th International Conference, DOI: 10.1109/ADHES.2000.860586.
13. Ferrando, F.; Zaberli, J.F.; Clot, P. and Chenuz, J.M., "Industrial approach of a Flip-Chip method using the stud-bumps with a non-conductive paste," Adhesive Joining and Coating Technology in Electronics Manufacturing, Proceedings. 4th International Conference on, pp. 205-211, 2000, DOI: 10.1109/ADHES.2000.860600.
14. Pajonk, J., "New flip chip technology utilizing non-conductive adhesive adapted for high volume chip card module production," Electronics Manufacturing Technology Symposium, 2004, DOI: 10.1109/IEMT.2004.1321653.
15. Mercado, L. L.; White, J.; Sarihan V. and Lee, T., "Failure Mechanism Study of Anisotropic Conductive Film (ACF) Packages," IEEE Transactions on Components and Packaging Technologies, Vol. 26, No. 3, September 2003, DOI: 10.1109/TCAPT.2003.817640.
16. Jang, C.; Han, S.; Kim, Y.; Kim, H.; Yoon, S.; Cho, S.; Han, C. and Han, B., "Development of Predictive Modeling Scheme for Flip-chip on Fine Pitch Flex Substrate," EuroSimE 2005, DOI: 10.1109/ESIME.2005.1502868.
17. Kristiansen, H.; Gulliksm, M.; Haugerud, H. and Friberg, R., "Characterization of Electrical Contacts Made By Non-Conductive Adhesive," Adhesive Joining and Coating Technology in Electronics Manufacturing, 1998, DOI: 10.1109/ADHES.1998.742051.

18. Caers, J.; Zhao, X.; Wong E. and S. Mhaisalkar, “Towards a predictive behavior of non-conductive adhesive interconnects in moisture environment,” ECTC 2004, DOI: 10.1109/ECTC.2004.1319322.
19. Chan, Y.C. and Luk, D.Y., “Effects of bonding parameters on the reliability performance of Anisotropic conductive adhesive interconnects for Flipchip-on-flex packages assembly II. Different bonding pressure,” Microelectronics Reliability 42 (2002) 1195–1204, DOI: http://dx.doi.org/10.1016/S0026-2714(02)00089-6.
20. Fu, Y.; Wang, Y.; Wang, X.; Liu, J.; Lai, Z.; Chen, G. and Willander, M., “Experimental and theoretical characterization of electrical contact in anisotropically conductive adhesive,” IEEE Transactions on Advanced Packaging, Vol. 23, No. 1, 2000, DOI: 10.1109/6040.826757.
21. Yeo, A.; Teo, M. and Lee, C., “Thermo- and Hydro-mechanical Modeling of an Adhesive Flip Chip Joint,” Electronics Packaging Technology Conference, 2004, DOI: 10.1109/EPTC.2004.1396583.
22. Wu C.M.L.; Liu, J. and Yeung N.H., “Reliability of ACF in Flip-Chip with Various Bump Height,” Adhesive Joining and Coating Technology in Electronics Manufacturing, 2000, DOI: 10.1109/ADHES.2000.860580.
23. Johnson, K.L., “Contact Mechanics”, Cambridge: Cambridge University Press, 1985.
24. Johnson, K.L., “Contact Mechanics”, Cambridge University Press , London, 1998.
25. Holm, R., “Electric Contacts: Theory and Applications”, Berlin, Germany: Springer, 1969.
26. Dickrell, D.J.; Dugger, M.T.; Hamilton M.A. and Sawyer, W.G., "Direct Contact-Area Computation for MEMS Using Real Topographic Surface Data," J. Microelectromech. Syst., Vol.16, No.5, pp.1263-1268, Oct. 2007, DOI: 10.1109/JMEMS.2007.901120.

27. Chang, W.; Etison, I. and Bogy, D., "An elastic-plastic model for the contact of rough surfaces," ASME J. Tribol., 109, pp. 257-263, 1987, DOI: http://dx.doi.org/10.1115/1.3261348.

28. Majumder, S.; McGruer N.E.; Adams, G.G.; Zavracky, P.M.; Morrison, R.H. and Krim, J., "Study of contacts in an electrostatically actuated microswitch," Sensors and Actuators A, vol.93, no.1, pp. 19-26, 2001, DOI: 10.1109/HOLM.1998.722437.

29. Rezvanian, O.; Zikry, M.A.; Brown, C. and Krim, J., "Surface roughness, asperity contact and gold RF MEMS switch behavior," J. Micromech. Microeng. 17, pp. 2006-2015, 2007, DOI: 10.1088/0960-1317/17/10/012.

30. Choi, Y. and Suresh, S., "Nanoindentation of patterned metal lines on a Si substrate", Scripta Materialia 48, 249, 2003, DOI: http://dx.doi.org/10.1016/S1359-6462(02)00377-9.

31. Shan, Z. and Sitaraman, K., "Elastic-plastic characterization of thin films using nanoindentation techniques", Thin Solid Films *437,* 176, 2003, DOI: http://dx.doi.org/10.1016/S0040-6090(03)00663-1.

32. Giannakopoulos, A. E.; Larsson P.-L. and Vestergaard, R., "Analysis of Vickers indentation", Int. J. Solids and Struct., 31, 2679-2708, 1994, DOI: http://dx.doi.org/10.1016/0020-7683(94)90225-9.

33. Larsson, P.-L.; Giannakopoulos, A. E.; So¨derlund, E.; Rowcliffe, D. J. and Vestergaard, R., "Analysis of Vickers indentation", Int. J. Solids Struct. 33, 221, 1996, DOI: 10.1016/0020-7683(95)00033-7.

34. Giannakopoulos, A. E. and Suresh S., "Determination of elastoplastic properties by instrumented sharp indentation", Scripta Mater. 40, 1191, 1999, DOI**:** 10.1016/S1359-6462(99)00011-1.

35. Suresh, S. and Giannakopoulos, A. E., “A new method for estimating residual stresses by instrumented sharp indentation", Acta Materialia, vol. 46 (16), 1998, pp. 5755-5767, DOI: http://dx.doi.org/10.1016/S1359-6454(98)00226-2.

36. Frost, H.J. and Ashby, M.F., “Deformation Mechanism Maps” Pergamon, Oxford 1982.

37. Brown, C.; Rezvanian, O.; Zikry, M.A. and Krim, J., “Temperature dependence of asperity contact and contact resistance in gold RF MEMS switches”, J. Micromech. Microeng. 19 (2009) 025006 (9pp), DOI: 10.1088/0960-1317/19/2/025006.

38. Haase, J., Iyer, P., Baumgartner, P., Farley, D., Dasgupta, A. and Caers, J., “Mechanics of Adhesively Bonded Flip-Chip-on-Flex Assemblies. Part I: Durability of Anisotropically Conductive Adhesive Interconnect,” Journal of Adhesion Science and Technology Vol 22, pp. 1733–1756, 2008, DOI: 10.1163/156856108X320564.

39. Yan, W. and Komvopoulos, “Contact Analysis of Elastic-Plastic Fractal Surfaces”, Journal of Applied Physics, Vol. 84, No. 7, October 1998

40. Wang, S.; Shen, J. and Chan W.K., “Determination of the Fractal Scaling Parameter from Simulated Fractal-Regular Surface Profiles Based on the Weierstrass-Mandelbrot Function”, Transactions of ASME, Vol. 129, October 2007

41. Weertman, J., “Theory of Steady-State Creep Based on Dislocation Climb”, Journal of Applied Physics, Volume 26, Number 10, October 1955

42. He, J.; Guo, Y. and Lin, Z., " Numerical and experimental analysis of thermosonic bond strength considering interfacial contact phenomena”, Journal of Physics D: Applied Physics, vol. 41, 2008, 165304 (13pp), DOI:10.1088/0022-3727/41/16/165304.

43. Fu, X. and Chung, D.D.L., “Sensitivity of the bond strength to the structure of the interface between reinforcement and cement, and the variability of this structure”, Journal of Cement

and Concrete Research, Volume 28, Issue 6, June 1998, Pages 787-793, DOI: http://dx.doi.org/10.1016/S0008-8846(98)00055-6.

44. Sinha, K., “Mechanics of Non Planar Interfaces in Flip-Chip Interconnects,” PhD Thesis, University of Maryland, College Park, Maryland, 2012

Chapter 5: Solder Interconnects in Adhesively Bonded Flip-Chip Joints: Crack Behavior at Non-Planar Interfaces

In this chapter, the bond strength that solder joints form in flip-chip assemblies have been investigated. A complex global-local finite element modeling approach gives the fracture strength of such joints and its expected variability with respect to various parameters. This study subsequently provides fundamental insights into the influence of the important governing factors on the change of apparent resistance to crack initiation in solder joints under shock and drop loading that are typical in portable electronic products. The contributions from this study go beyond flip-chip joints to other electronic package having similar joint structure. The original draft of this chapter is a journal paper that will be submitted for peer-review to Internal Journal of Fracture.

Effect of Geometric Complexities and Nonlinear Material Properties on Interfacial Crack Behaviour in Electronic Devices

Koustav Sinha, Joe Varghese, Abhijit Dasgupta
University of Maryland, College Park, Maryland, USA, 20742

5.1 Abstract

Interfacial failures are often found in solder joints between electronic components and PWAs, under shock and drop loading. These interfacial fractures are often either between layers of dissimilar intermetallic compounds (IMCs), or between the solder and IMC [1]. Studies have revealed that these interfaces are usually scalloped (wavy and non-planar) and that the waviness

decreases with continued thermal aging, accompanied by a reduction of the apparent resistance to interfacial crack initiation [2, 3]. This study investigates the effects of the interfacial waviness, nonlinear solder material properties, local geometric complexities, and the initial crack length, on the resistance to crack initiation. A detailed multi-scale, global-local, elastic-plastic finite element fracture simulation model is constructed and calibrated against the test data published in the literature [3] for 3 different roughness profiles on a soldered cantilever fracture specimen. The global model of the test specimen [3] analyses the average stresses in the solder and the local finite element model extracts the energy release rate at the tips of cracks of various lengths at the wavy IMC interfaces. The energy release rates are averaged over a periodic length of the wavy interface to obtain effective average values, so that the results can be compared with test results reported by Yao & Shang [3]. The initial crack length and loading rate are parametrically varied for each of the 3 roughness levels in Yao's paper. The analysis is repeated for elastic solder properties, elastic-plastic solder properties and viscoplastic solder properties. The results are compared with those from simple analytic models of a crack at a wavy interface between two semi-infinite elastic solids. These results provide fundamental insights into the influence of all the governing factors on the change of apparent resistance to crack initiation.

5.2 Introduction

Electronic assemblies rely on soldered connections between metallized terminals on components and matching terminals on printed wiring boards (PWBs). These joints are created by forming multiple species of metallurgical intermetallic compounds between the Tin in the solder and the metallization on the pad. As an example, Cu_6Sn_5 and Cu_3Sn intermetallic layers are formed with copper solder pads, while SnCuNi intermetallics are formed with Nickel-plated solder pads. The

interfaces between these intermetallic layers are wavy and scalloped, as are the interfaces with the solder. These (Fig. 5.1) interfaces are sometimes the weakest part of the structure, as the toughness of these brittle materials is low and the stresses can be high due to discontinuity of properties across these interfaces. Failure due to dynamic mechanical stresses, for example because of drop and shock events, are often by interfacial fracture.

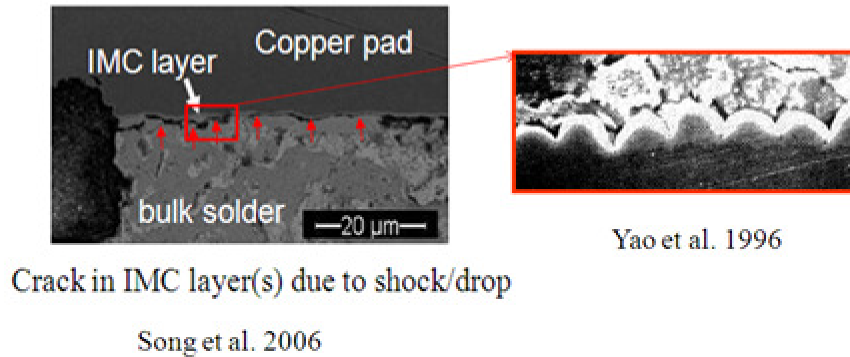

Figure 5.1: Example of Scalloped IMC Layer in a Solder Joint

Accurate predictions of interfacial failure rely heavily on determination of the fracture parameters that adequately characterize the state of stress at the debonded interface of interest, i.e., the stress intensity factors (K_I, K_{II}, K_{III}) and the strain energy release rate (G). The strain energy release rate of the crack depends on the waviness, phase angle of loading, and the properties of the materials that meet at the interface. According to the concept of fracture mechanics, cracks start propagating when the strain energy release rate exceeds a critical threshold value, termed the fracture toughness of the material/interface. However, the crack growth is detectable only when the interface reaches a fatigue threshold, after which it follows a power-law dependence on the stress intensity factors.

Published literature [2, 3] suggests that with continued thermal aging, the waviness of the solder intermetallic layers decreases. This aging is accompanied by a decrease in the effective fracture resistance at this interface, especially under dynamic loading. This loss of fracture

resistance is, atleast in part, due to increase in the stress intensity factor because of decrease in the waviness. This study provides fundamental insights into this problem for thermal aging of solder-bondpad interfaces in electronic assemblies, based on detailed stress analysis and on analysis of crack-shielding mechanisms at wavy interfaces of dissimilar materials [4].

5.3 Literature Review

Numerous papers have been published on the mechanics of interfacial fracture. It started with closed-form analytical models from Rice, Suo and Hutchinson [5, 6 and 7] which then got extended [4] for different loading conditions and mode mixity. This section summarizes the important theoretical work done in interfacial fracture that is relevant to this problem.

5.3.1 Nonplanar Interfacial Mechanics

Stresses near the crack tip at bimaterial interfaces have oscillatory behavior unlike those in the bulk. Rice [5] was the first to develop a mathematical expression for that behavior which essentially implies that the material in a small zone behind the crack tip will interpenetrate even when the crack is subjected to far-field tensile loads. Suo and Hutchinson [6] provided a way to relate the bulk stress intensity factor to the interfacial stress intensity factor. This technique relies on Dundurs' parameters, characteristic length, and a non-dimensional parameter to represent the oscillatory stress field at the crack tip. Hutchinson and Suo [7] showed that under certain conditions, the oscillatory stress field can be neglected, thus de-coupling the mode I and II interfacial stress intensity factors.

However, many practical components have wavy interfaces. For example the IMC layers formed between copper plates and solder are often scalloped and wavy. The interfacial

morphology evolves steadily with time, even at room temperature, due to ongoing diffusion between the plating materials, copper trace and solder [3, 8].

Evans and Hutchinson [4] were the first to relate the effective energy release rate at a wavy interface to that at a planar interface, as shown in the following equation:

$$\frac{G^t}{G} = 1 + \frac{(f^2 - 2f)(Sin(\theta) + \tan(\psi)Cos(\theta))^2}{1 + \tan^2(\Psi)}$$

(5-1)

G^t	Energy release rate at wavy interface
G	Energy release rate at straight interface
f	Non-dimensional scaling factor
θ	Facet angle for wavy interface
Ψ	Phase angle for mode-mixity

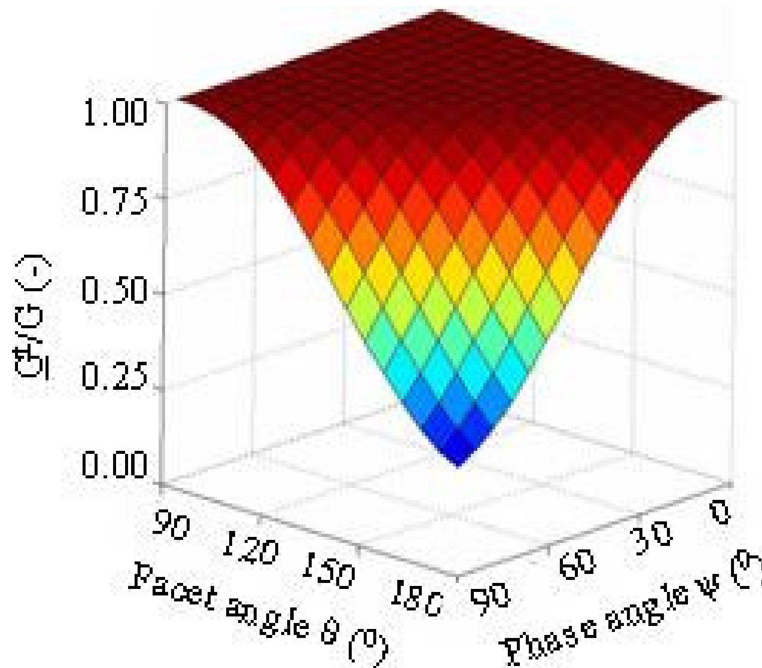

Figure 5-2: Graphical Representation of Eqn. (5-1) [27]

Fig. 5-2 is a 3D plot of the above equation and shows that G^t/G decreases monotonically with increasing interfacial waviness and phase angle. The changes in the waviness value (h/λ) reflect the changes in the interfacial morphology from rough ($h/\lambda = 5$) to smooth ($h/\lambda = 0$). For a given level of mode mixity, a rough interface clearly has a lower energy release rate for a given loading condition, and hence provides better resistance to crack propagation. Equation 5.1 is valid for a wavy interface between two elastic, semi-infinite solids.

5.3.2 Elastic-Plastic Interfaces

The major limitation of the above theories is that they are not valid in the presence of elastic-plastic deformations. Evans et al [9] suggested that the total energy required for interfacial cracking is a combination of the roughness shielding parameter and plastic work dissipation. Wei and Hutchinson [10] proposed a unified model which combined the Suo Shih Varias (SSV) model by Suo, et al [11] and embedded process zone model (EPZ) by Tvergaard and Hutchinson [12]. The model predicts that as peak stress increases for a fixed value of G, the interfacial toughening due to plasticity increases.

Lane, et al [13] and Wei and Hutchinson [14] defined the criteria for limiting conditions of interfacial toughening due to plasticity at the elastic/plastic interface. However, the effect of aging on the contribution of interface adhesion and plastic work to fracture of wavy interface is still not well understood.

5.3.3 Effect of Aging on Roughness

One of the most common wavy interfaces in electronic devices are at the IMC layers formed between copper and solder. These interfaces thicken and weaken with aging. Yao & Shang [13],

Luhua and Pang [2], Song, et al [1], Jang, et al [15], Tu, et al [16] have reported this. Fig. 5-3 shows the variation in the morphology of Cu_6Sn_5/Cu_3Sn interface of a SnAgCu interconnect with Organic Solderability Preservative (OSP) finish, at various conditions of thermal cycling [17].

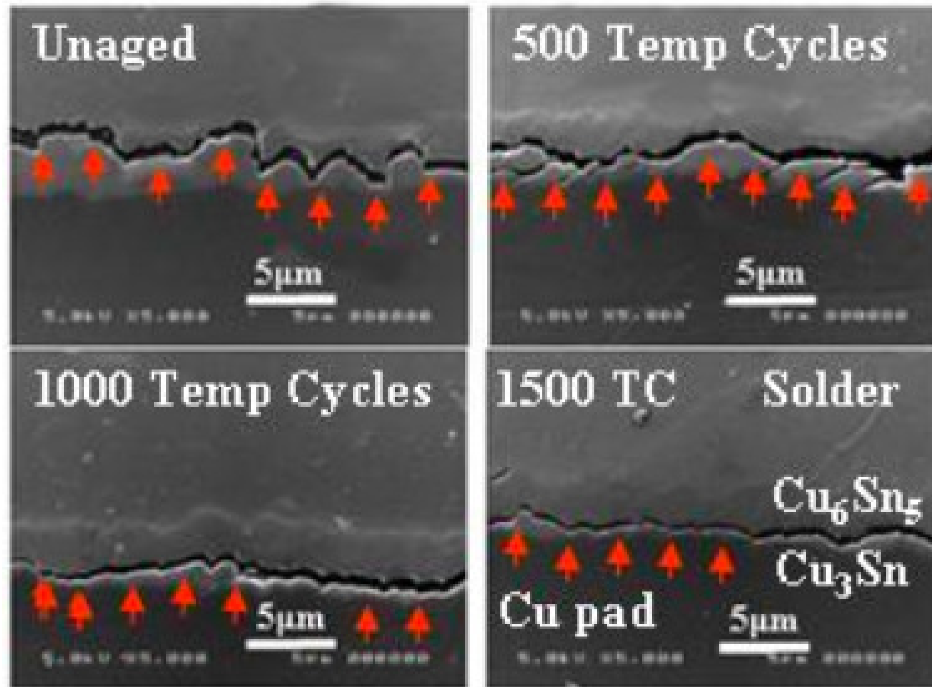

Figure 5-3: Changes in Interface Morphology due to Aging [1]

Any significant change in interfacial fracture strength can affect the failure site, which can have a direct impact on the fatigue life of a multi-layered stack. Thus a clear understanding is required about the way the fracture strength changes due to the aging process.

5.3.4 Changes in stress intensity factor due to crack shielding mechanism

Evans and Hutchinson [66] investigated the effects of non-planarity on interfacial fracture. Their model is based on a bimaterial elastic interface which consists of a kink along a crack surface. When the crack surfaces contact at the kink, the stress intensities at the crack front differ from the applied values to an extent governed by the kink angle, the kink amplitude and the friction

coefficient. The contacts resist the motion of the crack surface by means of friction and locking and thereby modify the energy release rate at the crack front. The modified strain energy release rate governs the effect of the contacting facets on the overall interface fracture resistance [4].

The mathematical model for predicting the effective stress intensity factors for non-planar interfaces is given by-

$$K_2^t + iK_1^t = K_2 + iK_1 - f(\xi)e^{i\omega}(K_1 Sin\theta + K_2 Cos\theta) \tag{5-2}$$

where, ξ is the size of the characteristic length on the crack surface, $f(\xi)$ is a non-dimensional scaling factor for the stress intensity factors, K_i^t is the stress intensity factor of the non-planar interface at the ith mode and θ is the facet angle of the non-planar interface. Equation (5-2) gives the coupled stress intensity factors compared to Equation (5-1) which gives the strain energy release rates as a function of interface facet angles. Because of the coupled nature of the stress intensity factors at the interfaces, usually strain energy release rate is a preferred mode of expressing the fracture properties. Thus, according to this derivation, the crack shielding due to the waviness of the non-planar interface decreases the stress intensity factor at the crack tip. The strain energy release rate of the crack depends on the waviness, phase angle of loading, and the properties of the materials that make up the interface.

5.3.5 Fracture Toughness Experiment for Wavy Solder Interface

Yao & Shang [3] evaluated the fracture characteristic of a solder intermetallic interface for different cooling rates by standard fatigue testing. A thin layer, 0.2 mm thick, of solder alloy (commercial grade eutectic Sn-Pb solder paste with standard mesh size and RMA rosin flux) was sandwiched between two copper (OFHC) beams with the same thickness of 1.6 mm. The cooling

rate was varied after the reflowing of the solder and thus the waviness of the solder/Cu interface was varied. The cooling rates were estimated to be approximately 100°C/s for water quenching, l°C/s for air cooling and 0.01°C/s for furnace cooling. Fig. 5-4 shows the difference in microstructure across the interface. The waviness (h/λ) is seen to be inversely related to the cooling rate. The slower the cooling rate, the flatter the interface and the faster the cooling rate, the wavier is the interface. In the water-quenching condition, the cell was small and nearly hemispherical while in the furnace cooling case, the intermetallic cell flattened out considerably into a "pancake" shape and the thickness of the intermetallic layer was larger.

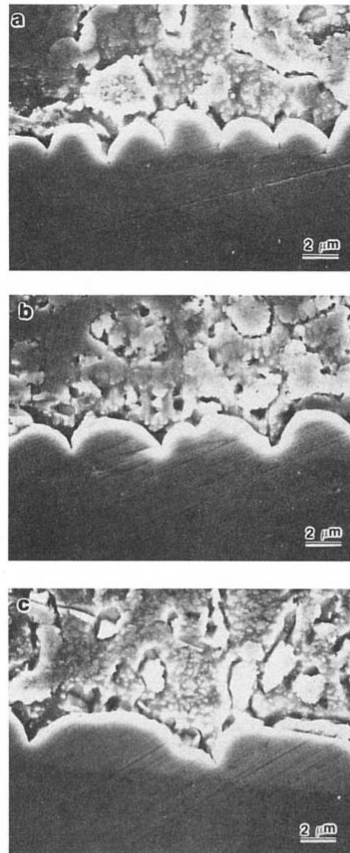

Figure 5-4: Interface Microstructures in Eutectic Sn-Pb/Cu Solder Joints: (a) Water Quenching, (b) Air Cooling, and (c) Furnace Cooling [3]

The sandwich specimens used by Yao and Shang were precracked at the edge of the interface between Cu_6Sn_5 intermetallic and solder, by cycling the specimen at about one-third to one half of the fracture toughness of the interface. The precracked specimens were then loaded cyclically in a sinusoidal waveform with a load ratio of 0 and at a frequency of 5 Hz. The tests were carried out in room air (22°C, 55% RH). Fatigue crack was monitored by an optical traveling microscope at a magnification of 10. Fatigue crack growth rates from less than 10^{10} to 10^{7} mm/cycle were measured. Fatigue crack growth threshold was approached by a load-shedding procedure where the load increment was less than 10 percent of the previous load. The crack growth driving force, range of strain energy release rate, ΔG, for the flexural peel specimen was calculated using the J-integral formulation. Applying beam theory, ΔG is derived using Eqn. (5-3)-

$$\Delta G = \frac{\Delta P^2 (L+a)^2}{2BE_s}\left(\frac{1}{I} - \frac{1}{I^*}\right)$$

(5-3)

where ΔP is the range of applied loads for a fatigue cycle, E_s, the elastic modulus of the Cu substrate, B, the specimen width, L is the distance from the loading line to the precrack, I and I* are the moments of inertia of the bottom beam and the joint, respectively.

Fig. 5-5 shows the crack growth behavior under the 3 different cooling conditions. Cooling rates have different effects at low and high energy release rates. At the low energy release rates, increasing cooling rate resulted in enhanced fatigue threshold for interface crack growth. On the contrary, at the high energy release rates, large reductions in the apparent fracture toughness followed the increases in the cooling rate. The difference in the cooling rate resulted in

changes in the failure mechanism. At low energy release rates, fatigue cracks propagated along the interface between the solder and the intermetallic layer. At high energy release rates, the failure mechanism was altered from cohesive in the furnace-cooled condition, to interfacial in the water-quenched, with a mixed failure mode in the intermediate cooling rate of air cooling.

In this study, the authors used a simple linear elastic model to estimate the strain energy release rate at the interface from the load and displacement data obtained from the test. The effect of interfacial waviness is neglected in this step, although the authors do discuss a crack-sliding model to qualitatively explain the decrease in the fatigue threshold with decreasing cooling rate. In their results, the authors represent the changes in fracture resistance by changing the effective fatigue threshold energy release rate (ΔG_{th}), as shown in Figure 5-5.

The reality is that the change in fracture resistance with change in interfacial waviness is only partially due to changes in the intrinsic fracture toughness of the interface, and partially due to changes in the stress intensity factor due to the crack shielding mechanism discussed above. These simultaneous changes cause changes in the stress-strength interferences at this interface.

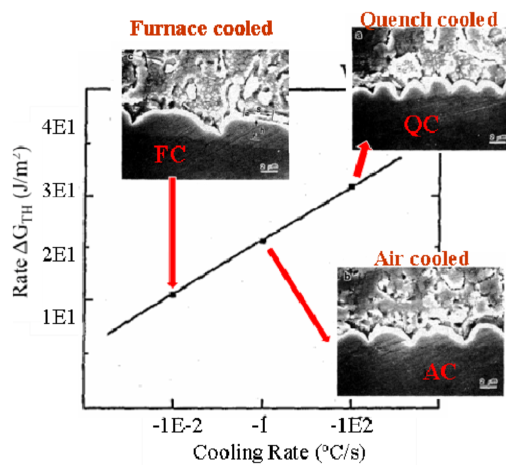

Figure 5-5: Threshold Strain Energy Release Rate vs Cooling rate

5.4 Approach

The approach taken in this work has been to initially build a finite element model of Shang's test setup [3] to estimate the stresses at the solder/copper interface with a crack being introduced in it. The stresses obtained here are used to estimate the strain energy release rate and phase angle of loading for a planar interfacial crack.

The difficult problem of determining the detailed stress state at the tip of the interface crack, as characterized by the phase angle or the individual stress intensity factors, requires numerical computation. To properly combine the macro scale of the specimens with the micro scale of the IMC features, a global-local modeling approach has been undertaken.

These values are then compared to results published by Yao and Shang [3]. The comparison gives us insight into the effect of waviness, plasticity and intrinsic interfacial bond strength on the threshold strain energy release rate.

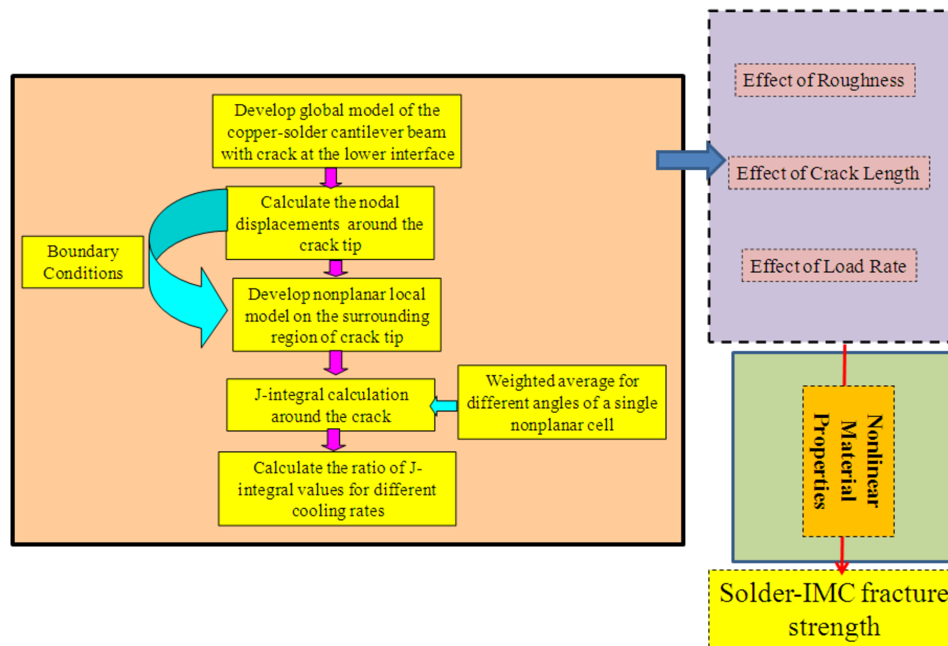

Figure 5-6: Investigation Flowchart

5.5 Finite Element Analysis

Shang's experimental setup was used for the model and the results were used as a basis of comparison. Multiscale global-local modeling concept was used to be able to effectively capture the micro features of the IMC structure. The following are the important aspects of the macro and micro model.

5.5.1 Macroscale Model

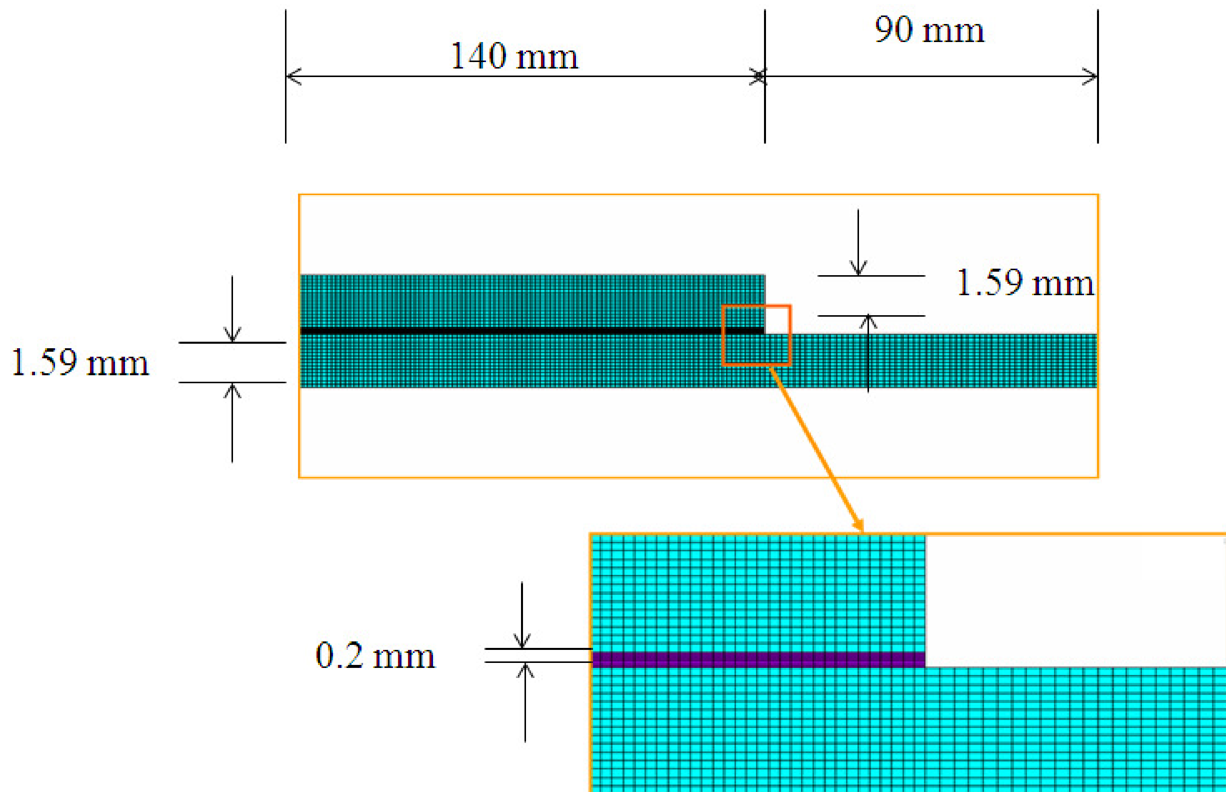

Figure 5-7: Global Model Geometry

The global or macroscale model essentially is a cantilever beam as in Shang's experiment with bending load. A solder layer with finer mesh is sandwiched between the two copper layers with thinner mesh. The meshing is done such that the nodal displacements can be effectively

transferred to the micromodel. Fig. 5-7 shows the structure of the model along with the dimensions. An 8-noded 2-D element was used with two translational degrees of freedom per node. The total number of nodes is 195,709. Left edge of the entire structure is constrained in all directions while a fixed load is applied at the other end. This load value is obtained by using Eqn. (1) in [3] where inputting the strain energy release rate values gives the load applied. Material Properties used are detailed in Appendix 1.

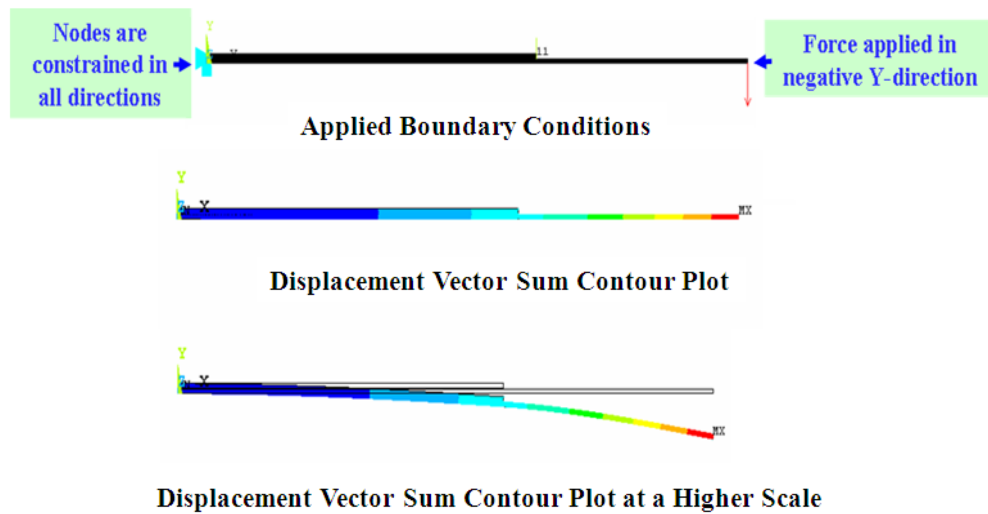

Figure 5-8: Global Model Displacement Plot

The macromodel has a crack seeded at the lower copper-solder interface of length that was parametrically varied with 3 different lengths- 10, 20 and 30 mm. The meshed geometry is then loaded at the end tip while the other end was fixed in all end directions like a typical cantilever. The nodal displacement plot in Fig. 5-8 shows the bending of the beam due to the load. As expected the highest stress is at the crack tip under this loading condition.

5.5.2 Microscale Model

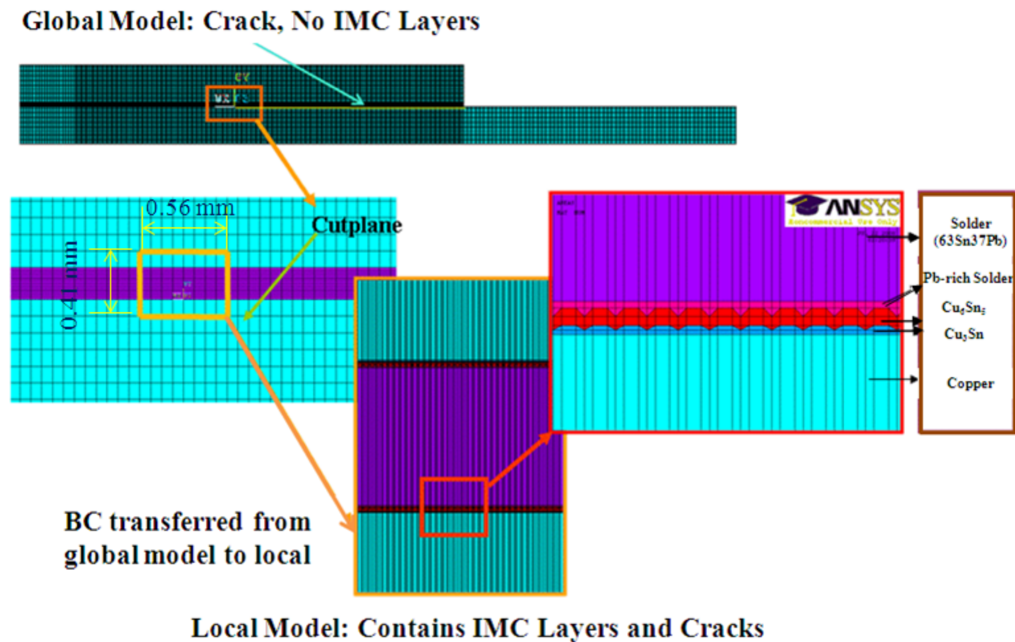

Figure 5-9: Global and Local Model

A small region around the crack tip was then analysed with a fully-detailed microscale model. Fig. 5-9 shows the location and size of this local model. The IMC layers with their detailed roughness features were incorporated in the model. The IMC cells were approximated as trapezoidal cells with rounded corners. The tin-rich (Cu_6Sn_5) IMC layer had a more wavy interface than the copper-rich (Cu_3Sn) layer. Fig. 5-10 shows further details regarding the structure of the IMC cells. Calculations made from Shang's data confirmed that the interfacial cell angle (Table 5-1) remains approximately same throughout the aging process. This is expected because the angle depends on the interfacial energy which doesn't change much with cooling rate. An 8-noded 2-D element was used with two translational degrees of freedom. The total number of nodes is 180,149. Material Properties used are detailed in Appendix 1 and the

boundary conditions applied are obtained from the nodal displacements of the macromodel at the matching nodes in the edges.

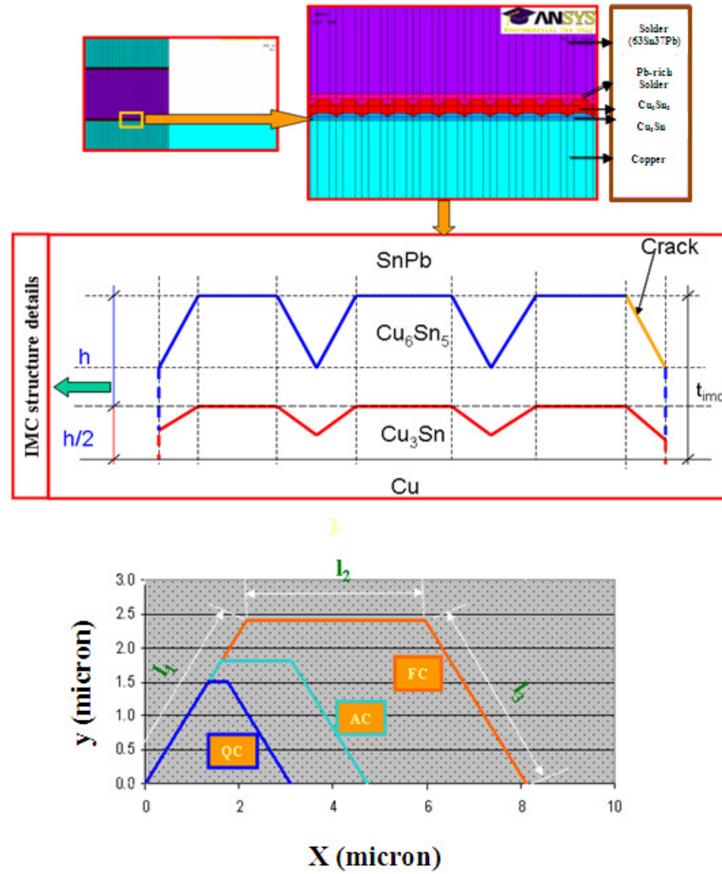

Cooling Condition	Height, h (μm)	Width, l_2 (μm)	Roughness, $2\,l_1/s$	Thickness of Pb-rich region (μm)	Measured Wavelength λ (μm)	Angle (degrees)
Furnace Cooling	2.4 ± 0.3	3.8 ± 0.5	1.3	2	8.19	48.3
Air Cooling	1.8 ± 0.4	1.5 ± 0.5	2.4	1.5	4.74 ± 1	48
Quench Cooling	1.5 ± 0.3	0.4 ± 0.2	7.5	1.25	3.07± 0.2	47.55

Angle remains constant (approx 48 degrees)

Figure 5-10: IMC Layer Morphology Details for 3 Cooling Rates

A comparative view of the SEM pictures and model geometry of the IMC layers has being shown in Fig. 5-11. Close to the upper interface of Cu_6Sn_5 lead-rich solder has been incorporated. This is because during the aging process, lead particles are accumulated towards the interface. The properties of all the different material layers are shown in Appendix 5.

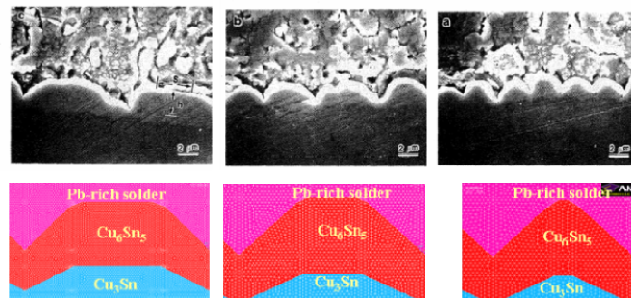

Figure 5-11: Geometric Comparison of the IMC Layers in Shang's Experiment and FEA

5.5.3 Calculation of Strain Energy Release Rate

Cracks are introduced in the form of unmerged nodes at the Cu_6Sn_5 and lead-rich solder interface. Since, each cell has three different slopes; different crack positions (total of 54) are simulated for each of the three roughness levels. The boundary conditions are varied for different crack lengths which are obtained from the nodal displacements of the macromodel.

The strain energy release rate computation was obtained by J-integral computation which can be compared to the experimental results. For this J-integral calculation, a local coordinate system has been specified at the tip of the crack with the crack normal plane being perpendicular to the local x-axis. To prevent interpenetration near the crack tip, contact elements are used at that interface (Fig. 5-12). This resulted in fast convergence of the J-integral value at the crack tip

across contours (Fig. 5-13).

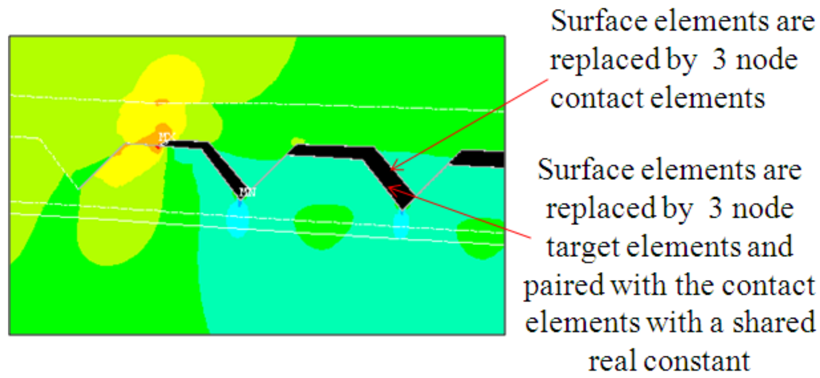

Figure 5-12: Nodal Von-Mises Strain Plot at the Crack Tip

J-integrals of all the crack positions are averaged which is subsequently compared across the different roughness levels. Thus, the whole cell morphology is taken into account in this process with different mode mixity levels.

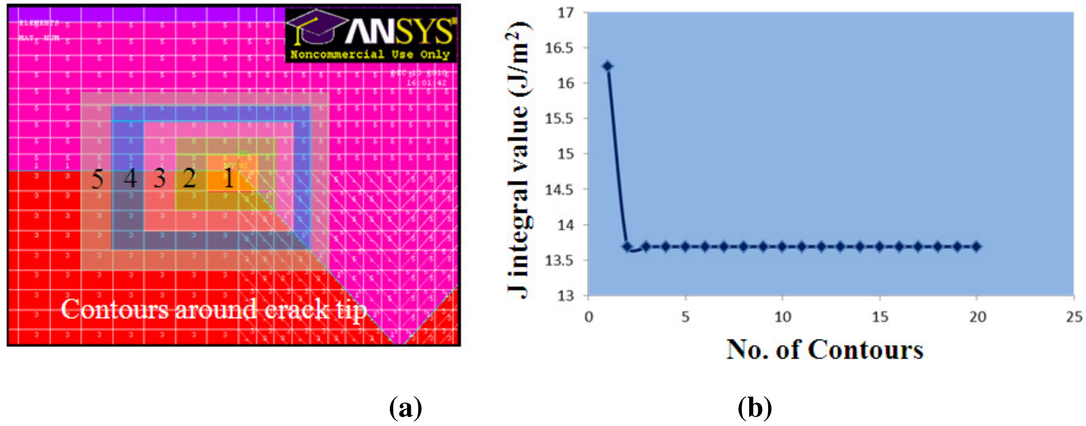

(a) **(b)**

Figure 5-13: (a) J-Integral Contours around the Crack Tip (b) Convergence of the J-Integral Value

5.5.4 Combined Effect of Crack Length and Roughness

Fig. 5-14 shows the typical crack behavior across one IMC cell in FC configuration. The trends

are similar for each of the three initial crack lengths where strain energy release rate increases steadily along upslope, holds steady in the horizontal portion and then drops down along the down slope. So, it takes more energy to propagate a crack at an angle than horizontally.

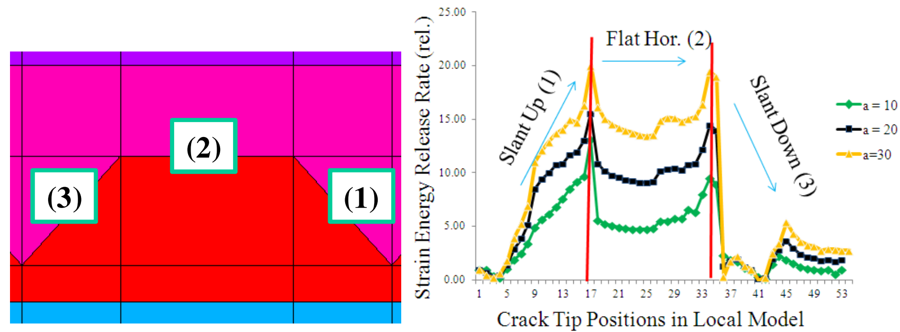

Fig. 5-14: Crack length Effect on Strain Energy Release Rate

The strain energy release rate averaged over one unit cell for different initial crack lengths was then plotted on a semi log scale alongside Shang's experimental results (Fig. 5-15). Both linear and nonlinear properties are used to see the role that plasticity plays over here. Also, a fit curve of Hutchinson's equation Eqn. (5-1) has been plotted in this graph. The results are normalized to the fastest cooling rate so that the role of aging can be tracked. As can be clearly observed, elastic FEA predicts stronger drop than measured values and simple analytical models. The curve is convex upwards as cooling time increases. Plasticity further adds to the decrease rate of G_{th} with cooling time.

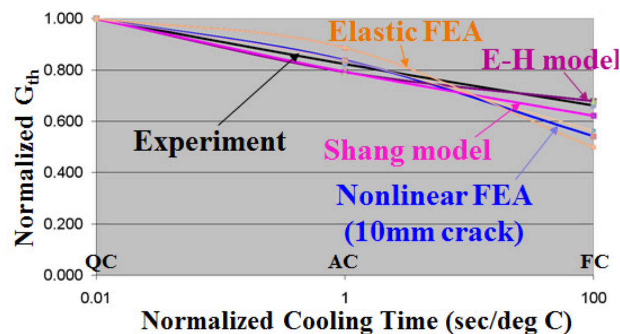

Figure 5-15: Comparisons of Results from Shang's Experiment and FEA (I)

Fig. 5-16 shows the comparison of the nonlinear simulation results for different initial crack lengths alongside the experiment results. It can be observed that FEA predictions are not very sensitive to initial crack length. Also, longer crack length makes the curve slightly more convex

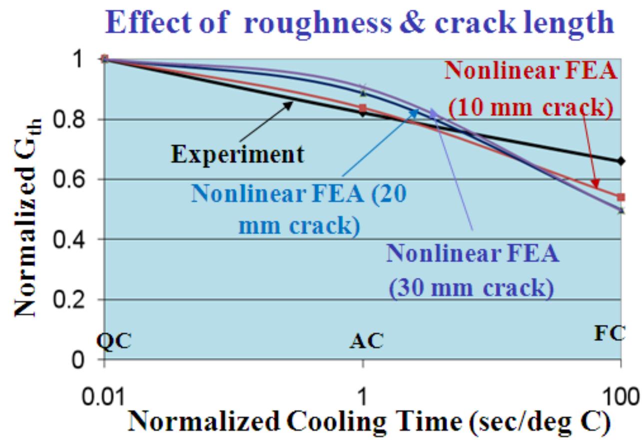

Figure 5-16: Comparisons of Results from Shang's Experiment and FEA (without strain rate effect)

5.5.5 Combined Effect of Loading Rate and Roughness

The FEA results in the previous sections didn't include the effect of loading rate. To understand that effect, creep properties of solder (Appendix 1) are now included in the global models. The same sets of runs have been performed and compared across different roughness levels. The 5 Hz frequency loading condition didn't produce much creep strain and thus the results (Fig. 5-17) are negligibly different from the ones without the strain rate effect.

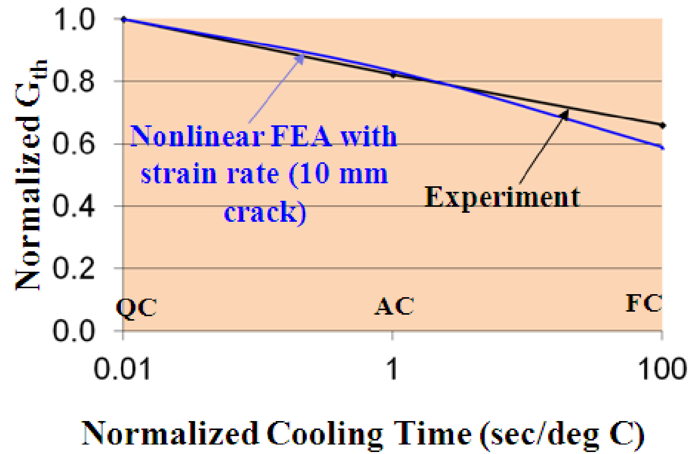

Figure 5-17: Comparisons of Results from Shang's experiment and FEA (with strain rate effects)

5.6 Summary and Conclusion

A finite element framework has been generated that can predict the real interfacial crack behavior, by incorporating the geometric complexities of a wavy interface and the material nonlinearities, that cannot be addressed in simple, analytic fracture models available in the literature. Crack behavior across one unit intermetallic cell has been compared across different roughness levels and various initial crack lengths. Interfacial toughness estimates show stronger sensitivity to roughness in FEA models than in simple analytic models. However, the effect of initial crack length is minimal based on these numerical results. By introducing rate sensitive properties in solder, the strain rate effect has been estimated on the crack behavior, which is found to be weak due to the type of loading condition. The existing analytical model's predictions in general are reasonably close to what the FEA models predict which suggests that they can be used with good confidence for approximate assessment of the strength of solder interfaces for moderate roughness levels.

Acknowledgement

The work reported here was sponsored by the members of the Electronic Products and Systems Consortium at the Center for Advanced Life Cycle Engineering at the University of Maryland.

References

1. Song, B.; Azarian, M.H.; Varghese, J.; Dasgupta, A. and Pecht, M., "Dynamic Loading Durability and Failure Site Transition in Enig-Sn37pb Interconnects in a Stacked Die BGA Package", IEEE Transactions on Components and Packaging Technologies, 2006.
2. Xu, L. and Pang, J.H.L., "Effect of Intermetallic and Kirkendall Voids Growth on Board Level Drop Reliability for SnAgCu Lead-free BGA Solder Joint ", Proceedings of the IEEE Electronic Components and Technology Conference, 275-282, 2006.
3. Yao, D. and Shang, J.K., "Effect of cooling rate on interfacial fatigue-crack growth in Sn-Pb solder joints", IEEE Trans. Components, Packaging, and Manufacturing Technology, Part B, 19(1):, 154-165, 1996.
4. Evans A.G. and Hutchinson, J.W., "Effects of Non-Planarity on the Mixed Mode Fracture Resistance of Bimaterial Interfaces", Acta Metallurgica, 1989. 37(3): p. 909- 916.
5. Rice, J. R., "Elastic Fracture Mechanics Concepts for Interface Cracks", Journal of Applied Mechanics, 1988. 55: p. 98–103.

6. Suo, Z. and Hutchinson, J. W., “Sandwich Test Specimens for Measuring Interface Crack Toughness”, Materials Science & Engineering A: Structural Materials: Properties, Microstructure and Processing, 1989. A107 (1-2): p. 135-143.
7. Hutchinson, J. W. and Suo, Z., “Mixed Mode Cracking in Layered Materials. Advances in applied mechanics”, 1992. 29: p. 63-191.
8. Tu, P. L.; Chan, Y. C.; Hung, K. C. and Lai, J. K. L., “Growth Kinetics of Intermetallic Compounds in Chip Scale Package Solder Joints”, Scripta Materialia, 2001. 44(2): p.317-323.
9. Evans, A. G., Ruhle, M., Dalgleish, B. J. and Charalambides, P. G., “The fracture energy of bimaterial interfaces in Metal-Ceramic Interfaces”, 1990, Metall. Trans. *A* 21A:2419–29.
10. Wei, Y and Hutchinson, J. W., " Models of interface separation accompanied by plastic dissipation at multiple scales”, 1999, Int. J. Fract 95:1–17.
11. Suo, Z.; Shih, C. F. and Varias, A. G., “A theory for cleavage cracking in the presence of plastic flow”, Acta Metall. Mater., 1993, 41:1551–57.
12. Tvergaard, V. and Hutchinson, J. W., “Toughness of an Interface along a Thin Ductile Layer joining Elastic Solids”, 1994, Philos Mag. A 70:641–56.
13. Lane, M.W.; Dauskardt, R.H.; Vainchtein, A. and Gao, H. “Plasticity contributions to interface adhesion in thin-film interconnect structures”, 2000, J. Mater. Res. 15:2758–69.
14. Wei, Y. and Hutchinson, J.W., “Interface strength, work of adhesion and plasticity in the peel test." Int. J. of Fracture, 93, 315-333, (1998).
15. Jang, J.W.; Lin, J.K. and Frear, D. R., ‘Failure Morphology after the Drop Impact Test of the Ball Grid Array Package with Lead-Free Sn-3.8Ag-0.7Cu on Cu and Ni Under-Bump Metallurgies”, Journal of Electronic Materials, 2007. 36(3): p. 207-213.

16. Tu, P. L.; Chan, Y. C.; Hung, K. C. and Lai, J. K. L., "Growth Kinetics of Intermetallic Compounds in Chip Scale Package Solder Joints", Scripta Materialia, 2001. 44(2): p.317-323.

17. P. L. Liu and J. K. Shang, "A Comparative Fatigue Study of Solder/Electroless-Nickel and Solder/Copper Interfaces", Journal of Material Research, 2000. 15(11): p. 2347- 2355.

Appendix 1: Material Properties for Finite Element Model

The linear material properties used in the FEA analysis are in Table A1-1.

MATERIAL	Young's Modulus (GPa)	Poisson's Ratio
Copper	110	0.343
Sn-Pb Solder	32	0.38
Pb-rich Solder	23.5	0.35
Cu_6Sn_5	85.56	0.309
Cu_3Sn	108.3	0.299

Table A1-1: Linear Properties for Solder-IMC Model (Source- www.matweb.com)

The elastic-plastic properties used in the FEA analysis are depicted in Fig. A1-1 & A1-2.

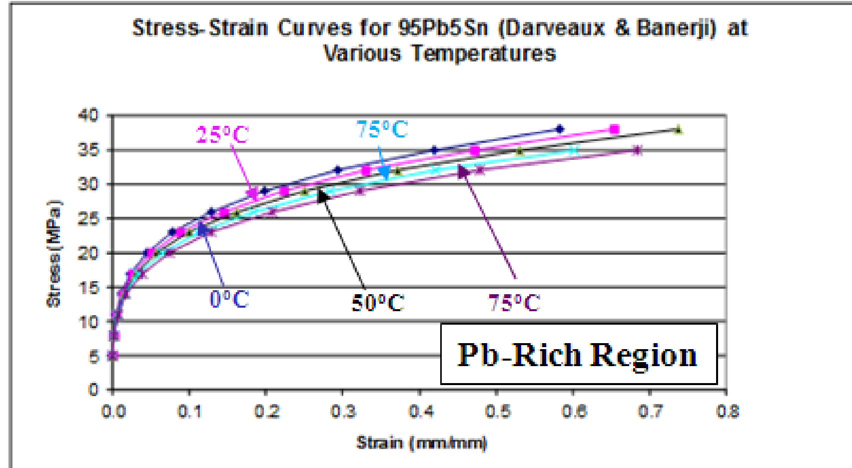

Figure A1-1: Stress-Strain Curves for 95Pb5Sn (Darveaux & Banerji) at Various Temperatures

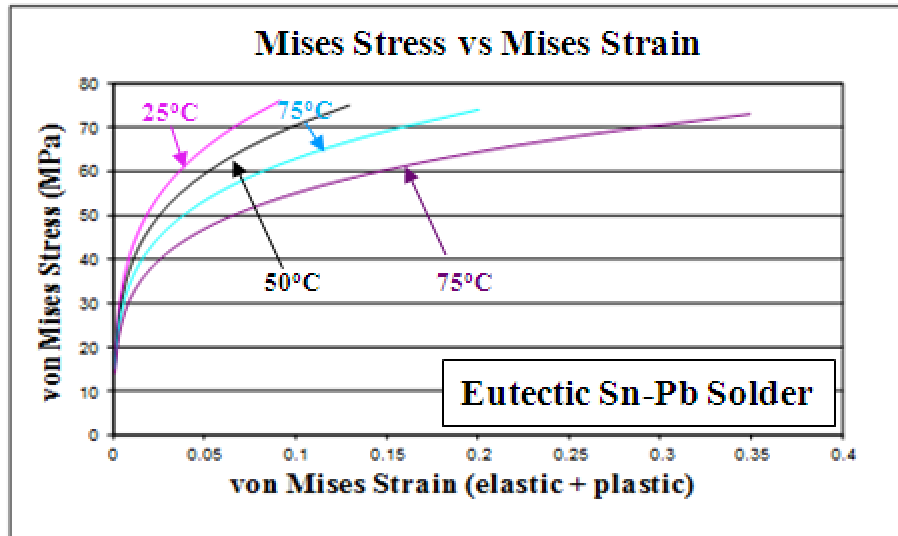

Figure A1-2: Von Mises Stress vs Von Mises Strain Curves for SnPb (Qian) at Various Temperatures

Garofalo Creep Law (Eqn. A1-1) was used for the rate-sensitive modeling. The model constants were extracted from Qian et.al, 2004.

$$\dot{\varepsilon}_{cr} = C_1[Sinh(C_2\sigma)]^{C_3}\exp(-C_4/T) \qquad \text{(A1-1)}$$

where *C1 =66.40; C2 =0.115E − 06; C3 = 2.2; C4 = 7130; T = 298K*

Chapter 6: Dissertation Contributions & Benefits

The contributions and benefits from the thesis have been classified below according to the two different parts of the study.

6.1 Gold Bumps in Flip-Chip Interconnects

- Quantified the effect of bonding parameters on the Au-Au bond strength in Au-Au flip-chip joints.
- Provided insights into the relative contribution from diffusion-assisted creep mechanisms for the bond strength growth over time. Demonstrated that the creep-assisted growth in contact area correlates very well with measured growth rate of bond strength.
- Constructed a diffusion-based empirical model to predict the bond strength for different bonding parameters and roughness features.
- Used detailed finite element viscoplastic modeling to identify the role of the most influential surface features, material properties and bonding parameters, that affect the interfacial bond strength for flip-chip interconnects. Demonstrated that the FEA model prediction of bond strength evolution has very similar trends as that from simpler diffusion-based analytic models.
- Developed a response surface model, based on the detailed FEA, that can be used for optimizing process parameters for adhesive joining of flip chips that have gold metallization.

6.2 Solder Bumps in Flip-Chip Interconnects

- Investigated the influence of complex IMC microstructural morphology on solder interconnect strength, using detailed global-local, 3D, elastic-plastic-creep finite element modeling and fracture mechanics concepts.

- Developed fundamental insights into the effect of different parameters (interface roughness as characterized by statistical measures of the asperity profile, crack length, load rate) on solder-IMC interface fracture strength, through detailed micro-scale modeling of the IMC structure, under bending load.

- An impact of this study is that the proposed computational framework can be used to predict the strength of solder joints for various other solder compositions and under different aging processes, based on their effect on interfacial IMC morphology.

Chapter 7: Limitations and Future Work

The thesis work has its limitations that can be improved upon by further studies. Below is a summary of the limitations that provides the foundation for future work:

7.1 Gold Bumps in Flip-Chip Interconnects

- The bonding matrix for the experiments in this study did not capture the effect of temperature with sufficient rigor or detail. Examining the role of temperature on the saturated bond strength will provide broader understanding of the role of all the bonding parameters.
- The effect of surface diffusion and grain-boundary diffusion contributions have been neglected in the computational model, compared to the bulk-diffusion contribution, when estimating the growth of the contact area. This approximation is based on published properties of gold, but needs to be experimentally verified for the specific type of gold used in the bond pads. Therefore, in subsequent studies the role of such other forms of diffusion needs to be taken into account.
- FEA model is limited on the roughness details because of the 2D single-asperity representation for the time-dependent modeling. More detailed 3D modeling of realistic multi-asperity contacts should be undertaken to verify the findings of this study. Such a study could start by assuming the asperity formations as isotropic and then extending them to anisotropic random asperity features.
- Local temperature effects at the interface due to exothermic bonding reactions can locally spike the diffusion and creep rates, which hasn't been captured in the present study. A

detailed atomistic scale study could provide insight on any local temperature rise and its effect on the overall bond formation.

- The surface oxides can be one of the causes of the initial time lag to form any measurable bond strength. However, this needs to be clarified by atomistic scale simulations that will be useful to understand the bond strength behavior in the short bonding time region.

- The statistical variability of the input parameters, in particular the asperity distribution, has not been captured in great detail in this study. Such variability can potentially impact the actual bond strength and needs to be considered in subsequent studies.

7.2 Solder Bumps in Flip-Chip Interconnects

- FEA model developed in this study can be further calibrated by experiments conducted on other solder alloy compositions.

- Broader aging conditions can be incorporated in this study to help calibrate the FEA model and better understand the roughness effects.

- Parametric variation of loading rates can be applied on the model to properly determine the strain rate effect.

- The properties at smaller length scales can vary considerably due to strain gradient effect. Experiments can be conducted to extract strain-gradient properties which can be used to further refine the model. (true for both the studies)

Acknowledgments

This work is sponsored by the members of the CALCE Electronic Products and Systems Consortium at the University of Maryland, College Park.

Appendix 1: Characteristics of the Pull-Test Specimen (Chapter 3)

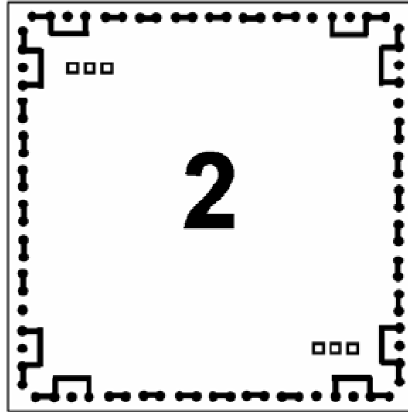

Figure A1-1: Pull Test Specimen Schematic

Size: 5.0 x 5.0 mm

Pitch of the Bumps: 130 μm

Bump for adhesive bonding:

Finish: Standard Al bondpad

Galvanic Au Bump

Height: 20 mm (measured: 20.9 – 22.5 mm)

Bump Height Variation over Die: 0.2 μm- 0.7 μm (measured)

Size: 81 mm, octagonal (measured 86-89 μm)

Hardness: 40.9-49.0 HV

Tensile Strength: 130 MPa (soft gold) to 220 MPa (hard gold)

Quantity of Bumps Overall: 84

Quantity of Connected Bumps: 58

Appendix 2: Specifications of Pull Tester (Chapter 3)

Figure A2-1: Pull Tester

Y axis Maximum Force: 100 Kg

X axis Maximum Force: 5 Kg

Z axis Maximum Force: 10 Kg

Z axis Travel: 65 mm

Z axis accuracy over full travel: ± 10 µm

Z axis maximum test speed: 5 mm/second

Work Holder Working Envelope: X 220 mm, Y 220 mm, Z 50 mm

Load Cartridges: All load cartridges have 4 software selectable load ranges as standard

Accuracy: Total system accuracy ± 0.25 % of load range selected. Maximum load cartridge accuracy and repeatability to within 0.01%

Compliance: European CE regulations- EMC directive, low voltage directive and mechanical safety directive

International Certification: Compliant with European CE Regulations- EMC Directive, Low Voltage Directive, Mechanical Safety Directive

Appendix 3: Aluminum Pull Test Fixture Design (Chapter 3)

(All dimensions here are in mm)

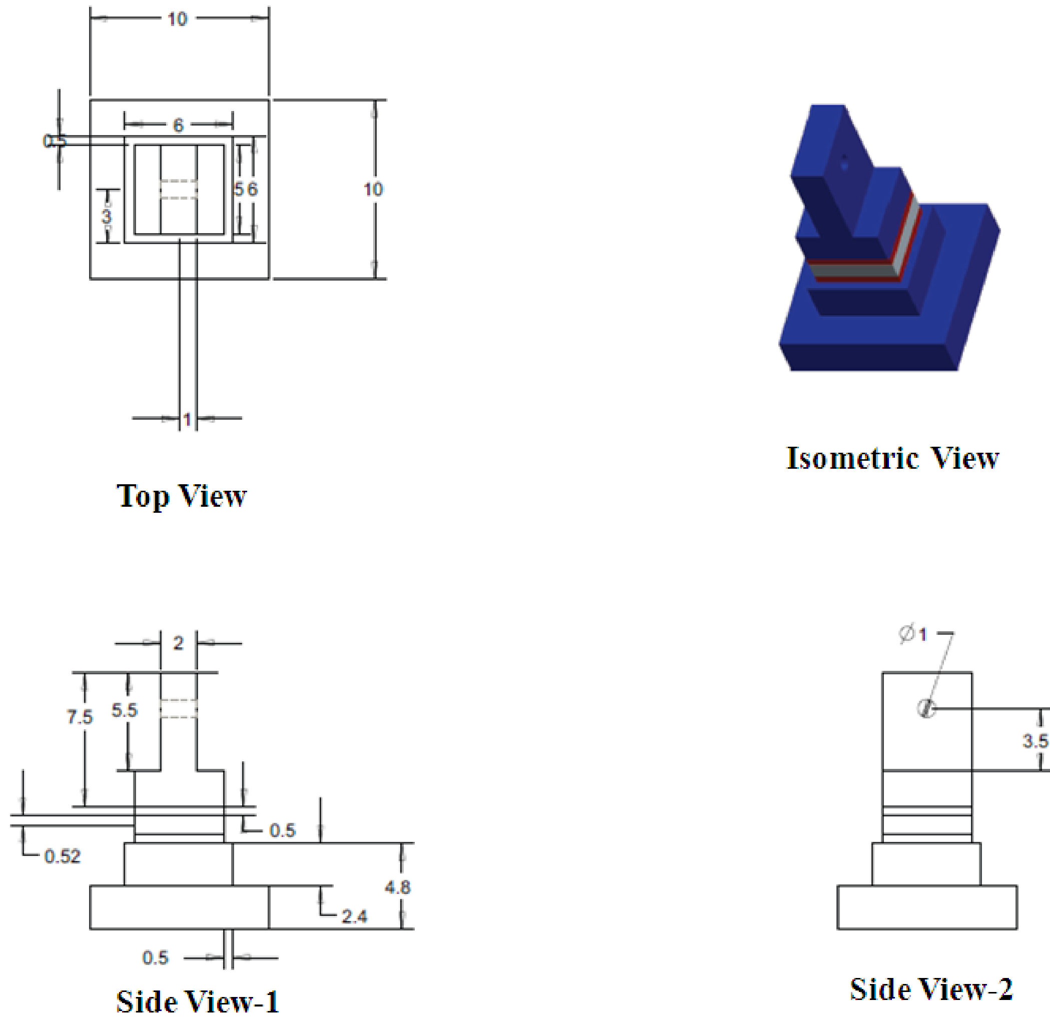

Figure A3-1: Pull Test Fixture Design

Appendix 4: Surface Characterization Plots (Chapter 3)

Below are the surface profiles (Top and Isometric View) from which the roughness parameters were measured:

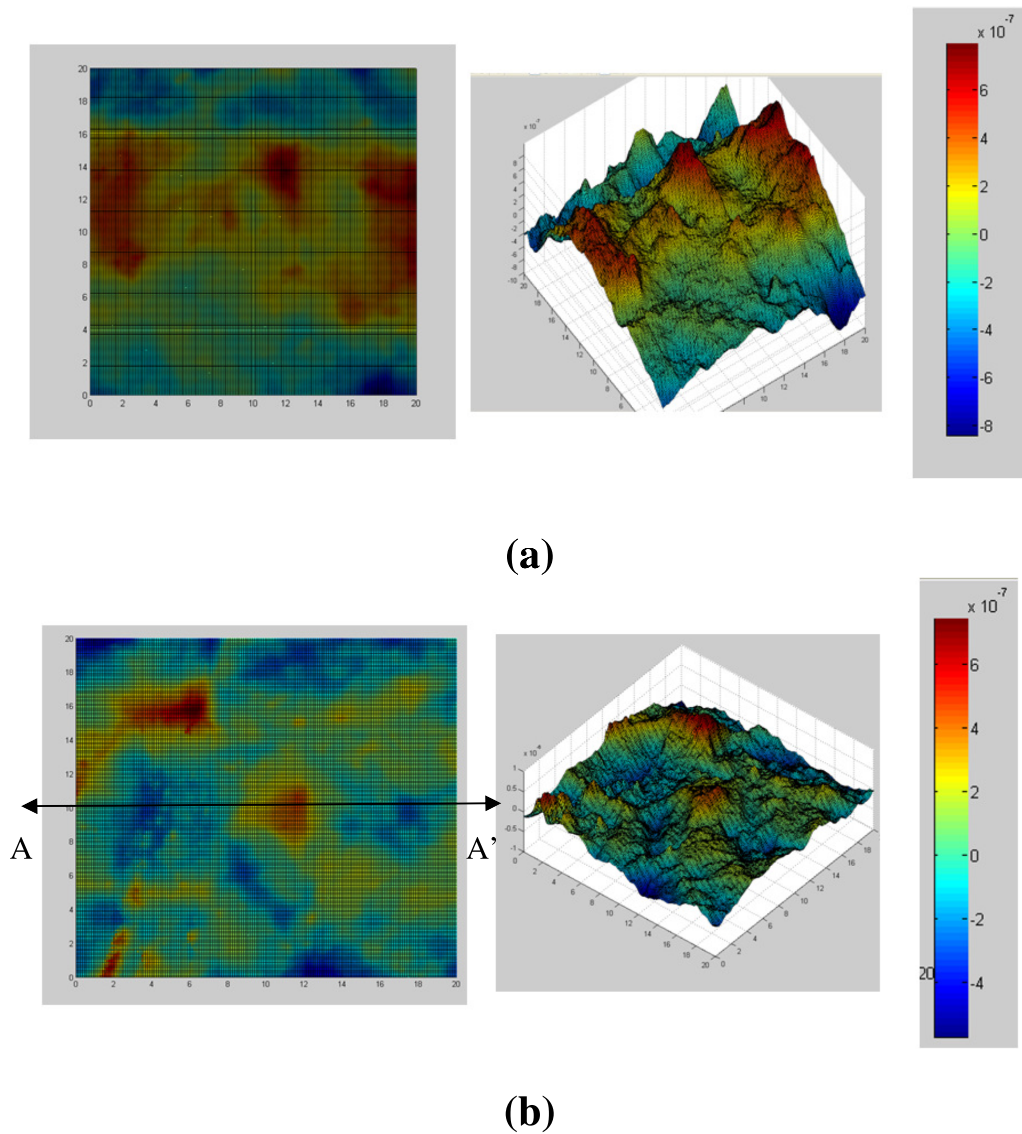

Fig. A4-1: 3D Suface Profile No.1 (a) Unmated (b) Mated

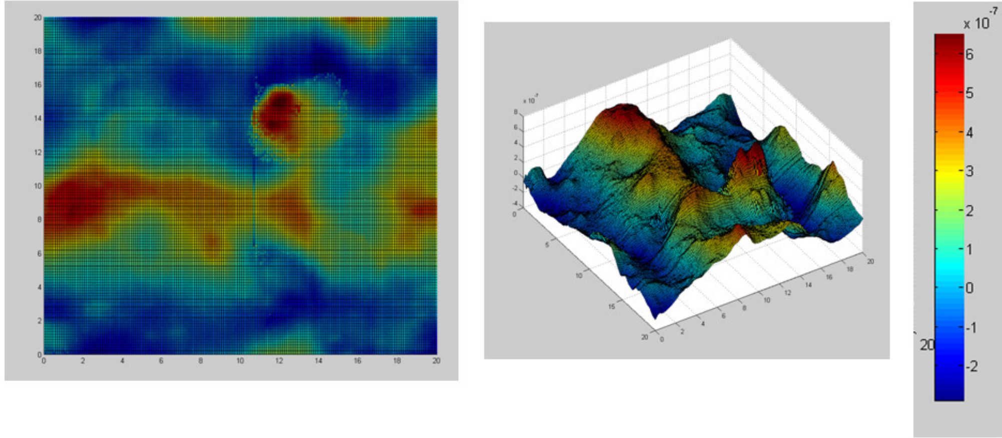

(a)

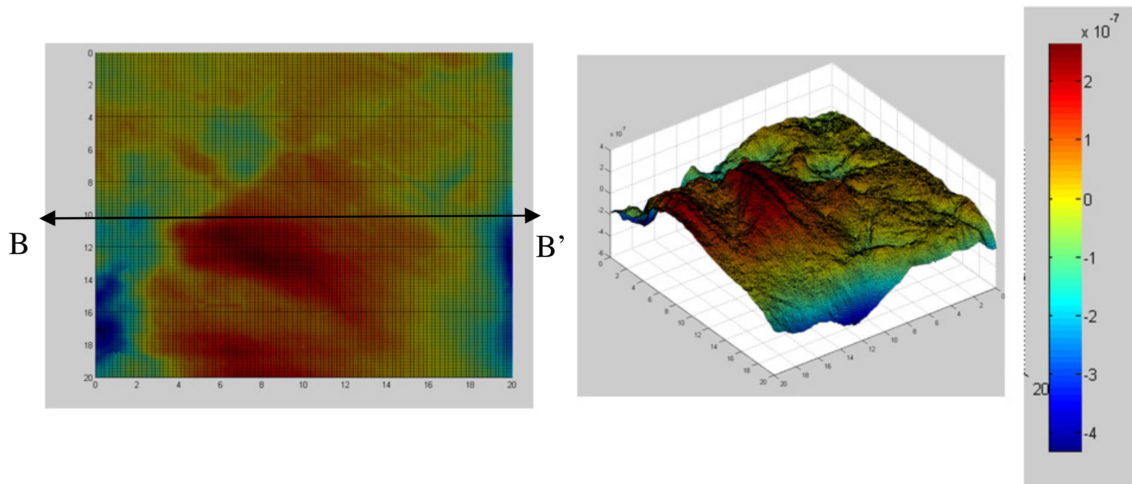

(b)

Fig. A4-2: 3D Suface Profile No.2 (a) Unmated (b) Mated

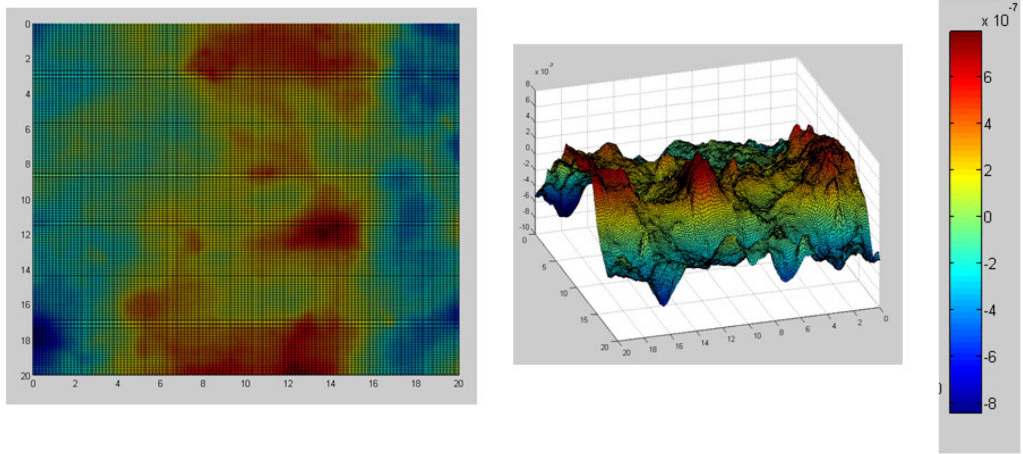

(a)

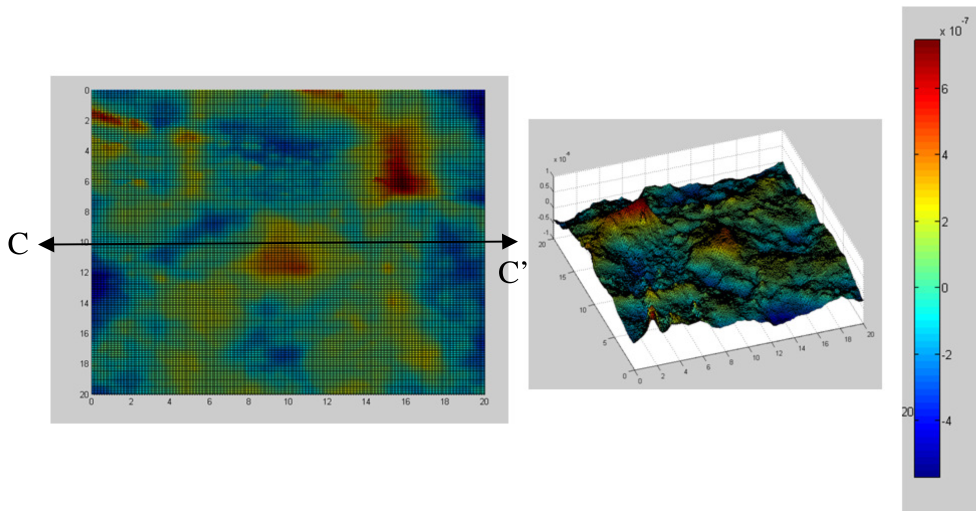

(b)

Fig. A4-3: 3D Suface Profile No. 3 (a) Unmated (b) Mated

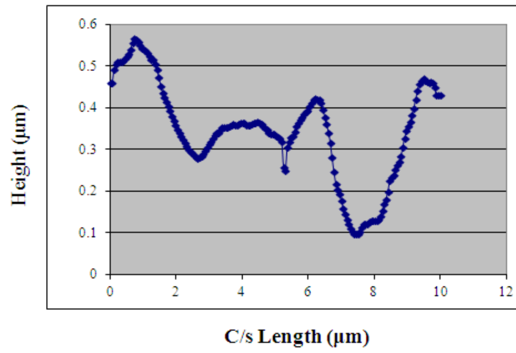

(Cross-Section along A-A')

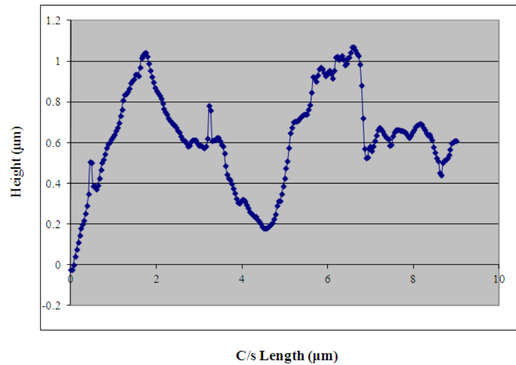

(Cross-Section along B-B')

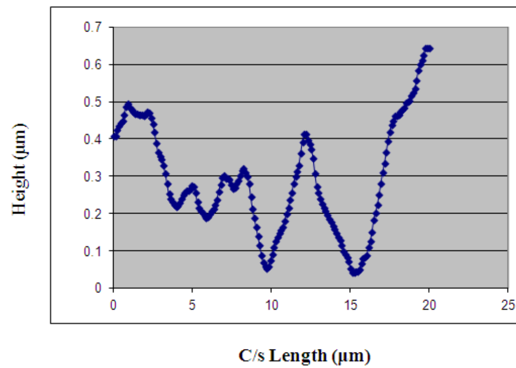

(Cross-Section along C-C')

Figure A4-4: Measured Cross-Sections

The surface is assumed to have uniform distribution of the peaks all across. 3 cross-sections are chosen from 3 different mated bumps characterized at their equatorial regions. Based on the number of major peaks and the surface length, the wavelengths of the surface profiles are estimated. For the surfaces as shown in Fig. A, B, C the wavelengths are determined to be 4, 5, 4.5 microns. The average wavelength thus these surfaces which is used in the modeling is 4.5 microns.

Appendix 5: Derivation of Rate of Change of Contact Area for Different Diffusion Models (Chapter 3)

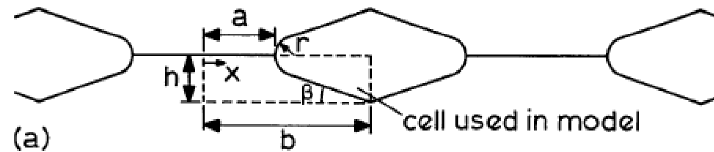

Figure A5-1: Contacting Surfaces Modeled as Small Cells due to Assumed Symmetry (Derby et al.)

List of Symbols-

a: Half of interfacial void width

A: Modified creep constant

A_c: Strain rate power law creep constant

A_c' : Creep constant from uniaxial creep testing

b: Half of bonded length between two adjacent voids (Half of average wavelength from the AFM measurement)

h: Half of interfacial cavity height (RMS roughness in the AFM measurement)

k: Boltzmann's constant

Q_v: Activation energy of volume diffusion

t: Bonding time

T: Bonding Temperature

P: Bonding Stress

γ: Surface Tension

R: Universal Gas Constant

μ: Chemical Potential

S: Sign of Bonding Pressure (negative for compression)

V: Volume transferred in bonding

b_v : Modulus of the burgers vector

$\dot{V}$: Rate of change of V with respect to time

f: Fraction of Bonded Area

Following are the values of gold for the above material parameters:

Parameters	Unit	Value	Reference
Atomic Volume	Ω (m^3)	1.7×10^{-29}	[17]
Burgers Vector	b_v (m)	2.56×10^{-10}	[16]
Shear Modulus	μ_o (Mpa)	2.7×10^{4}	[18]
Melting Temperature	T_m (K)	1337.33	[17]
Temperature coeff. of shear modulus	(K)	4×10^{-4}	[18]
Density	ρ (Kg m^{-3})	19.32×10^{3}	[17]
Surface Energy	γ (J m^{-2})	1.25	[19]
Bulk Diffusion Coeff	D_v (m^3 sec^{-1})	3×10^{-5}	[20]
Bulk Diffusion Activation Energy	Q_v (KJ mol^{-1})	207	[16]
Grain-Boundary Diffusion Coeff	$\delta_B D_B$ (m^3 sec^{-1})	5×10^{-15}	[16]
Grain-Boundary Diffusion Activation Energy	Q_B (KJ mol^{-1})	105	[16]
Surface Diffusion Coeff.	$\delta_s D_s$ (m^3 sec^{-1})	6×10^{-10}	[16]
Surface Diffusion Activation Energy	Q_s (KJ mol^{-1})	88	[21]
Power-Law Creep Constant	A (hr^{-1})	1.9×10^{-15}	[22]
Power-Law Creep Exponent	n_c	7	[22]

Table A5-1: Gold Property Constants

Parameters	Unit	Value
Half of bonded length between two adjacent voids	b (µm)	2.25
Half of interfacial cavity height	h (µm)	0.12
Bonding Temperature	T (Kelvin)	473
Angle between a surface ridge and the horizontal	β (degree)	45
Bond Neck Radius	r (µm)	.001
Stress	P (MPa)	159

Table A5-2: Other Parameters

Diffusion Mechanism 1: For surface source to neck

$$\dot{h} = \frac{\dot{V}}{b - a - r(1 - \sin\beta)} \quad \text{(A5-1)}$$

$$\dot{a} = \frac{h\dot{h}}{r\tan\beta(\frac{1}{\sin\beta} - \frac{\pi}{2} + \beta)}(\frac{1}{\sin\beta} - 1) - \frac{\dot{h}}{\tan\beta} \quad \text{(A5-2)}$$

Substituting equation (A7-2) in equation (A7-1) we get

$$\frac{\dot{a}\, r\tan\beta(\frac{1}{\sin\beta} - \frac{\pi}{2} + \beta)}{(h(\frac{1}{\sin\beta} - 1) - \frac{1}{\tan\beta})} = \frac{\dot{V}}{b - a - r(1 - \sin\beta)} \quad \text{(A5-3)}$$

Substituting a = bf where 0<f<1

$$\frac{b\dot{f}\, r\tan\beta(\frac{1}{\sin\beta} - \frac{\pi}{2} + \beta)}{(h(\frac{1}{\sin\beta} - 1) - \frac{1}{\tan\beta})} = \frac{\dot{V}}{b - bf - r(1 - \sin\beta)} \quad \text{(A5-4)}$$

$$dt = \frac{br\tan\beta(\frac{1}{\sin\beta} - \frac{\pi}{2} + \beta)(b - bf - r(1 - \sin\beta))}{(h(\frac{1}{\sin\beta} - 1) - \frac{1}{\tan\beta})\dot{V}}df \quad \text{(A5-5)}$$

For surface diffusion,

$$\dot{V}_1 = \frac{2\Omega\delta_s D_s}{rkT}\frac{\gamma}{r}(1 - \frac{r}{b - a}) \quad \text{(A5-6)}$$

For volume diffusion,

$$\dot{V}_2 = \frac{2\Omega D_v}{kT}\frac{\gamma}{r}(1 - \frac{r}{b - a}) \quad \text{(A5-7)}$$

$$\dot{V} = \dot{V}_1 + \dot{V}_2 = \frac{2\Omega}{kT}\frac{\gamma}{r}(1-\frac{r}{b-a})[\frac{\delta_s D_s}{r} + D_v] \text{.......... (A5-8)}$$

Substituting (A7-8) in (A7-5), we get

$$dt_1 = \frac{kTbr^2[\frac{\delta_s D_s}{r} + D_v]\tan\beta(\frac{1}{\sin\beta} - \frac{\pi}{2} + \beta)(b - bf - r(1-\sin\beta))}{2\gamma(h(\frac{1}{\sin\beta}-1) - \frac{1}{\tan\beta})\Omega(1-\frac{r}{b-bf})} df \text{ .... (A5-9)}$$

Diffusion Mechanism 2: For interfacial source to neck

$$\dot{h} = -\frac{2(r+a)}{\pi r}\frac{\dot{V}}{a} \text{ .... (A5-10)}$$

$$\dot{a} = \dot{h} \text{ .... (A5-11)}$$

Substituting (A7-11) in equation (A7-10), we get

$$\dot{a} = \frac{2(r+a)}{\pi r}\frac{\dot{V}}{a} \text{ .... (A5-12)}$$

Substituting a = bf in equation (A7-12), we get

$$b\frac{df}{dt} = \frac{2(r+a)}{\pi r}\frac{\dot{V}}{a} \text{ .... (A5-13)}$$

Simplifying (A7-13), we get

$$dt = \frac{b\pi ra}{2(r+a)\dot{V}} df \text{ .... (A5-14)}$$

For surface diffusion,

$$\dot{V}_3 = \frac{3\Omega\delta_B D_B}{2kTa}(P\frac{b}{a} - \frac{\gamma}{a} - \frac{\gamma}{r}) \text{.................................. (A5-15)}$$

For volume diffusion,

$$\dot{V}_4 = \frac{3\Omega r D_v}{kTa}(P\frac{b}{a} - \frac{\gamma}{a} - \frac{\gamma}{r}) \text{ .... (A5-16)}$$

$$\dot{V} = \dot{V}_3 + \dot{V}_4 = \frac{3\Omega}{kTa}(P\frac{b}{a} - \frac{\gamma}{a} - \frac{\gamma}{r})(\frac{\delta_B D_B}{2} + rD_v) \text{ .... (A5-17)}$$

Substituting (A7-17) in equation (A7-14) we get,

$$dt_2 = \frac{kTb\pi rb^2 f^2}{2(r+bf)3\Omega(P\frac{1}{f} - \frac{\gamma}{bf} - \frac{\gamma}{r})(\frac{\delta_B D_B}{2} + rD_v)} df \text{ .... (A5-18)}$$

Diffusion Mechanism 3: For mass transfer by bulk deformation

$$\dot{a} = \frac{-\dot{h}}{h}(b+a) \text{..} \quad \text{(A5-19)}$$

$$\dot{h} = -\frac{\dot{V}}{a} \quad \text{…………………………………………..} \quad \text{(A5-20)}$$

Substituting (A7-20) in equation (A7-19), we get

$$\frac{\dot{a}h}{(b+a)} = \frac{\dot{V}}{a} \text{………………........................} \quad \text{(A5-21)}$$

Substituting a=bf in equation (A7-21), we get

$$\frac{bdfh}{(b+a)dt} = \frac{\dot{V}}{a}$$

$$dt = \frac{bha}{(b+a)\dot{V}}df \quad \text{……………………………} \quad \text{(A5-22)}$$

We know,

$$\dot{V} = \frac{\sqrt{3}SA_c a^2 \tan\beta}{2[1-(\frac{a}{b})^{\frac{2}{n_c}}]^{n_c}} \left\{ \frac{2[P(\frac{b}{a}-1)-\frac{\gamma}{a}]}{\mu n_c} \right\}^{n_c} \quad \text{………………………………..} \quad \text{(A5-23)}$$

Substituting (A7-23) in equation (A7-22), we get

$$dt_3 = \frac{2h[1-(f)^{\frac{2}{n_c}}]^{n_c}}{(b+bf)\sqrt{3}SA_c f \tan\beta} \left\{ \frac{2[P(\frac{1}{f}-1)-\frac{\gamma}{bf}]}{\mu n_c} \right\}^{-n_c} df \quad \text{………………………………} \quad \text{(A5-24)}$$

Appendix 6: FEA Schematic (Chapter 4)

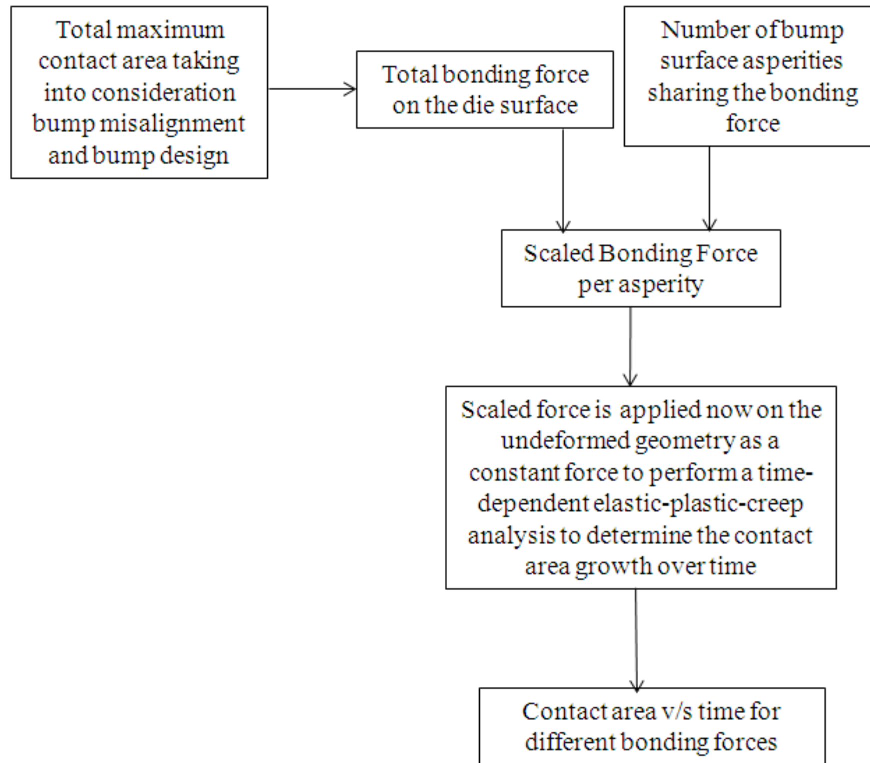

Figure A6-1: Schematic of FEA approach

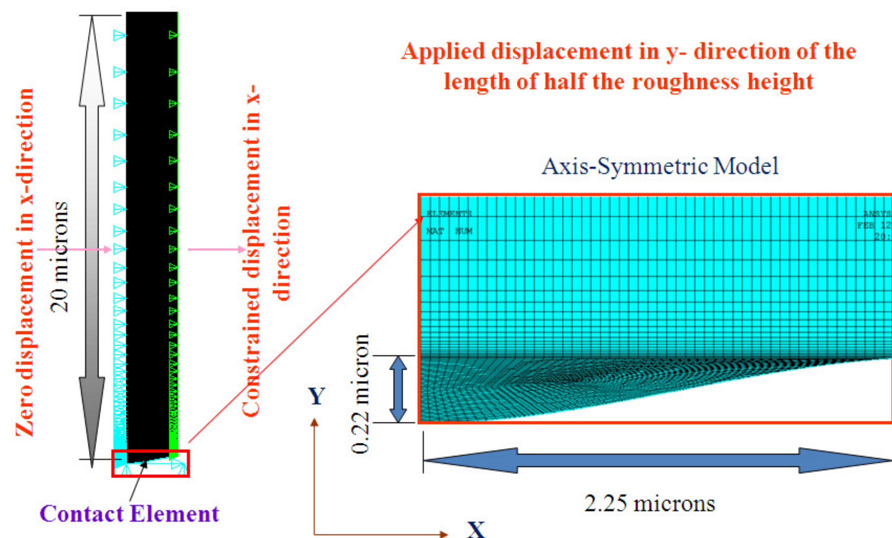

Figure A6-2: Representative "a-spot" Finite Element Model

The above schematic (Fig. A8-1) is repeated for each kind of roughness in the Design of Experiment. The number of asperities is calculated by dividing the total surface area (0.24 mm^2) (after taking into account the misalignment and bump positions) with the area of each asperity (1.59E-5 mm^2) and we get a total of approximately 15094 asperities. This is then used to scale the total bonding force. Fig. A8-2 explains the other boundary conditions. The left-side boundary has zero displacement in x-direction while the right-side boundary has coupled x-direction displacement. The rigid surface is fully clamped while the contact happens between the contact elements of the gold bump and the target elements of the rigid surface. This study was extended as mentioned in Chapter 4 to fractional factorial DOE varying different parameters which included different roughness shapes. The response surface model study had one of these 5 roughness profiles with varying bonding parameters and material properties. Below are the shape and meshing of the different roughness profiles used. Here the four moments are Sa is average roughness, Sr is RMS roughness, Sq is skewness and Sk is kurtosis. The details of the material models and model constants are in Chapter 4.

Sa=0, Sr=0 116 nm, Sq=0 -0.46, Sk=0 2

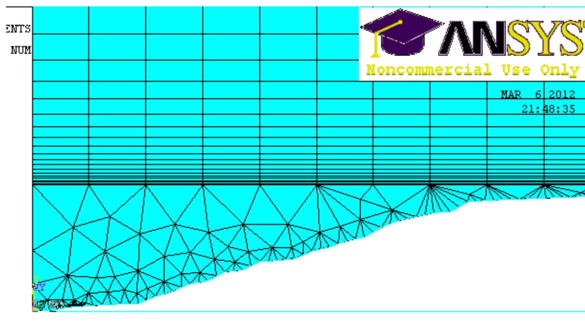

Figure A6-3: Roughness Profile # 1

Sa=0, Sr=116 nm, Sq= -0.46, Sk = 4.2

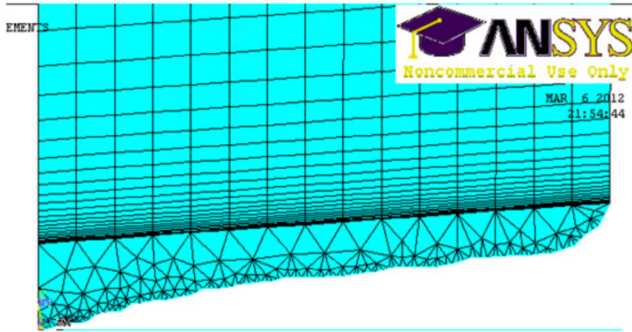

Figure A6-4: Roughness Profile # 2

Sa=192 nm, Sr= 430 nm, Sq= 0.8, Sk= 2

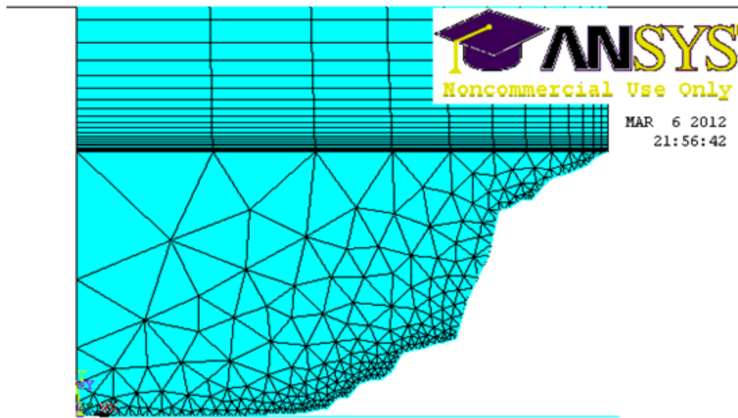

Figure A6-5: Roughness Profile # 3

Sa=192 nm, Sr =116 nm, Sq=0.8, Sk= 4.2

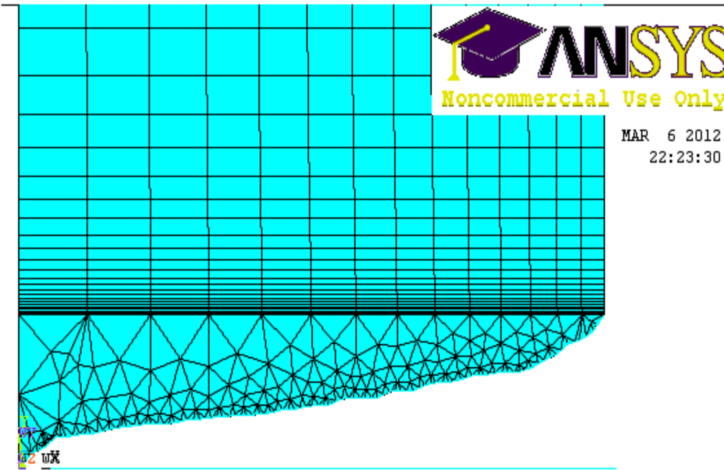

Figure A6-6: Roughness Profile # 4

Sa=0 nm, Sr=430 nm, Sq=0.8, Sk=4.2

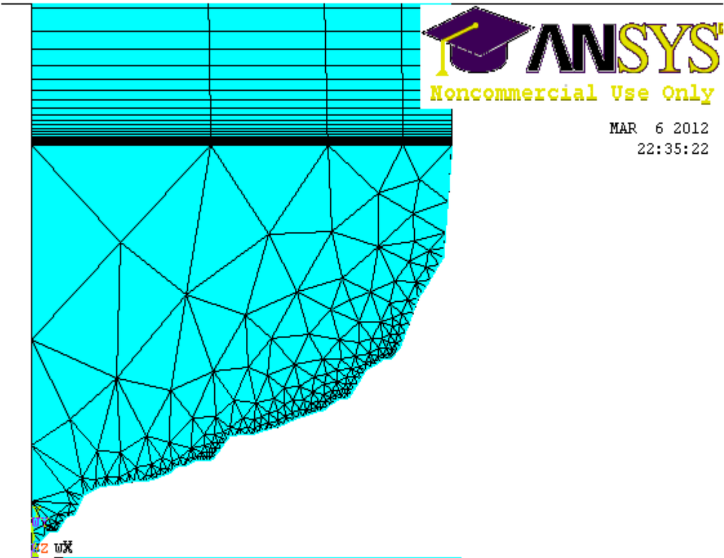

Figure A6-7: Roughness Profile # 5

Appendix 7: Multi-Asperity 2D Model Details (Chapter 4)

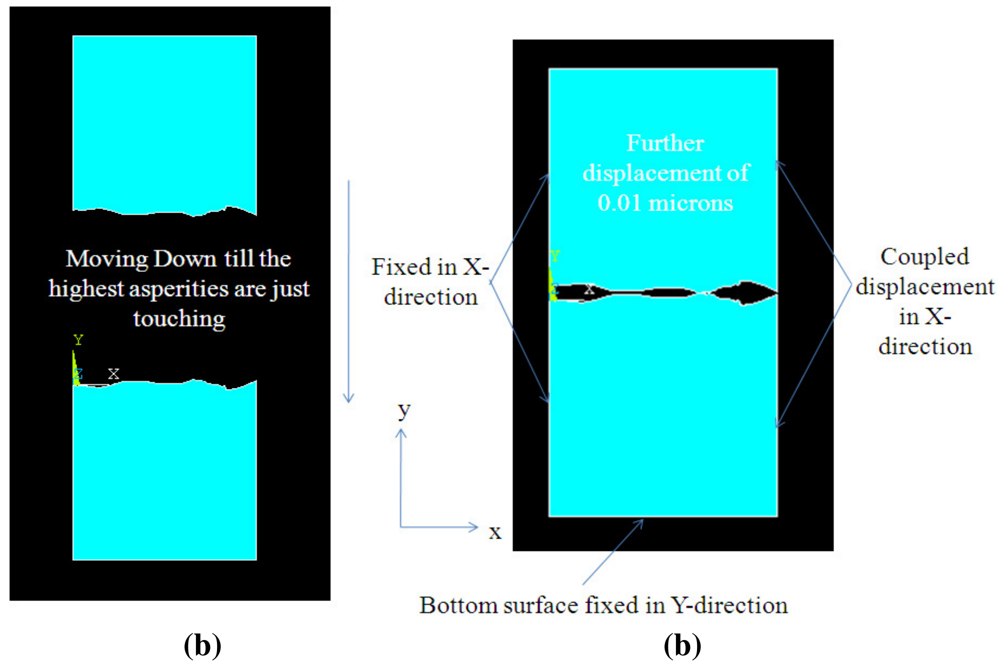

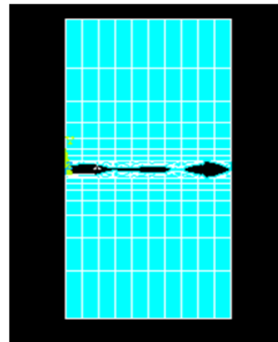

• **Total contact area is 0.5 microns**
• **Total surface area is 10.45 microns**
• **% area in contact ~ 4.8**

10,761 nodes

Plane 82 element- 8 node Solid Element

(c)

Figure A7-1: Multi-Asperity Model (a) Geometry (b) Boundary Conditions (c) Meshing

The boundary conditions as explained in Fig. A9-1 (b). The bottom surface is fixed in y-direction. The left hand edge is fixed in x-direction while the right hand edge has a coupled

displacement in x-direction. A displacement boundary condition is applied from the top. The type of surface in contact is parametrically varied by offsetting the top surface stepwise by 0.5 microns. Below are the various configurations from which the Force vs Displacement and Force vs Contact Area curves are derived.

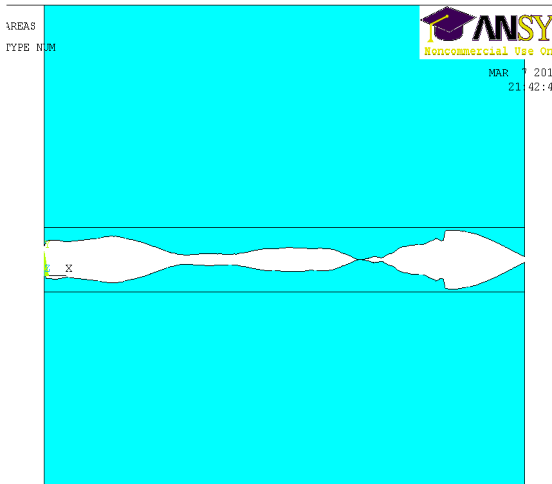

Figure A7-2: Offset Length: 0 µm

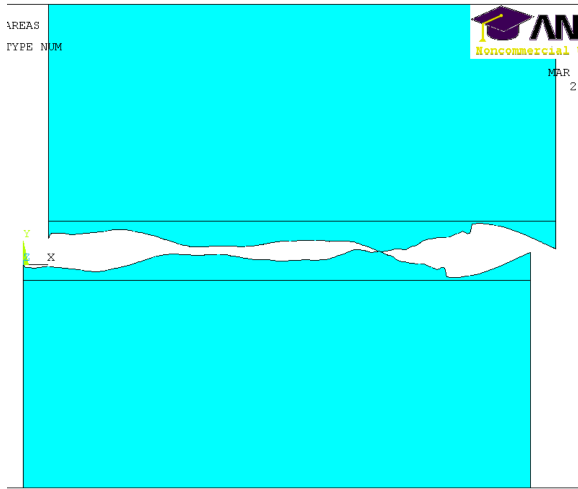

Figure A7-3: Offset Length: 0.5 µm

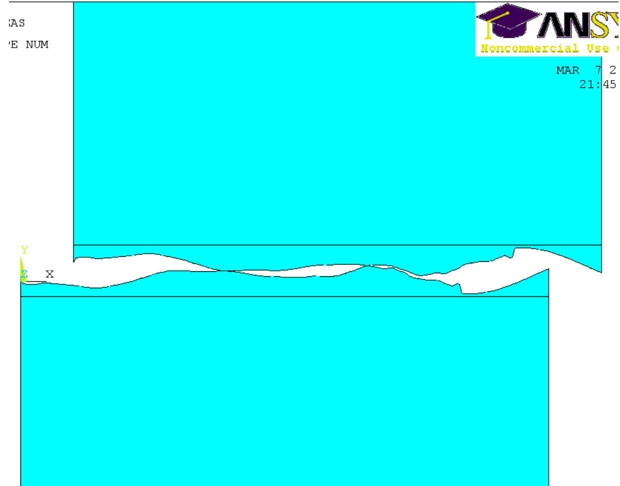

Figure A7-4: Offset Length: 1 µm

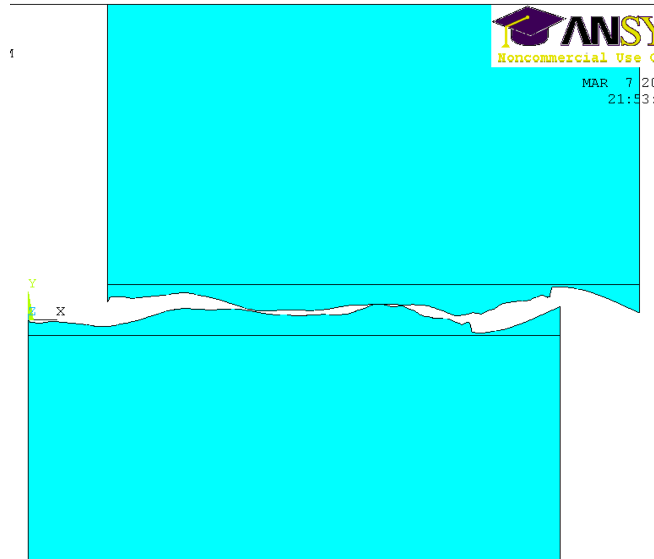

Figure A7-5: Offset Length: 1.5 µm

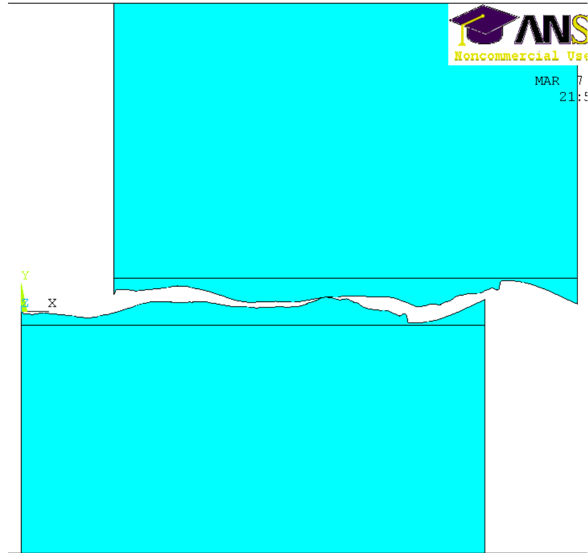

Figure A7-6: Offset Length: 2 µm

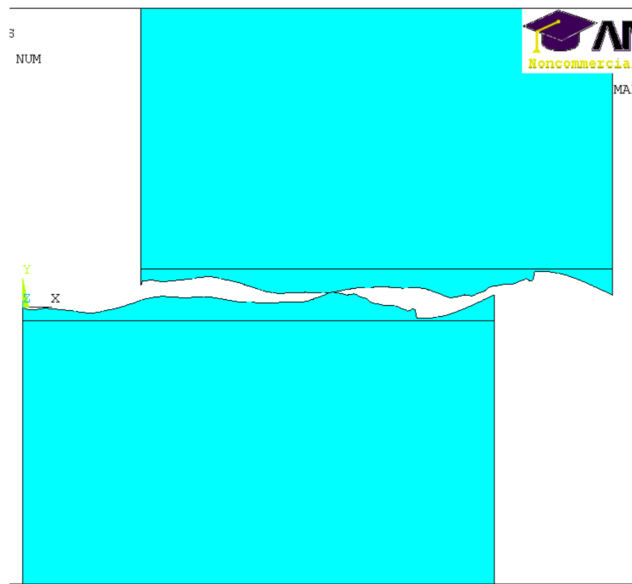

Figure A7-7: Offset Length: 2.5 µm

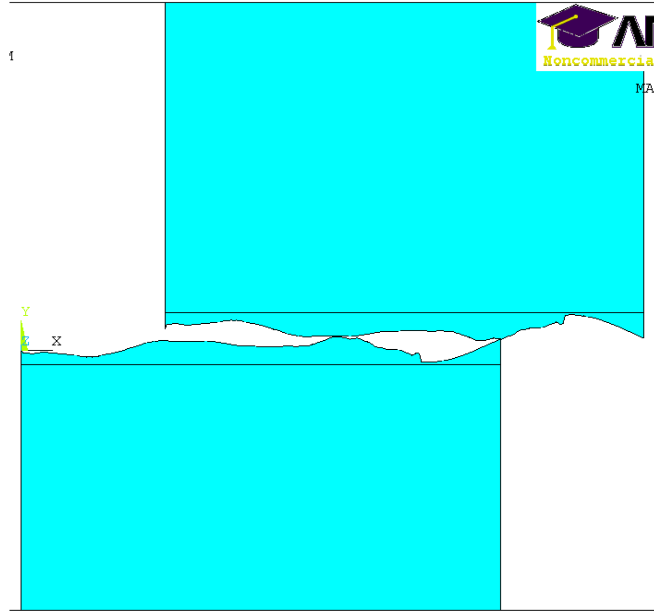

Figure A7-8: Offset Length: 3 µm

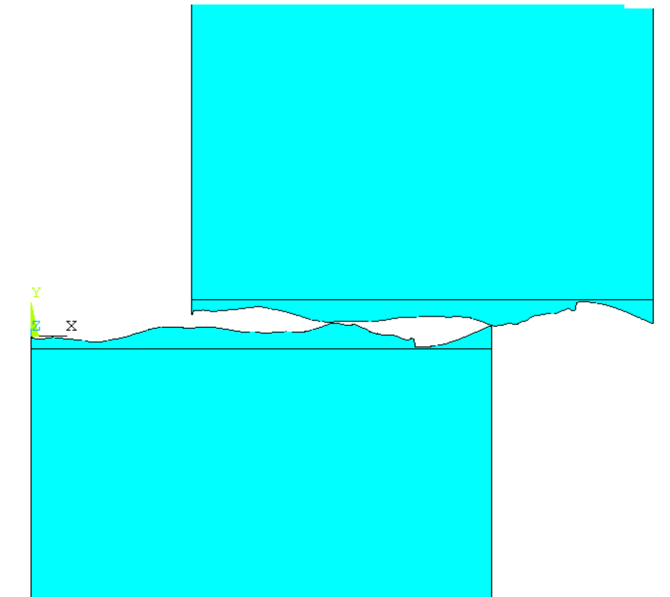

Figure A7-9: Offset Length: 3.5 µm

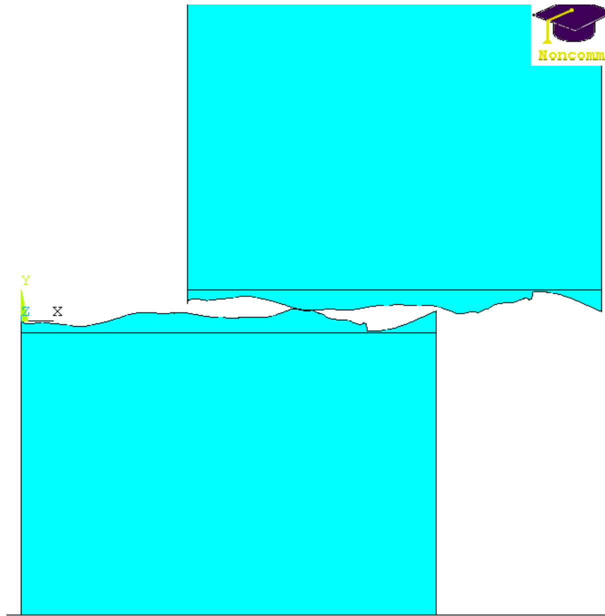

Figure A7-10: Offset Length: 4 µm

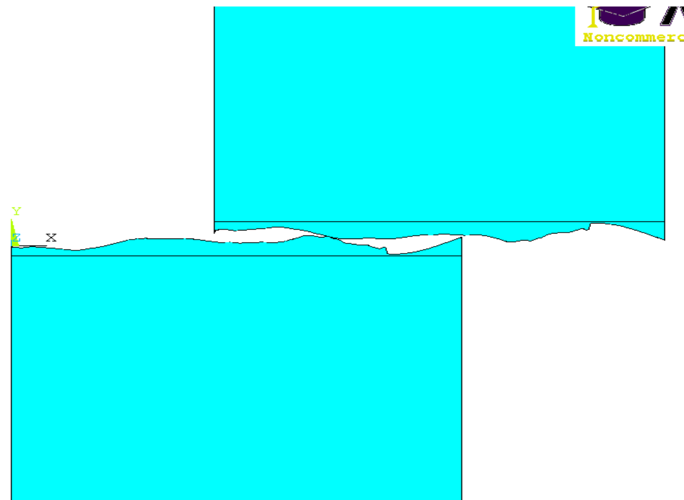

Figure A7-11: Offset Length: 4.5 µm

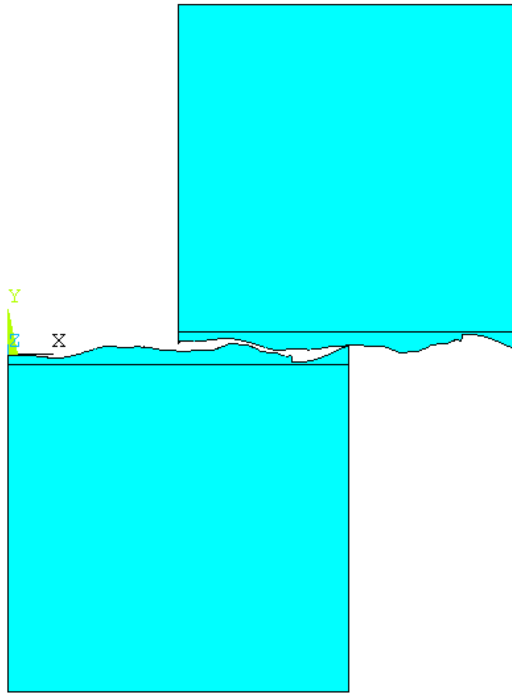

Figure A7-12: Offset Length: 5 µm

Bibliography

1. Lau, J.; Wong, C.P.; Lee, N. and Lee, S.W., "Electronics Manufacturing with Lead-Free, Halogen-Free Conductive Adhesives," 1st Edition, McGraw Hill, 2002, ISBN: 0071386246.
2. Caers, J. F. J.; Zhao, X. J.; Sy, H. G.; Wong, E. H. and Mhaisalkar, S. G., "Towards a predictive behavior of nonconductive adhesive interconnects in moisture environment," in 54th Electronic Components and Technology Conference, Las Vegas, NV, 2004, pp. 106-112, DOI: 10.1109/ECTC.2004.1319322.
3. Haase, J., Iyer, P., Baumgartner, P., Farley, D., Dasgupta, A. and Caers, J., "Mechanics of Adhesively Bonded Flip-Chip-on-Flex Assemblies. Part I: Durability of Anisotropically Conductive Adhesive Interconnect," Journal of Adhesion Science and Technology Vol 22, pp. 1733–1756, 2008, DOI: 10.1163/156856108X320564.
4. Farley, D.; Kahnert, T.; Sinha, K.; Solares, S.; Dasgupta, A.; Caers, J.F.J. and Zhao, X.J., "Cold welding: A new factor governing the robustness of adhesively bonded flip-chip interconnects," Proceedings, 59th Electronic Components and Technology Conference, 2009, pp. 67, DOI: 10.1109/ECTC.2009.5073998.
5. Obeid, I.; Morizio, J. C.; Moxon, K. A.; Nicolelis, M. A. L. and Wolf, P. D., "Two multichannel integrated circuits for neural recording and signal processing," IEEE Transactions on Biomedical Engineering, vol. 50, pp. 255-258, Feb 2003, DOI: 10.1109/TBME.2002.807643.
6. Aschenbrenner, R.; Gwiasda, J.; Eldring, J.; Zakel, E. and H. Reichl, "Gold Ball Bumps for Adhesive Flip Chip Assembly," in Adhesives in Electronics '94, VDI/VDE Tagung, 1994.
7. Holm R., "Electric Contacts Handbook", Springer-Verlag Berlin, 1958, 3rd ed., pp. 433.

8. Johnson, K. L.; Kendall, K. and Roberts, A. D., "Surface Energy and the Contact of Elastic Solids," Proceedings of the Royal Society of London, Series A, Vol. 324, No. 1558, 1971, pp. 301-313, DOI: 10.1098/rspa.1971.0141.
9. Cuthrell, R. E. and Tipping, D. W., "Electric Contacts. II. Mechanics of closure for gold contacts," Journal of Applied Physics, 44(10), 1973, pp. 4360-4365, DOI: 10.1063/1.1661964.
10. G. Garmong; N. E.P. Aton and A.S. Argon , "Attainment of Full Interfacial During Diffusion Bonding", Metallurgical and Materials Transactions A, Vol. 6, Number 6, 1269-1279, DOI: 10.1007/BF02658537.
11. Hamilton, C.H., "Superplastic Forming and Diffusion Bonding of Titanium Alloys", Titanium Science and Technology, pp. 621-647, Plenum Press, New York, 1973, DOI: 10.1002/9780470686652.eae223.
12. A. A. L. White and D. J. Allen: in Proc. Conf. on 'Joining of metals', Vol. 2, 96; 1981, London, Institution of Metallurgists.
13. Derby, B. and Wallach, E. R., "Theoretical model for diffusion bonding", Met. *Sci.,* 1982, 16, 49, DOI: http://dx.doi.org/10.1179/030634582790427028.
14. Derby, B. and Wallach, E. R., "Diffusion Bonding: Development of Theoretical model", Met. Sci., Volume 18, Number 9, September 1984, pp. 427-431(5), DOI: http://dx.doi.org/10.1179/030634584790419809.
15. King W.H. and Owczarski W.A., "Diffusion Welding of Commercially Pure Titanium", Welding Journal, 46 (1967) 289s.
16. Frost, H.J. and Ashby, M.F., "Deformation Mechanism Maps" Pergamon, Oxford 1982.
17. http://www.chemicool.com/elements/gold.html
18. http://www.kayelaby.npl.co.uk/general_physics/2_2/2_2_2.html

19. Needs R. J. and Mansfield M., “Calculations of the surface stress tensor and surface energy of the (111) surfaces of iridium, platinum and gold”, J. Phys.: Condens. Matter 1 (1989) 7555-7563, Printed in the UK, DOI: 10.1088/0953-8984/1/41/006.
20. Arcidiacono, S.; Bieri, N.R.; Poulikakos, D. and Grigoropoulos, C.P., “On the coalescence of gold nanoparticles”, International Journal of Multiphase Flow 30 (2004) 979-994, DOI: 10.1007/s11671-009-9298-6.
21. Lin, T.S. and Chung, Y.W., “Measurement of the activation energy for surface diffusion in gold by scanning tunneling microscopy”, Journal of Surface Science, Volume 207, Issues 2–3, 1 January 1989, Pages 539–546, DOI: 10.1016/0039-6028(89)90140-4.
22. Brown, C.; Rezvanian, O.; Zikry, M. A. and Krim, J., “Temperature dependence of asperity contact and contact resistance in gold RF MEMS switches”, J. Micromechanics and Microengineering, 19 (2009) 025006 (9pp), DOI: 10.1088/0960-1317/19/2/025006.
23. Sinha, K and Dasgupta A.,“Dependence of Bond Strength in Adhesively Bonded Flip-Chip Interconnects on Different Parameters: Part 2”, Proceeding paper in this issue.
24. Simon, S. L.; McKenna, G. B. and Sindt, O., “Modeling the Evolution of the Dynamic Mechanical Properties of a Commercial Epoxy During Cure after Gelation,” Journal of Applied Polymer Science, Vol. 76, 495–508 (2000)
25. Taylor, P. A.; Nelson, J. S. and Dodson, B. W.,"Adhesion between Atomically Flat Metallic Surfaces," Physical Review B, 44, 5834, 1991, DOI:10.1103/PhysRevB.44.5834
26. Sinha, K.; Farley, D.; Kahnert T.; Dasgupta A.; Caers J. F. J. and Zhao X.J., “Dependence of Bond Strength in Adhesively Bonded Flip-Chip Interconnects on Different Parameters: Part 1”, Preceding paper in this issue.

27. Ellis, T. W., "The Future of Gold in Electronics," Gold Bulletin. Vol. 37, no. 1-2, pp. 66-71. 2004, DOI: 10.1007/BF03215518.

28. Ferguson G.; Chaudhury, M.; Sigal G. and Whitesides G., "Contact adhesion of thin gold films on elastomeric supports - Cold welding under ambient conditions," Science, Vol. 253, pp. 776-778, 1991, DOI: 10.1126/science.253.5021.776.

29. Frisk, L. and Ristolainen, E., "Flip chip attachment on flexible LCP substrate using an ACF," Microelectronics Reliability 45 (2005) 583–588, DOI: http://dx.doi.org/10.1016/j.microrel.2004.10.009.

30. Teh L.K.; Wong C.C.; Mhaisalkar S.; Ong, K., Teo, P.S. and Wong, E.H., "Characterization of Nonconductive Adhesives for Flip-Chip Interconnection," Journal of Electronic Materials, Vol. 33, No. 4, pp. 271-276, 2004, DOI: 10.1007/s11664-004-0132-8.

31. Teo, M.; Mhaisalkar, S. G.; Wong, E. H.; Teo, P.-S.; Wong, C. C.; Ong, K.; Goh C. F. and Teh L. K., "Correlation of Material Properties to Reliability Performance of Anisotropic Conductive Adhesive Flip Chip Packages," IEEE Transactions on Components and Packaging Technologies, Vol. 28, No. 1, March 2005, DOI: 10.1109/TCAPT.2004.843175.

32. Yim M.J.; Hwang J.S.; Kwon W.; Jang K.W. and Paik, K.W., "Highly reliable nonconductive adhesives for flip chip CSP applications," Electronics Packaging Manufacturing, IEEE Transactions on, Vol. 26, No. 2, pp.150–155, April 2003, DOI: 10.1109/TEPM.2003.817715.

33. Yin, C.; Lu, H.; Bailey, C. and Chan, Y-C., "Effects of Solder Reflow on the Reliability of Flip-Chip on Flex Interconnections Using Anisotropic Conductive Adhesives," IEEE Transactions on Electronics Packaging Manufacturing, Vol. 27, No. 4, 2004, DOI: 10.1109/TEPM.2004.843152.

34. Aschenbrenner, R.; Miessner, R. and Reichl, H., “Adhesive flip chip bonding on flexible substrates,” The First IEEE International Symposium on Polymeric Electronics Packaging, Oct 1997, DOI: 10.1109/PEP.1997.656478.

35. Chan, Y.C.; Hung, K.C.; Tang, C.W. and Wu, C.M.L., “Degradation Mechanisms of Anisotropic Conductive Adhesive Joints for Flip Chip on Flex Applications,” Adhesive Joining and Coating Technology in Electronics Manufacturing, 2000, DOI: 10.1109/ADHES.2000.860588.

36. Chiang, K.N.; Chang, C.W. and Lin, J.D., “Analysis of ACA/ACF package using equivalent spring method,” Electronics Packaging Technology Conference, 2000, DOI: 10.1109/EPTC.2000.906358.

37. Li, L. and Fang, T., “Anisotropic Conductive Adhesive Films for Flip Chip on Flex Packages,” Adhesive Joining and Coating Technology in Electronics Manufacturing, 2000, Proceedings on 4th International Conference, DOI: 10.1109/ADHES.2000.860586.

38. Ferrando, F.; Zaberli, J.F.; Clot, P. and Chenuz, J.M., “Industrial approach of a Flip-Chip method using the stud-bumps with a non-conductive paste,” Adhesive Joining and Coating Technology in Electronics Manufacturing, Proceedings. 4th International Conference on, pp. 205-211, 2000, DOI: 10.1109/ADHES.2000.860600.

39. Pajonk, J., “New flip chip technology utilizing non-conductive adhesive adapted for high volume chip card module production,” Electronics Manufacturing Technology Symposium, 2004, DOI: 10.1109/IEMT.2004.1321653.

40. Mercado, L. L.; White, J.; Sarihan V. and Lee, T., “Failure Mechanism Study of Anisotropic Conductive Film (ACF) Packages,” IEEE Transactions on Components and Packaging Technologies, Vol. 26, No. 3, September 2003, DOI: 10.1109/TCAPT.2003.817640.

41. Jang, C.; Han, S.; Kim, Y.; Kim, H.; Yoon, S.; Cho, S.; Han, C. and Han, B., "Development of Predictive Modeling Scheme for Flip-chip on Fine Pitch Flex Substrate," EuroSimE 2005, DOI: 10.1109/ESIME.2005.1502868.

42. Kristiansen, H.; Gulliksm, M.; Haugerud, H. and Friberg, R., "Characterization of Electrical Contacts Made By Non-Conductive Adhesive," Adhesive Joining and Coating Technology in Electronics Manufacturing, 1998, DOI: 10.1109/ADHES.1998.742051.

43. Caers, J.; Zhao, X.; Wong E. and S. Mhaisalkar, "Towards a predictive behavior of non-conductive adhesive interconnects in moisture environment," ECTC 2004, DOI: 10.1109/ECTC.2004.1319322.

44. Chan, Y.C. and Luk, D.Y., "Effects of bonding parameters on the reliability performance of Anisotropic conductive adhesive interconnects for Flipchip-on-flex packages assembly II. Different bonding pressure," Microelectronics Reliability 42 (2002) 1195–1204, DOI: http://dx.doi.org/10.1016/S0026-2714(02)00089-6.

45. Fu, Y.; Wang, Y.; Wang, X.; Liu, J.; Lai, Z.; Chen, G. and Willander, M., "Experimental and theoretical characterization of electrical contact in anisotropically conductive adhesive," IEEE Transactions on Advanced Packaging, Vol. 23, No. 1, 2000, DOI: 10.1109/6040.826757.

46. Yeo, A.; Teo, M. and Lee, C., "Thermo- and Hydro-mechanical Modeling of an Adhesive Flip Chip Joint," Electronics Packaging Technology Conference, 2004, DOI: 10.1109/EPTC.2004.1396583.

47. Wu C.M.L.; Liu, J. and Yeung N.H., "Reliability of ACF in Flip-Chip with Various Bump Height," Adhesive Joining and Coating Technology in Electronics Manufacturing, 2000, DOI: 10.1109/ADHES.2000.860580.

48. Johnson, K.L., "Contact Mechanics", Cambridge: Cambridge University Press, 1985.

49. Johnson, K.L., “Contact Mechanics”, Cambridge University Press , London, 1998.

50. Holm, R., “Electric Contacts: Theory and Applications”, Berlin, Germany: Springer, 1969.

51. Dickrell, D.J.; Dugger, M.T.; Hamilton M.A. and Sawyer, W.G., "Direct Contact-Area Computation for MEMS Using Real Topographic Surface Data," J. Microelectromech. Syst., Vol.16, No.5, pp.1263-1268, Oct. 2007, DOI: 10.1109/JMEMS.2007.901120.

52. Chang, W.; Etison, I. and Bogy, D., “An elastic-plastic model for the contact of rough surfaces,” ASME J. Tribol., 109, pp. 257-263, 1987, DOI: http://dx.doi.org/10.1115/1.3261348.

53. Majumder, S.; McGruer N.E.; Adams, G.G.; Zavracky, P.M.; Morrison, R.H. and Krim, J., “Study of contacts in an electrostatically actuated microswitch,” Sensors and Actuators A, vol.93, no.1, pp. 19-26, 2001, DOI: 10.1109/HOLM.1998.722437.

54. Rezvanian, O.; Zikry, M.A.; Brown, C. and Krim, J., “Surface roughness, asperity contact and gold RF MEMS switch behavior,” J. Micromech. Microeng. 17, pp. 2006-2015, 2007, DOI: 10.1088/0960-1317/17/10/012.

55. Choi, Y. and Suresh, S., “Nanoindentation of patterned metal lines on a Si substrate”, Scripta Materialia 48, 249, 2003, DOI: http://dx.doi.org/10.1016/S1359-6462(02)00377-9.

56. Shan, Z. and Sitaraman, K., “Elastic-plastic characterization of thin films using nanoindentation techniques”, Thin Solid Films *437,* 176, 2003, DOI: http://dx.doi.org/10.1016/S0040-6090(03)00663-1.

57. Giannakopoulos, A. E.; Larsson P.-L. and Vestergaard, R., “Analysis of Vickers indentation", Int. J. Solids and Struct., 31, 2679-2708, 1994, DOI: http://dx.doi.org/10.1016/0020-7683(94)90225-9.

58. Larsson, P.-L.; Giannakopoulos, A. E.; So¨derlund, E.; Rowcliffe, D. J. and Vestergaard, R., “Analysis of Vickers indentation", Int. J. Solids Struct. 33, 221, 1996, DOI: 10.1016/0020-7683(95)00033-7.

59. Giannakopoulos, A. E. and Suresh S., "Determination of elastoplastic properties by instrumented sharp indentation", Scripta Mater. 40, 1191, 1999, DOI: 10.1016/S1359-6462(99)00011-1.

60. Suresh, S. and Giannakopoulos, A. E., "A new method for estimating residual stresses by instrumented sharp indentation", Acta Materialia, vol. 46 (16), 1998, pp. 5755-5767, DOI: http://dx.doi.org/10.1016/S1359-6454(98)00226-2.

61. Frost, H.J. and Ashby, M.F., "Deformation Mechanism Maps" Pergamon, Oxford 1982.

62. Brown, C.; Rezvanian, O.; Zikry, M.A. and Krim, J., "Temperature dependence of asperity contact and contact resistance in gold RF MEMS switches", J. Micromech. Microeng. 19 (2009) 025006 (9pp), DOI: 10.1088/0960-1317/19/2/025006.

63. Song, B.; Azarian, M.H.; Varghese, J.; Dasgupta, A. and Pecht, M., "Dynamic Loading Durability and Failure Site Transition in Enig-Sn37pb Interconnects in a Stacked Die BGA Package", IEEE Transactions on Components and Packaging Technologies, 2006.

64. Xu, L. and Pang, J.H.L., "Effect of Intermetallic and Kirkendall Voids Growth on Board Level Drop Reliability for SnAgCu Lead-free BGA Solder Joint ", Proceedings of the IEEE Electronic Components and Technology Conference, 275-282, 2006.

65. Yao, D. and Shang, J.K., "Effect of cooling rate on interfacial fatigue-crack growth in Sn-Pb solder joints", IEEE Trans. Components, Packaging, and Manufacturing Technology, Part B, 19(1):, 154-165, 1996.

66. Evans A.G. and Hutchinson, J.W., "Effects of Non-Planarity on the Mixed Mode Fracture Resistance of Bimaterial Interfaces", Acta Metallurgica, 1989. 37(3): p. 909- 916.

67. Rice, J. R., "Elastic Fracture Mechanics Concepts for Interface Cracks", Journal of Applied Mechanics, 1988. 55: p. 98–103.

68. Suo, Z. and Hutchinson, J. W., "Sandwich Test Specimens for Measuring Interface Crack Toughness", Materials Science & Engineering A: Structural Materials: Properties, Microstructure and Processing, 1989. A107 (1-2): p. 135-143.

69. Hutchinson, J. W. and Suo, Z., "Mixed Mode Cracking in Layered Materials. Advances in applied mechanics", 1992. 29: p. 63-191.

70. Tu, P. L.; Chan, Y. C.; Hung, K. C. and Lai, J. K. L., "Growth Kinetics of Intermetallic Compounds in Chip Scale Package Solder Joints", Scripta Materialia, 2001. 44(2): p.317-323.

71. Evans, A. G., Ruhle, M., Dalgleish, B. J. and Charalambides, P. G., "The fracture energy of bimaterial interfaces in Metal-Ceramic Interfaces", 1990, Metall. Trans. *A* 21A:2419–29.

72. Wei, Y and Hutchinson, J. W., " Models of interface separation accompanied by plastic dissipation at multiple scales", 1999, Int. J. Fract 95:1–17.

73. Suo, Z.; Shih, C. F. and Varias, A. G., "A theory for cleavage cracking in the presence of plastic flow", Acta Metall. Mater., 1993, 41:1551–57.

74. Tvergaard, V. and Hutchinson, J. W., "Toughness of an Interface along a Thin Ductile Layer joining Elastic Solids", 1994, Philos Mag. A 70:641–56.

75. Lane, M.W.; Dauskardt, R.H.; Vainchtein, A. and Gao, H. "Plasticity contributions to interface adhesion in thin-film interconnect structures", 2000, J. Mater. Res. 15:2758–69.

76. Wei, Y. and Hutchinson, J.W., "Interface strength, work of adhesion and plasticity in the peel test." Int. J. of Fracture, 93, 315-333, (1998).

77. Jang, J.W.; Lin, J.K. and Frear, D. R., 'Failure Morphology after the Drop Impact Test of the Ball Grid Array Package with Lead-Free Sn-3.8Ag-0.7Cu on Cu and Ni Under-Bump Metallurgies", Journal of Electronic Materials, 2007. 36(3): p. 207-213.

78. Tu, P. L.; Chan, Y. C.; Hung, K. C. and Lai, J. K. L., “Growth Kinetics of Intermetallic Compounds in Chip Scale Package Solder Joints”, Scripta Materialia, 2001. 44(2): p.317-323.

79. P. L. Liu and J. K. Shang, “A Comparative Fatigue Study of Solder/Electroless-Nickel and Solder/Copper Interfaces”, Journal of Material Research, 2000. 15(11): p. 2347- 2355.

80. He, J.; Guo, Y. and Lin, Z., " Numerical and experimental analysis of thermosonic bond strength considering interfacial contact phenomena”, Journal of Physics D: Applied Physics, vol. 41, 2008, 165304 (13pp), DOI:10.1088/0022-3727/41/16/165304.

81. Fu, X. and Chung, D.D.L., “Sensitivity of the bond strength to the structure of the interface between reinforcement and cement, and the variability of this structure”, Journal of Cement and Concrete Research, Volume 28, Issue 6, June 1998, Pages 787-793, DOI: http://dx.doi.org/10.1016/S0008-8846(98)00055-6.

82. Bazhutin, N. B., G. K. Boreskov and V. I. Savchenko, “Adsorption of molecular and atomic oxygen on gold”, React. Kinet. Catal. Lett., Vol. 10, No. 4,337-340 (1979), DOI: 10.1007/BF02075320.

83. Baker, T. A.; Xu B., Liu X.; Kaxiras E. and Friend, C.M., “Nature of Oxidation of the Au(111) Surface: Experimental and Theoretical Investigation”, Journal of Physical Chemistry C Letters, 2009, *113,* 16561–16564, DOI: 10.1021/jp9052192.

84. Kahnert, T., “Au/Au bonding study for adhesively bonded flip chip packages,” Master’s Thesis, University of Applied Science Mannheim, 2008.

85. Farley, D.; Dasgupta, A. and Caers, J.F.J, “Mechanics of Adhesively Bonded Flip-Chip-on-Flex Assemblies. Part II: Effect of Bump Coplanarity on Manufacturability and Durability of Non-Conducting Adhesive Assemblies,” Journal of Adhesion Science and Technology, *22,* 1757, 2008.

86. Haase, J., “Characterization of a Selected Anisotropic Conductive Adhesive,” M.S. Thesis, University of Maryland, College Park, Maryland, 2001.

87. Smith, J. R.; Bozzolo, G.; Banerjea, A. and Ferrante, J., “Avalanche in Adhesion,” Physical Review Letters, Vol. 63, No. 12, 1989.

88. Alcantar, N. A.; Park, C.; Pan, J-M. and Israelachvili, J. N., “Adhesion and coalescence of ductile metal surfaces and nanoparticles,” Acta Materialia 51 (2003)

89. Varghese, J., “Effect of Dynamic Flexural Loading on the Durability and Failure Site of Solder Interconnects in Printed Wiring Assemblies,” PhD Thesis, University of Maryland, College Park, Maryland, 2007.

90. Lane, M., “Interface Fracture”, Annu. Rev. Mater. Res, 2003, 33:29–54, DOI: 10.1146/annurev.matsci.33.012202.130440.